Offshore Wind Turbine Interaction with Floating Freshwater Ice on the Great Lakes

by

Bingbin Yu

A dissertation submitted in partial fulfillment
of the requirements for the degree of
Doctor of Philosophy
(Naval Architecture and Marine Engineering)
in The University of Michigan
2014

Doctoral Committee:

Associate Professor Dale G. Karr, Chair
Assistant Professor Jeremy N. Bassis
Assistant Professor Matthew D. Collette
Senior Engineer Amy N. Robertson, National Renewable Energy Laboratory

For my dear grandpa, Xingwei Jiang. Hope you are proud of me.

ACKNOWLEDGEMENTS

Thanks to all the people who make this dissertation possible.

The research is sponsored by U.S. Department of Energy and is in cooperation with National Renewable Energy Laboratory.

Thanks to Professor Dale G. Karr for your support through these five and a half years. Thanks for all your advise on research and life. Thanks to my committee members for your valuable comments.

Thanks to my parents, my grandma, my fiance Guang Dong, my five-year roommate Jessie Huang and all my friends for your love and company. You made life wonderful.

TABLE OF CONTENTS

LIST OF FIGURES

Figure

ABSTRACT

Offshore Wind Turbine Interaction with Floating Freshwater Ice on the Great Lakes

by

Bingbin Yu

Chair: Dale Karr

Developing offshore wind energy has become more and more serious worldwide in recent years. Many of the promising offshore wind farm locations are in cold regions that may have ice cover during wintertime. The challenge of possible ice loads on offshore wind turbines raises the demand of modeling capacity of dynamic wind turbine response under the joint action of ice, wind, wave and current. The simulation software FAST is an open source CAE package maintained by the National Renewable Energy Laboratory. In this thesis, a new module of FAST for assessing the dynamic response of offshore wind turbines subjected to ice forcing is presented.

In the ice module, six models are included which involve both prescribed forcing and coupled response. The division of ice models is based on different ice failure modes and ice-structure interaction characteristics. Among these six models, two new analytical models of ice loading are presented. One is a new analytical model to simulate time-dependent ice forces limited by ice failure with the ice considered to fail in multiple zones non-simultaneously. The other model generates time-dependent ice forces on sloping structures due to bending failure.

Besides ice loading models, since ice thickness is an important input parameter

when predicting ice loads, several analytical models that predict ice thickness change over time as a function of air temperatures are also presented in this thesis.

CHAPTER I

Introduction

Wind energy is recognized worldwide as a proven technology to meet increasing electricity demands in a sustainable and clean way. Offshore wind energy has an added attraction since it has minimal environmental effects and the best resources are reasonably well located relative to the centers of electricity demand.

As of 2013, no offshore wind turbines have been installed in U.S. waters. Desired wind farm site characteristics include good wind resource, shallow water (less than 30m), and proximity to land, load centers, and on-shore transmission lines (*Tarp-Johansen*, 2005). Therefore, the most promising locations for offshore wind turbines in the US are off the northeast coast (roughly form Virginia north) and the Great Lakes.

For development of offshore wind energy in the Great Lakes, one important technological challenge is the presence of ice. Some areas of the lakes can remain ice free for the entire winter, but there are exceptionally harsh winters when ice cover reaches nearly 100% of the surface of the Great Lakes. Lake Superior, Huron and Erie are often substantially ice covered and have wind driven ice floes at times. The extent of ice cover, ice thickness and ice strength are highly variable, both over space and over time. The forces exerted on the wind turbine structure are associated with geometry, motion and failure strength of ice. Therefore, the ice forces are also highly

variable. Unlike other offshore structures in cold areas, offshore wind turbines are not only subject to coupled forcing from ice, winds, waves and currents, their structural responses are also influenced by turbine dynamics and forces.

For the above reasons, there is need for Computer-Aided Engineering (CAE) tools that are capable of modeling all the design-driving loads interacting with offshore wind turbine systems during operation. We have augmented an existing CAE tool, FAST, used for offshore wind turbine analysis with a new module that can provide the impact of ice loading on the system. FAST is the CAE tool maintained by the National Renewable Energy Laboratory (NREL) for simulating onshore and offshore wind turbine dynamics. Before the addition of the ice module, it only considered loading from wind, wave, current and seismic base motions. The new module includes both static and dynamic ice loading that can be applied during a dynamic simulation of an offshore wind turbine. When calculating the dynamic ice loads, the ice module is coupled with the main FAST program and exchanges with it the data such as the ice forces and structure responses. When calculating the static or quasi-static ice load, the ice module is decoupled and submits the data of ice forces to the main program.

In Chapter 2, a more detailed description of FAST and its interaction with the ice module is given. Using FAST with the new module, we are able to model the offshore wind turbine structural response in cold weather environments and predict the resulting stresses and response frequencies resulting from ice actions.

Here, an offshore system consisting of an NREL 5.0 MW Baseline Wind Turbine (*Jonkman et al.*, 2009) atop a fixed bottom monopile substructure is simulated. The turbine is operating under constant wind speed and floating freshwater ice loading, as shown in Fig. 1.1. The simulation is to test the new ice module integrated with FAST and to assess the impact of ice forcing on the wind turbine. The wind speed used in the simulations in the following chapters is 8 m/s. The floating ice sheet may have various sizes and geometries, and encounter the tower at $6.57m$ above its bottom. In

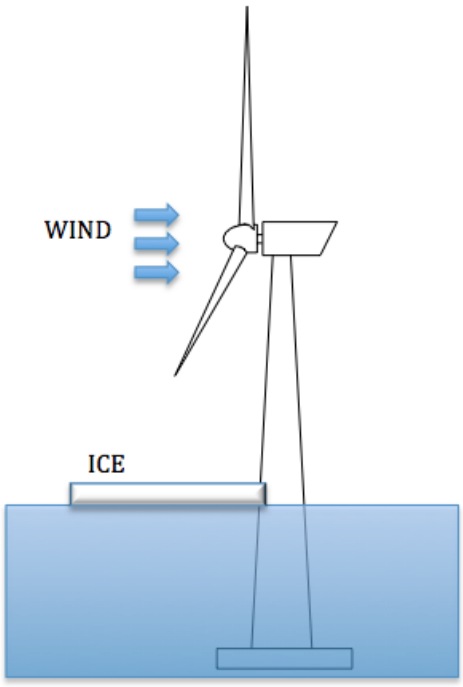

Figure 1.1: Example wind turbine in contact with wind and ice

the simulation examples, the hydrodynamic added mass is not included. We set x as the fore-aft direction of the wind turbine, y as the side-side direction while z is the upward direction. In our simulations, the wind and horizontal ice forces are in the positive x direction, while vertical ice forces are in the z direction.

The tower base moment and tower top displacement are selected to represent the tower response to wind and ice force. When there is no ice, the time history of these two values are shown in Fig. 1.2 and Fig. 1.3. We choose the tower top displacement because when it exceeds a certain value, the normal operation of the rotor may be affected. According to Jonkman (*Jonkman and Buhl Jr.*, 2005), FAST models the tower deflection using a linear modal representation. There are two fore-aft modes and two side-side modes. Each mode shape has the form of a six-order polynomial. The transient vibration at the beginning of simulation is due to the start of turbine operation. We display the transient displacement as a reference to show

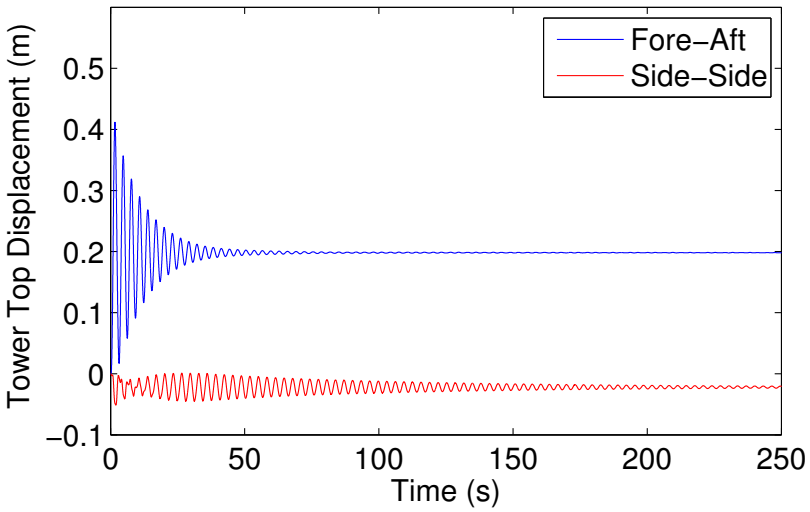

Figure 1.2: Wind turbine tower tip displacement under no ice load

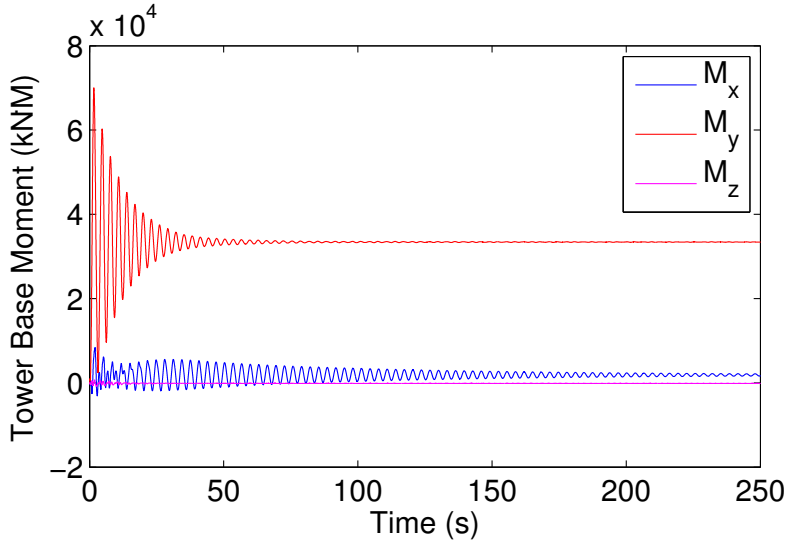

Figure 1.3: Wind turbine tower base moment under no ice load

how significant the structural response is due to ice load. As shown in the tower base moment time history (Fig. 1.3), since we apply wind and ice force both in the x direction, M_y (tower pitching moment or fore-aft moment) is much larger than M_x (tower roll moment or side-to-side moment) and M_z (tower yaw moment or torsional moment).

The ice module includes six ice models based on the characteristics of ice and structure interaction. For each model, users are required to input specific ice parameters, such as ice thickness, temperature and velocity. The module also provides suggested default values for some useful constants, such as Young's modulus of ice. In the following chapters, one sample simulation for each ice model is described.

In Chapter 2, four models applying existing ice mechanics theories to model ice-structure interactions are described. The first model is quasi-static ice loading. The ice force can be prescribed as a function of the characteristics of the ice and structure. Based on the failure mode of ice, this model is divided into two sub-models. One is the creep failure mode, which may happen at a very low velocity. The other is the buckling failure mode, which happens to thin ice sheets. The second model is dynamic ice loading. It models the interaction between ice and compliant structures. In this model, the ice force cannot be prescribed and is influenced by the structural responses. The third model is random ice loading. In this model, the ice force is random due to the randomness of ice characteristics. The fourth model is the impact of ice floes. In this model, the dynamics of the ice floe is modeled and the velocity of the ice is not prescribed but influenced by the ice-structure interaction. The ice force is limited by the momentum of the ice floe, the external environmental driving forces or the splitting failure of the ice.

In Chapter 3, a new analytical model is presented to simulate time-dependent response of structures subjected to ice impact. The ice forces are limited by ice failure with the ice considered to fail in multiple zones non-simultaneously. Non-

simultaneous ice failure is one important failure mode of larger scale ice moving at moderate to high speeds. This model combines previous independent failure zone theory of brittle materials and a dynamic ice-structure interaction model. This model is able to produce an ice load time history, which can be applied to dynamic ice-structure interaction analysis. The model can also generate a pressure-area curve based on the input ice characteristics.

In Chapter 4, a new analytical model that generates time-dependent ice forces on sloping structures due to bending failure is presented. Considering the fact that ice tensile strength is much smaller comparing to its compressive strength, sloping structures, especially conical structures attached to the offshore tower at the water level are widely used to reduce ice forces. This model provides a simplified method to approximate the deformation field of the ice sheet when encountering a sloping structure, and thus calculate the ice force when bending failure happens. A quasi-static ice force time history that describe the change of ice force over time after the bending failure happens is also provided.

In all the models that predict ice load on offshore structures, ice thickness is an important input parameter. To better simulate ice load change over time in reality, it is necessary to establish ice thickness as a function of time and environmental factors. In Chapter 5, several analytical models that predict ice thickness change over time as a function of air temperatures are presented. The factors of heat flux from water, initial ice formation, ice-air heat exchange and ice top surface melting are taken into consideration. The resulting prediction is compared with ice thickness measurement data from Lake Huron.

CHAPTER II

Application of Existing Ice Mechanics Theories in Wind Turbine Response Simulation

2.1 FAST

FAST is the CAE tool maintained by the National Renewable Energy Laboratory (NREL) for simulating onshore and offshore wind turbine systems. NREL's core CAE tool, FAST (*Jonkman and Buhl Jr.*, 2005; *Jonkman*) is based on advanced engineering models derived from fundamental physics, but with appropriate simplifications and assumptions, and supplemented where applicable with computational solutions and test data.

FAST joins AeroDyn (a rotor aerodynamics module) (*Laino and Hansen*, 2002; *Moriarty and Hansen*, 2005), HydroDyn (a platform hydrodynamics module) (*Jonkman*, 2007, 2009) for offshore systems, SubDyn (a multimember substructure finite element module) (*Damiani and Song*, 2013; *Song et al.*, 2013), a control and electrical system (servo) dynamics module, and a structural (elastic) dynamics module to enable coupled nonlinear aero-hydro-servo-elastic analysis in the time domain. The FAST tool enables the analysis of a wide range of wind turbine configurations, including two- or three-blade horizontal-axis rotor, pitch or stall regulation, rigid or teetering hub, upwind or downwind rotor, and lattice or tubular tower. The wind turbine can be

modeled on land or offshore on fixed-bottom or floating substructures.

NREL has recently put considerable effort into improving the overall modularity of FAST to improve the ability to read, implement, and maintain source code, increase module sharing and shared code development across the wind community, improve numerical performance and robustness and greatly enhance flexibility and expandability to enable further developments of functionality without the need to recode established modules (*Jonkman*, 2013). The new FAST modularization framework supports module-independent inputs, outputs, states, and parameters; states in continuous-time, discrete-time, and in constraint form; loose and tight coupling; independent time and spatial discretizations; time marching, operating-point determination, and linearization; data encapsulation; dynamic allocation; and save/retrieve capability. One of the benefits of a modular framework is that it allows modules to be interchanged; this feature is important for benchmarking, research, and industrial applications because the required model fidelity is dependent on the application. The modular framework is implemented in the version 8 of FAST.

The ice module developed and presented in this chapter will become a new module named IceDyn that can be integrated into the FAST modularization framework through loose or tight coupling allowing simulations of offshore wind turbine systems in cold weather under combination of simultaneous wind, wave, current, and ice loading. In the new FAST modularization frame work, the ice module is called by the FAST driver program. At each coupling step, the ice module reads tower displacement and velocity from the structure module through FAST driver program and returns ice force to the FAST driver program. In a loosely coupled time-integration scheme, the ice module tracks its own states (e.g. ice floe displacement and velocity) and integrates its own equations with its own solver. In a tightly coupled time-integration scheme, the ice module sets up its own equations, but the states of the ice module and other modules are tracked and integrated by a solver common to all the modules.

The ice loads on structures are dictated by the failure mode of the ice. The resulting ice forces are dynamic and may be coupled with the structural response. Therefore, in the IceDyn module, we developed ice/structural interaction models that include the effects of ice sheet deformation and failure as well as structural properties and dynamic structural responses. Four models are described in this chapter utilizing existing theories to simulate the ice forces based on characteristics of ice and structure interaction.

2.2 Quasi-static ice loading

In the first model, we considered a stiff support structure of the wind turbine. The relative displacement and velocity between the structure and ice are small. In this case, the ice-structure interaction does not affect the magnitude and period of ice loads. Therefore, the ice loading can be prescribed. Depending on parameters such as ice velocity and ice sheet thickness, ice may fail in different modes. Based on ice failure modes creep and elastic buckling, this model has two sub-models.

2.2.1 Creep

Consider the case of an ice plate of thickness h moving at velocity U past a vertical indenter (the support structure of a wind turbine) of width D. The ice plate is idealized as a semi-infinite sheet presenting its free-edge exactly parallel to, and in perfect contact with, a flat punch indenter. In this sub-model, we consider ice as a creep material flowing around the structure (*Sanderson*, 1988), as shown in Fig. 2.1. The force exerted on the structure as ice moves past can be calculated using Korzhavin equation (*Korzhavin*, 1971):

$$F_{max} = IkmDh\sigma \tag{2.1}$$

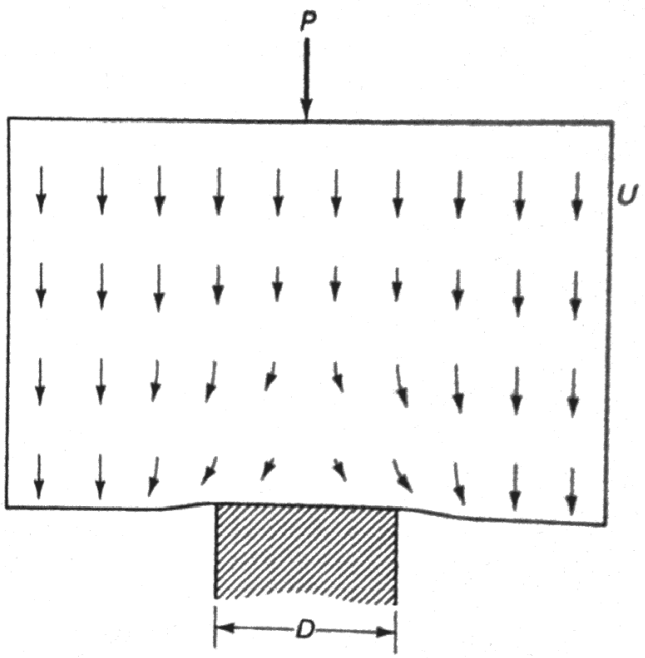

Figure 2.1: Top view of the creep flow field within an ice sheet driven by an external force P, moving with a velocity of U against a structure with a width of D. (*Sanderson*, 1988)

where: I is the indentation factor, and has the range of 1 to 3. k is the contact factor, and has the range of 0.3 (for non-simultaneous failure) to 1 (for simultaneous failure, such as creep) for small scale structures. Meanwhile, Sanderson suggested that contact factor k had to be very low (0.02-0.13) for full-scale structures (*Sanderson*, 1988). The parameter m is the shape factor, and has the value of 0.9 for cylindrical structures and 1 for flat indenter. Michel and Toussaint (*Michel and Toussaint*, 1977) also suggest a different value 2.97 for the product of I, k and m. Ralston (*Ralston*, 1979) suggested a range of 1.15 to 4 depends on the aspect ratio. The users may choose proper values for these parameters according to the specific situation of their ice field and wind turbine structure. σ is the uniaxial compressive strength of ice. The product of Ikm and σ is called effective pressure in some literature.

The uniaxial compressive strength of ice depends on the strain rate. Michel and Toussaint (*Michel and Toussaint*, 1977) proposed that first from the ice velocity U_{ice}

and the diameter of the structure D, calculate $U_{ice}/4D$ or $U_{ice}/2D$ (*Ralston*, 1979) and adopt this as indentation strain rate.

For freshwater ice we also find the relation:

$$\sigma = \left[\frac{1}{A} exp\left(\frac{Q}{RT}\right)\dot{\epsilon}\right]^{1/3} \tag{2.2}$$

where T is temperature in Kelvin. Other constants R, T, Q and A are as suggested by Sanderson (*Sanderson*, 1988).

Before the ice stress reaches the yield stress, we assume ice is under elastic strain. The elastic strain when ice begins to yield can be calculated as:

$$\epsilon_e = \frac{Ikm\sigma}{E} \tag{2.3}$$

where E is the Young's Modulus of ice. We assume constant strain rate, thus the time when the ice begins to yield is

$$T_{rise} = \epsilon_e/\dot{\epsilon} \tag{2.4}$$

Therefore, the time history of ice force in this submodel presumes that the ice force increases linearly over time until T_{rise} and it reaches its maximum limit. After that, the ice force stays constant at its maximum value.

The assumption of pure elastic strain in the loading process is not entirely accurate. According to Sanderson (*Sanderson*, 1988), when ice is subjected to a stress, besides an immediate elastic strain ϵ_e, it also deforms in a transient time-dependent delayed elastic strain ϵ_d and a time-dependent viscous creep strain ϵ_v. Since the ice velocity is small, before the ice fails, there would be enough time for these two types of strains to grow comparable to the elastic strain. And the time to failure when considering the other two strains would be longer. The reason for this simplification

is that the ice load time history is not a cyclic one. When the ice load increases to the maximum, it is assumed to stay constant. Therefore, T_{rise} does not affect the ice-structure interaction mode and thus does not affect the structural response to the maximum ice force.

For ice to fail in this model, the indentation speed calculated from the ice velocity during the loading phase should be within the ductile range of ice. This means the indentation strain rate should be below 10^{-4}. This gives an upper limit of the ice velocity if the contact geometry is known.

One example simulation is presented using user input values as: ice thickness $h = 0.99m$ since during a cold year, the maximum ice thickness in the Great Lakes range from $0.7m$ to $1.2m$. The ice velocity is $U = 0.001m/s$, and structure diameter is $D = 2.7m$ at the water surface. The temperature of the ice is $T = -4°C$. Indentation factors $Ikm = 2.97$ as suggested by Michel and Toussaint (*Michel and Toussaint*, 1977). Other constants are as suggested by Sanderson (*Sanderson*, 1988). According to Eqn. (2.2), $\sigma = 4.8MPa$. According to Eqn. 2.1, the maximum ice force on the structure is $F_{max} = 3.8 \times 10^7 N$ and $T_{rise} = 16.2s$.

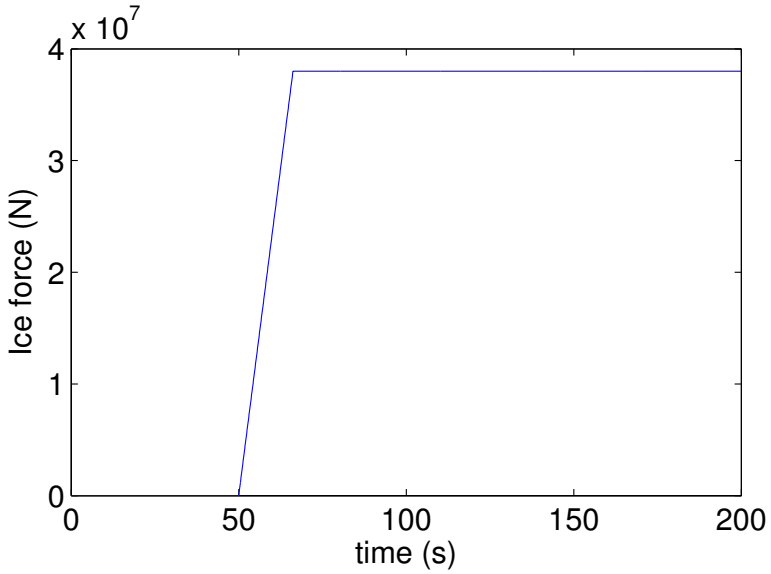

Figure 2.2: Time history of ice loading for ice model 1.1 creep

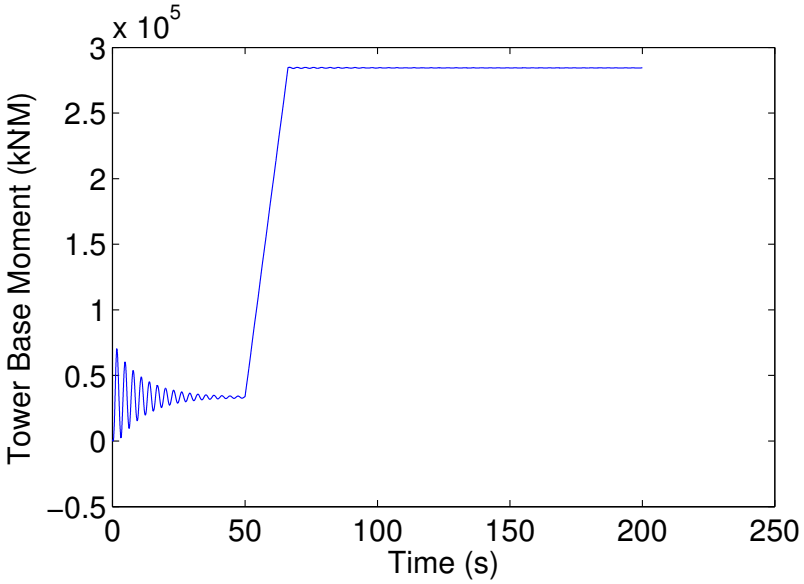

Figure 2.3: Time history of FAST simulated wind turbine tower base moment for ice model 1.1 creep

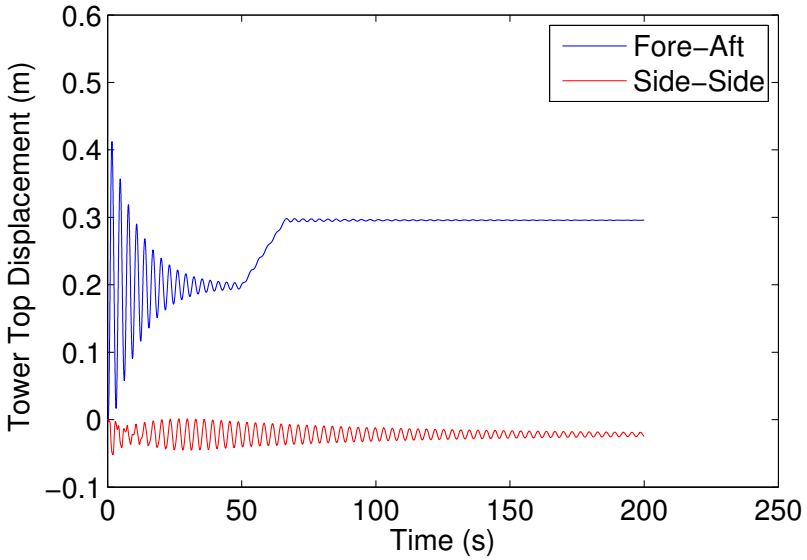

Figure 2.4: Time history of FAST simulated wind turbine tower top displacement for ice model 1.1 creep

The force is added at 50 s after the simulation begins in order to let the transient vibration die out. The time history of ice load and FAST simulation result of the tower base moment and tower top displacement are shown in Fig. 2.2, 2.3 and 2.4. It can be observed that the simulated tower base moment reaches its maximum value at about $t = 50 + 16.2s$. Also, the ice force is placed $6.57m$ height above the tower base. Therefore this maximum tower base moment minus the moment when there is no ice force equals $6.57m \times F_{max}$, which is as expected.

2.2.2 Elastic buckling

In this sub-model, as shown in Fig. 2.5, we assume a truncated wedge-shaped plate of elastic material (ice) floats on an elastic foundation (fresh/sea water) and is loaded at its edge by a total force P distributed over a width D.

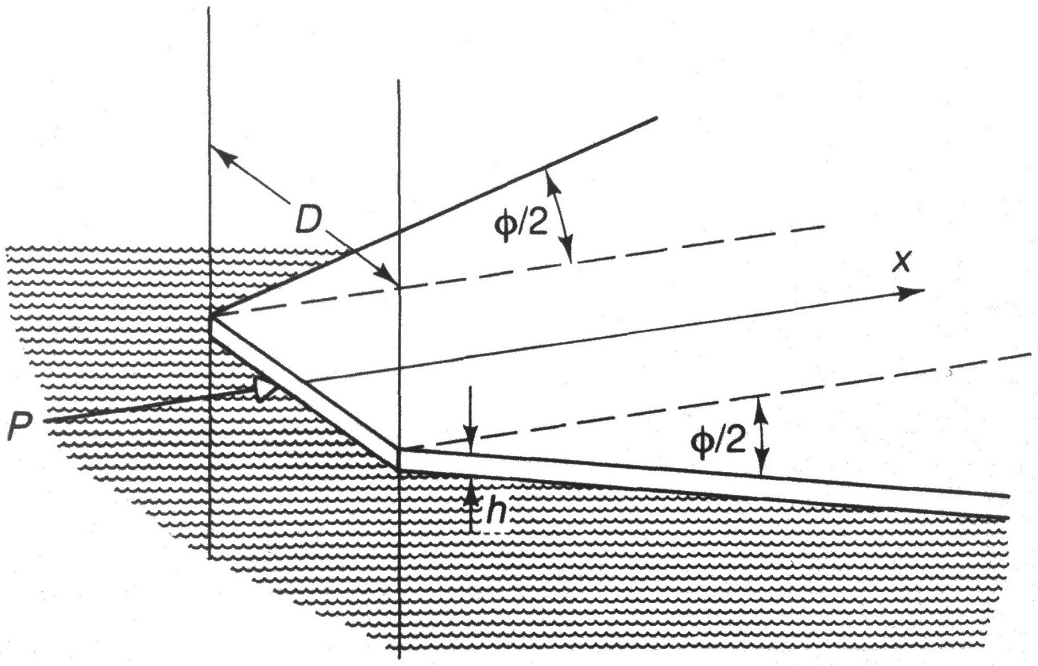

Figure 2.5: Geometry for analysis of elastic buckling, (*Sanderson*, 1988)

The wedge angle ϕ is variable. The plate can be a parallel-sided floating plate

(uniaxial loading) with $\phi = 0$. As ϕ tends to 180°, the plate approaches an infinite half-plane. According to Sanderson (*Sanderson*, 1988), it is usually observed that, the ice sheet interacting with structures, would form radial cracks at angles of around 45° before buckling. Therefore, we set the default value of wedge angle to be 90°.

The solution given by Sanderson (*Sanderson*, 1988) depends on the boundary condition at the loaded edge, where ice and structure interact. For a simply supported edge, which is a more realistic case, the buckling load is given by:

$$P_b = 5.3 B_f \kappa \left(\kappa D + 2tan\frac{\phi}{2} \right) \tag{2.5}$$

where B_f represents the flexural rigidity of the ice cover

$$B_f = \frac{Eh^3}{12\left(1-\nu^2\right)} \tag{2.6}$$

and we define

$$\kappa = \left(\frac{\rho_w g}{4 B_f} \right)^{1/4} \tag{2.7}$$

where ρ_w is the density of water, g is the gravity acceleration, h is the ice thickness, D is the structure width, ν is the Poissons ratio of ice, and E is the Youngs modulus of ice.

Since this is the elastic buckling model, the average stress of ice at buckling and total elastic strain can be calculated as: $\sigma_b = P_b/Dh$, $\epsilon_b = \sigma_b/E$. And the time from loading till buckling is $T_b = \epsilon_b/\dot{\epsilon}$. Also assume T_0 is the time window between the end of one ice sheet buckling and the start of another ice sheet loading. This should be a random number depending on the situation of the ice field.

For ice to fail in this model, buckling should occur before creep or crushing occurs, so the buckling load should be smaller than the ice force when ice fails in creep or brittle mode. Therefore, we have $P_b < P_c$, $C_1 h^{1/2} + C_2 h^{5/4} < \sigma_c$, where C_1 and C_2 are

constants depending on ρ_w, g, ν and E. σ_c is the effective creep or crushing pressure. The above equations give an upper limit for the thickness of the ice sheet.

Let us assume one ice sheet of thickness $0.1m$, is moving at a speed of $0.001m/s$. It is contacting a wind turbine support structure of a diameter $2.7m$ at water surface. The temperature of ice is $-4°C$. The density of the water is $1000kg/m^3$. The buckling load is $2.79 \times 10^6 N$, and the buckle time is $T_b = 11.7s$. And T_0 is assumed to be zero. The calculated ice force in elastic buckling mode is smaller than that calculated in other ice failure modes, such as creep or crushing, using the same parameter values.

The time history resulting from FAST simulation of tower base moment and tower top displacement is shown in Fig. 2.6 and 2.7. It can be seen that both structure responses have a cyclic pattern. The period is about $11.7s$. Also, the maximum tower base moment minus the moment when there is no ice force equals to $6.57m \times F_{max}$. This is as expected for a quasi-static loading case. It can also be seen that both tower base moment and tower top displacement are small comparing to the structure's transient vibration. This is also as expected, since according to Popko et al. (*Popko et al.*, 2012), the buckling of ice does not impose significant forces on a structure thus may not be critical situation for the design of offshore wind turbines.

2.3 Dynamic ice loading

During an ice interaction with a structure, the ice fails in the ductile or brittle modes, depending on the indentation speed. For both modes, the ice force can be prescribed. However, when ice interacts with a compliant structure, or the ice loading frequency is comparable to the natural frequency of the structure, the structural response can be very large and have some feedback on the ice load. In this case, the ice force exerted on the structure can no longer be prescribed.

In this model, we use the mechanical model presented by Matlock et al. (*Matlock et al.*, 1971) and Kar et al. (*Karr et al.*, 1993) to describe the ice-structure interaction

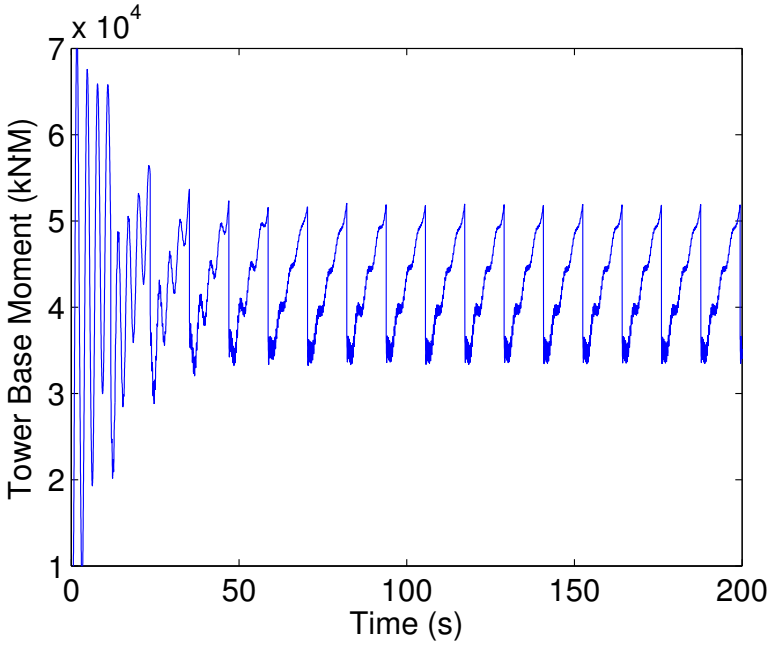

Figure 2.6: Time history of FAST simulated wind turbine tower base moment for ice model 1.2 elastic buckling

process. The ice sheet is represented by a system of brittle elastic bars, as shown in Fig. 2.8.

In this model, the ice sheet consists of a series of ice teeth. The position of the first ice tooth at the beginning of the simulation is denoted as z_0. The ice sheet is assumed to move at a constant speed $\dot{z} = v_{ice}$. The distance between ice teeth is assumed to be a constant value P. Assuming the position of the structure at current time is x, the tip deflection of the current Nth ice tooth can be calculated as:

$$\Delta = \dot{z}t + z_0 - x - P(N-1) \tag{2.8}$$

Each ice tooth exhibits linear elastic deformation when it contacts the structure and before the maximum deflection Δ_{max} is reached. Denote the stiffness of the ice tooth as K_{ice}, then the ice force becomes $K_{ice}\Delta$. When ice tooth does not contact the structure or when it breaks, the ice force becomes zero. Therefore, the ice force can

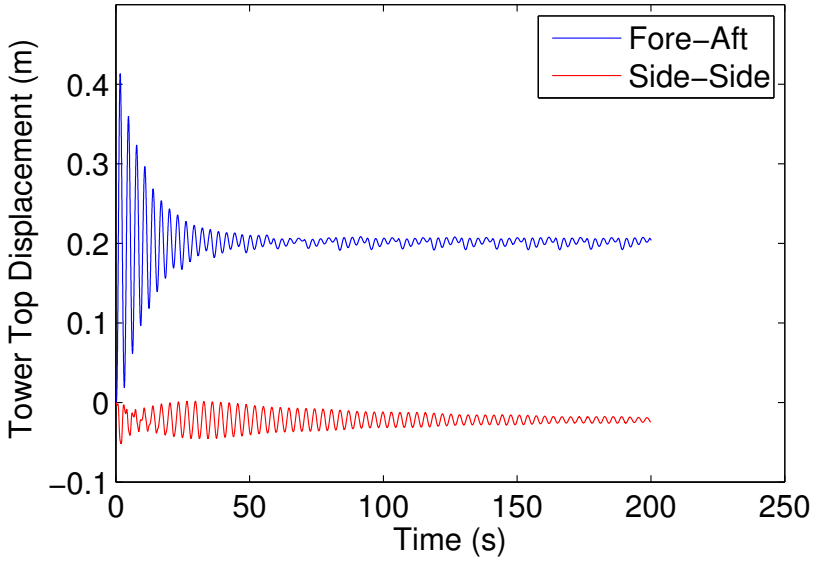

Figure 2.7: Time history of FAST simulated wind turbine tower top displacement for ice model 1.2 elastic buckling

be expressed as

$$F_{ice} = \begin{cases} K_{ice}\Delta, & 0 < \Delta < \Delta_{max}, \\ 0, & \Delta \leq 0, \Delta = \Delta_{max} \end{cases} \tag{2.9}$$

In this model, the user is expected to input the ice sheet thickness, structure diameter, ice pressure, distance between ice teeth and the maximum ice tooth deflection. According to ISO 19906, the stiffness of ice can be calculated as (*BSI*, 2011):

$$F_{max} = Dh\sigma_g \tag{2.10}$$

and

$$K_{ice} = F_{max}/\Delta_{max} \tag{2.11}$$

where σ_g is the global average ice pressure. The FAST program will provide the ice module the current simulation time and structure position. Then based on Eqn. (2.14), the ice module will return the current ice force.

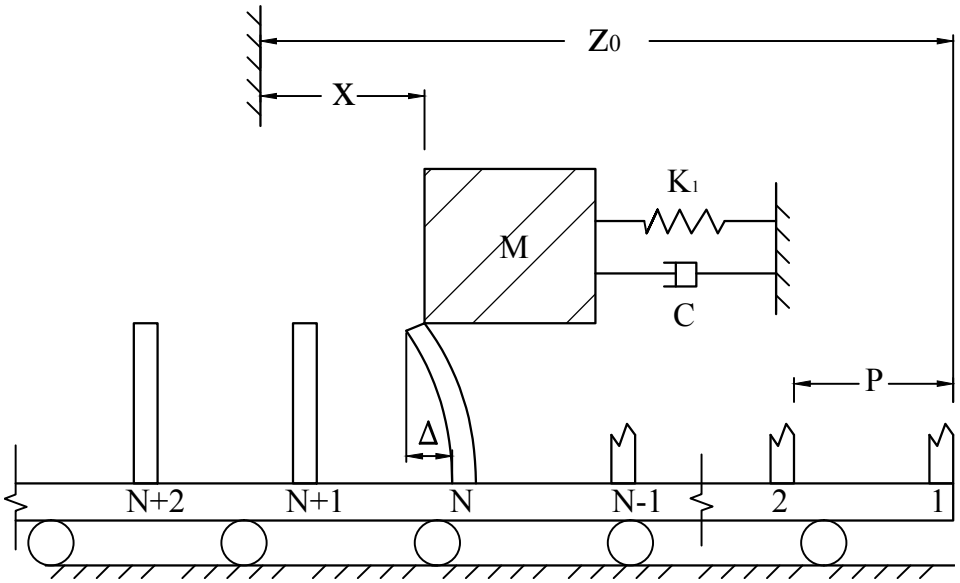

Figure 2.8: Ice structure interaction model (*Karr et al.*, 1993)

One example simulation includes: user input ice thickness $h = 0.99m$, ice velocity $v_{ice} = 0.01m/s$, structure diameter of $D = 2.7m$ at the water surface. The average ice pressure is $\sigma = 10MPa$, distance between ice teeth is $P = 0.1m$, and the maximum elastic deflection is $\Delta_{max} = 0.1m$. The simulated tower base moment and tower tip displacement are shown in Fig. 2.9 and 2.10.

It can be seen from Fig. 2.9 and 2.10 that both structural response are cyclic. It can also be observed that the tower top displacement vibration is continuous and has an amplitude comparable to the transient motion. This result can be used to assess the ice impact on the operation of the rotor as well as in fatigue analysis of the structure.

2.4 Random ice loading

According to ISO standard 19906:2010 (*BSI*, 2011), an ice loading event can be estimated using a deterministic method or a probabilistic method. When the

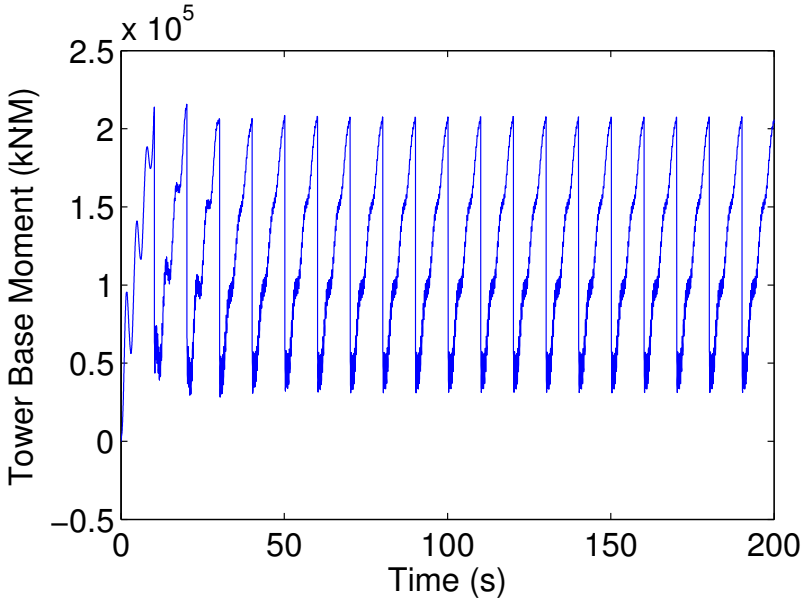

Figure 2.9: Time history of FAST simulated wind turbine tower base moment for ice model 2 dynamic ice loading

indentation speed is high, the ice fails in brittle manner and the ice load exerted on the structure has a random pattern, resulting in random vibration excitation of the structure. Also, according to the previous discussion, the ice force can be influenced by many factors, such as ice thickness, ice drifting speed, ice crushing stress, floe sizes, ice temperature, ice-structure interaction width and others. Most of these parameters usually vary randomly. Therefore, in order to better simulate ice loading events realistically, a random ice loading model is needed. In our ice model 3, based on the ice failure mode, we have three sub-models: the first two are considering ice brittle failure at high indentation speed. This failure mode is known as continuous crushing (*Yue et al.*, 2009). The other is an ice creep failure mode at low indentation speed, with random ice characteristics.

Since there are many factors that influence the ice load, it may become too complicated if we consider random distribution for all of them. As suggested by ISO standard (*BSI*, 2011), we only consider the joint probability distribution of the most important parameters, such as ice thickness, ice sheet drifting speed and ice strength.

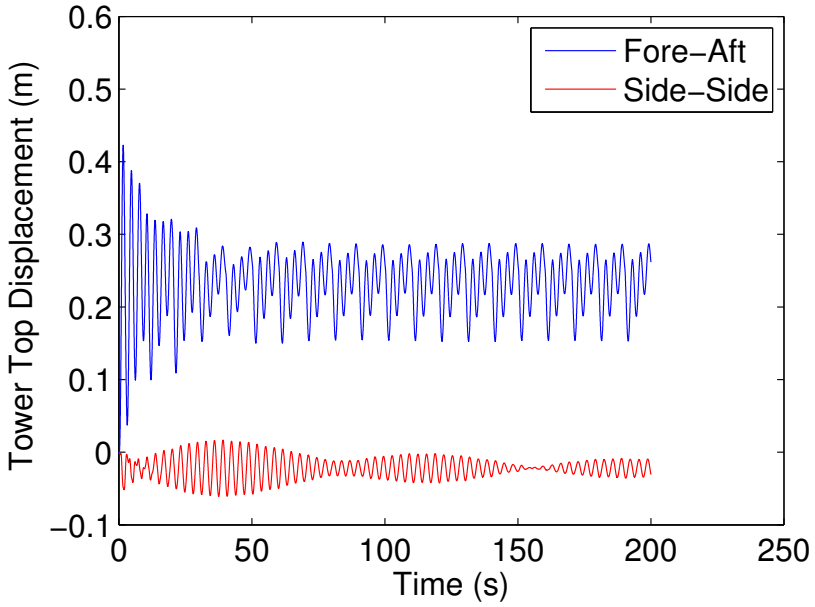

Figure 2.10: Time history of FAST simulated wind turbine tower top displacement for ice model 2 dynamic ice loading

When generating ice loading events, three critical items need to be considered: 1) maximum ice load during one loading event; 2) total ice loading time during one event; 3) time between two loading events. In order to simplify the problem, the following assumptions are made: only a single event is allowed to occur for incremental time intervals; the probability of an event to occur is independent of the probability of any other event; and the requirement of stationarity implies that the probability of an event to occur within a time interval with a given duration must be identical throughout the whole time series.

With the stochastic model of the above three factors, the ice module will be able to generate a random time history of the ice load. At the beginning of the simulation, based on users' input, the program will generate a random event duration, random ice thickness, velocity and/or ice crushing strength. Then a maximum ice force and ice loading time for each event are to be calculated. The time history of ice force within one loading event is generated based on ice failure modes. Then at the end of

one event, the program will generate random parameters for the next event.

2.4.1 Continuous crushing - quasi-static load

When a level ice sheet moves quickly passing a vertical structure, the ice force and structural response both fluctuate randomly. In this condition, the ice sheet is believed to fail in a brittle manner and crushed ice pieces flake, causing variation of the ice force. The failure mode is known as continuous crushing (*Yue et al.*, 2009). This and the next sub-model both assume ice has this failure mode.

This sub-model assumes that the structure is rigid comparing to the ice cover. In this model, ice brittle strength or ice load has a random pattern, while other ice characteristics may be deterministic. For this reason, we treat ice strength as the most important random variable, while leaving the choice of ice thickness and velocity randomness to the user.

There have been many researchers, that studied the random ice strength or ice load. In Christensen's paper, ice properties in the Great Belt in Denmark were analyzed (*Christensen and Skourup*, 1991). Christensen argued that since ice thickness h and ice strength σ were both related to the temperature, they were not fully independent. To circumvent this problem, the product of ice strength and thickness was split into temperature-dependent and temperature independent parts. The difficulty of applying Christensen's method is that when calculating the ice loading time within each loading event, the value of ice strength is needed, but Christensen's method does not estimate ice strength directly. For this reason, also since ice loading time is important for deciding structural response, we may decide to assume ice strength and thickness as independent random variables.

In Suyuthis research (*Suyuthi et al.*, 2012), the maximum ice load within one loading event was assumed to have a Weibull distribution. According to Jordaan (*Jordaan et al.*, 1993), the distribution of ice-induced pressure on a ship hull can be represented

by an exponential distribution. For longer time durations, the distribution might tend to the double-exponential (Gumbel) form. In Kamios research (*Kamio et al.*, 2003), the experimental data of fracture strength of notched ice specimens conformed to the simplest form of two-parameter Weibull distribution.

In our ice module, we would allow the user to input the mean value and variance of ice strength, and specify the type of distribution to apply. Then at the beginning of each loading event, the program will generate a random number of ice strength and based on Eqn. (2.10), calculate the maximum ice force for this event.

According to Sodhi (*Sodhi*, 1998), elastic deformation is dominant in continuous crushing. The elastic strain when ice begins to fail can be calculated as:

$$\epsilon_e = \frac{\sigma_g}{E}$$

where E is the Young's Modulus of ice.

We assume here a constant strain rate. Then the time when the ice begins to fail is

$$T_{rise} = \epsilon_e / \dot{\epsilon}$$

$$T_{rise} = \frac{4D\epsilon_e}{v_{ice}} \tag{2.12}$$

Similar to Suyuthi's study (*Suyuthi et al.*, 2012), we also assume that only a single loading event is allowed to occur for incremental time intervals. This means the structure is contacting with one piece of ice at one time. The probability of an event to occur is independent of the probability of any other event. Under these assumptions, the duration t between sequence events should follow an exponential distribution with probability density function as follows:

$$f_T(t) = \lambda e^{\lambda_t} \tag{2.13}$$

where $1/\lambda_t$ is defined as the expected time between subsequent event. This value will be input by the users.

One example simulation presented here involves the following: user input ice sheet thickness of $0.5m$ and ice velocity of $0.2m/s$. Ice loading event duration has a mean value of $1s$. The ice strength has a Weibull distribution with a mean value of $10MPa$ and a variance of $1MPa^2$. The wind turbine support structure has a diameter $2.7m$ at the water surface. The temperature of the ice is $-4°C$. The simulated tower base moment and tower top displacement are shown in Fig. 2.11 and 2.12.

In this example, the expected value of ice force is $1.33 \times 10^7 N$. The expected tower base moment is thus $1.33 \times 10^7 N \times 6.57m + 3.347 \times 10^7 N{\cdot}m = 1.2 \times 10^5 kN{\cdot}m$. It can be seen from Fig. 2.11 that most maximum tower base moments are around $1 \times 10^5 kN{\cdot}m$. The tower top displacement vibrates with a small amplitude about a mean value the same as in the no ice case. This is expected for the static load case, since although the expected ice load is not small, the loading frequency is high comparing to the natural frequency of the structure. Therefore the resulted structural vibration is small.

2.4.2 Continuous crushing - dynamic load

The second sub-model considers interaction between a compliant structure and a ice cover moving at high velocity. In this model, although the compliant structure movement will reduce the relative velocity between the ice and structure, we still assume that there is not enough time for the primary or secondary creep strain to form (*Sodhi*, 1998). Therefore, here we can apply the brittle elastic ice bars model used in ice model 2. The randomness of the continuous crushing mode is reflected in the random ice teeth properties, such as ice brittle strength, distance between ice teeth and the maximum ice tooth deflection.

We apply the Weibull distribution to describe ice brittle strength, as suggested in

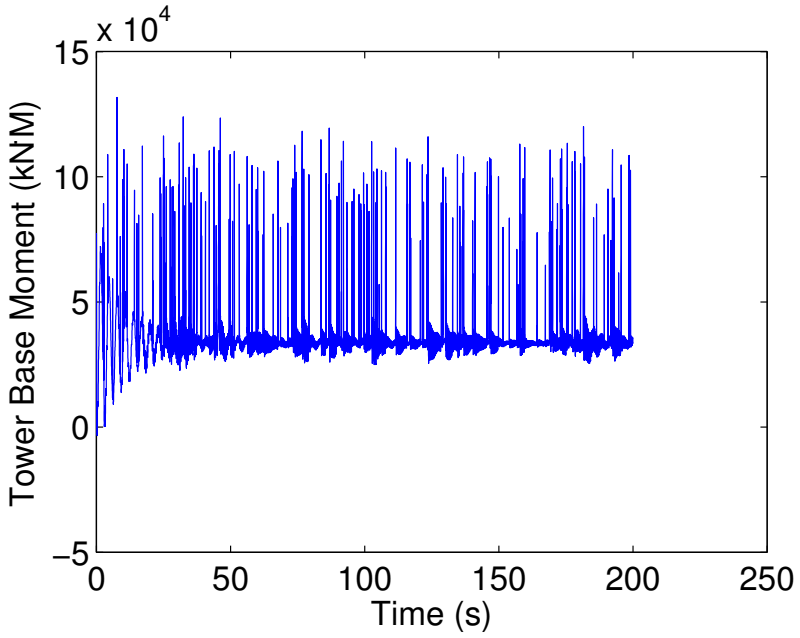

Figure 2.11: Time history of FAST simulated wind turbine tower base moment for ice model 3.1 static random ice loading

the previous sub-model and calculate ice tooth stiffness K_{ice} using Eqn. (2.11). We apply normal distribution to describe distance between ice teeth and the maximum ice tooth deflection. The ice force exerted on the structure when it is in contact with the Nth ice tooth can be expressed as:

$$F_{ice} = \begin{cases} K_{ice,N}\Delta, & 0 < \Delta < \Delta_{max,N}, \\ 0, & \Delta \leq 0, \Delta = \Delta_{max,N} \end{cases} \tag{2.14}$$

$$\Delta = \dot{z}t + z_0 - x - \sum_{n=1}^{N-1} P_n \tag{2.15}$$

At the beginning of the simulation, the program generates the random ice brittle strength, distance of the next ice tooth and the maximum tooth deflection for the first ice tooth. Then when one ice tooth breaks, the program will generate a set of random properties for the next ice tooth. For this model, the user is expected to input mean value and variance of the ice brittle strength, distance between ice teeth

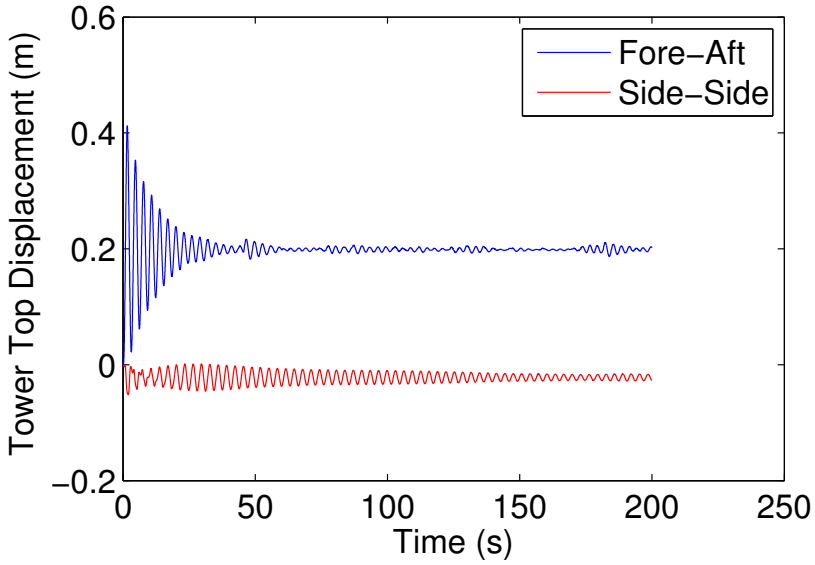

Figure 2.12: Time history of FAST simulated wind turbine tower top displacement for ice model 3.1 static random ice loading

and the maximum ice tooth deflection and determined values of ice thickness and structure diameter.

One example simulation presented here involves the following: user input ice sheet thickness of $0.99m$, and ice velocity of $0.2m/s$. The ice strength has a Weibull distribution with a mean value of $10MPa$ and a variance of $1MPa^2$. The distance between ice teeth has a normal distribution with a mean value of 0.4m, and a standard deviation of 10% of its mean value. The maximum elastic deflection has a normal distribution with a mean value of $0.2m$ and a standard deviation of 10% of its mean value. The wind turbine support structure has a diameter $2.7m$ at the water surface. The temperature of the ice is $-4°C$. The simulated tower base moment and tower top displacement are shown in Fig. 2.13 and 2.14. Fig. 2.15 shows tower base moment time history between $t = 60s$ and $90s$.

It can be observed from Fig. 2.15 that the ice load is cyclic with random maximum value. Since the maximum elastic deformation of ice teeth has a smaller mean value than the distance between ice teeth, there will be free vibration of the structure

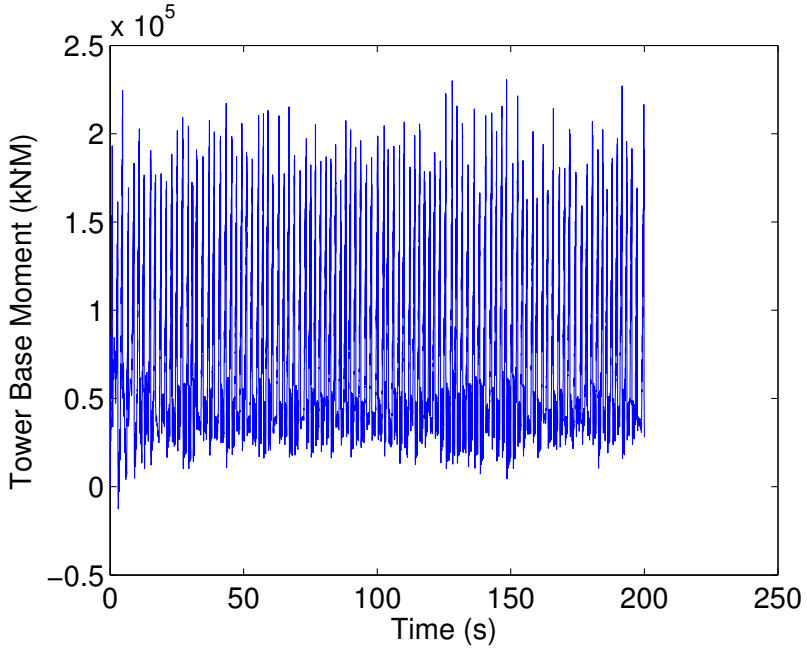

Figure 2.13: Time history of FAST simulated wind turbine tower base moment for ice model 3.2 dynamic random ice loading

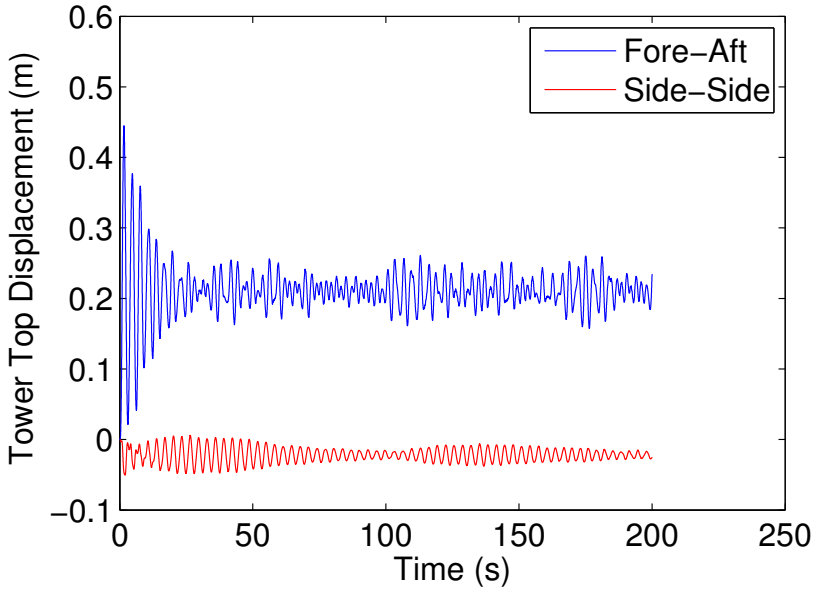

Figure 2.14: Time history of FAST simulated wind turbine tower top displacement for ice model 3.2 dynamic random ice loading

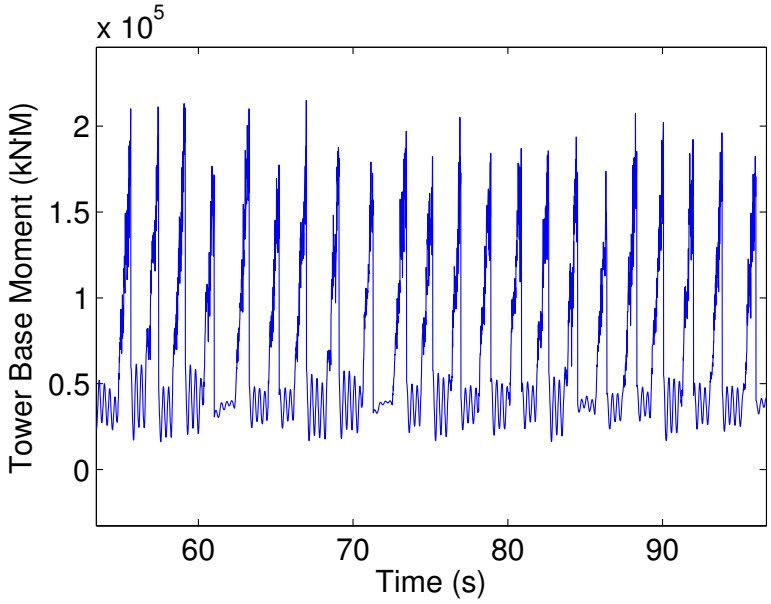

Figure 2.15: Time history of FAST simulated wind turbine tower base moment for ice model 3.2 dynamic random ice loading

between its contact with sequential ice teeth. Fig. 2.15 shows this expected result. It can be seen from Fig. 2.14 that the tower vibrates continuously about its mean position with random amplitude. This result can be used in fatigue analysis of the structure.

2.4.3 Creep

The random ice model can also be applied to other ice failure modes with random ice properties. For example, when ice fails in creep mode, according to previous discussion in model 1, the maximum ice force depends on the ice velocity v_{ice} and thickness h. In this case, we consider these two parameters as random variables and all the other parameters such as D, R, T_{ice} determined as constants. In the current research, v_{ice} and h are assumed independent random variables.

Some previous researchers have studied the random ice properties. Both Leira (*Leira et al.*, 2009) and Liu (*Liu et al.*, 2009) used lognormal distribution to model

ice thickness data:

$$p_H(h) = \frac{1}{\sigma h\sqrt{2\pi}} exp\left[-\frac{1}{2}\left(\frac{lnh-\mu}{\sigma}\right)^2\right] \tag{2.16}$$

with a mean value of $exp(\mu + \sigma^2/2)$ and a variance of $[exp(\sigma^2) - 1]exp(2\mu + \sigma^2)$.

Liu (*Liu et al.*, 2009) applied a Rayleigh distribution to describe ice velocity:

$$p_V(v) = \frac{v}{\sigma^2} exp\left(-\frac{v^2}{2\sigma^2}\right) \tag{2.17}$$

with a mean value of $\sigma\sqrt{\pi/2}$ and a variance $\sigma^2(4-\pi)/2$.

In this model, the user will input the mean value and variance for ice thickness and ice velocity. We apply lognormal distribution for ice thickness and Rayleigh distribution for ice velocity. For each ice loading event, from these random distributions, a random ice thickness and ice velocity are independently generated. Then based on Eqn. (2.2) and (2.1), the calculated maximum ice force for the current ice loading event is determined. The methods of calculating ice loading time and generating loading event time are the same as in the continuous crushing model.

For this example simulation we have: user input ice sheet thickness has a mean value of $0.5m$ and a variance of $0.04m^2$. Ice velocity has a mean value of $0.001m/s$ and a variance $10^{-6}m^2/s^2$. Ice loading event duration has a mean value of $15s$. The wind turbine support structure has a diameter $2.7m$ at the water surface. The temperature of the ice is $-4°C$. The simulated tower base moment and tower tip displacement are shown in Fig. 2.16 and 2.17.

It can be seen from Fig. 2.16, the simulated tower base moment and ice loading time are highly variable. This is expected since there are many random variables in this case. The tower top displacement time history basically follows the pattern of tower base moment.

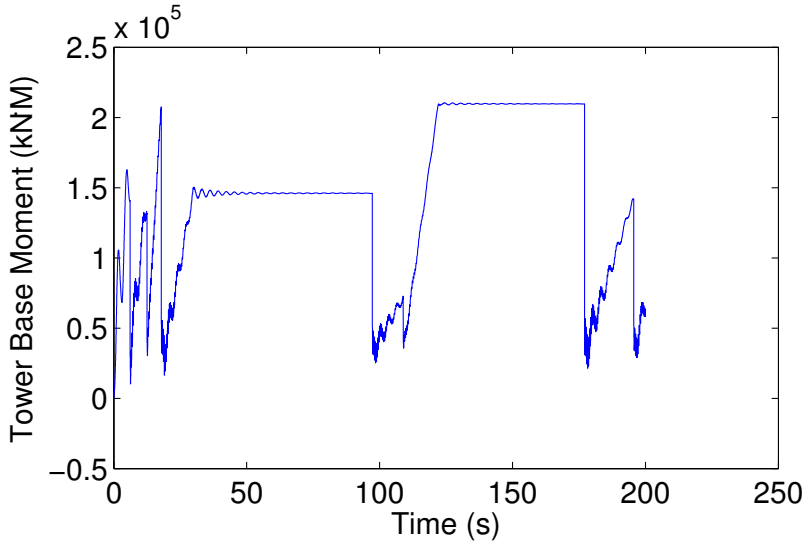

Figure 2.16: Time history of FAST simulated wind turbine tower base moment for ice model 3.3 creep with random ice properties

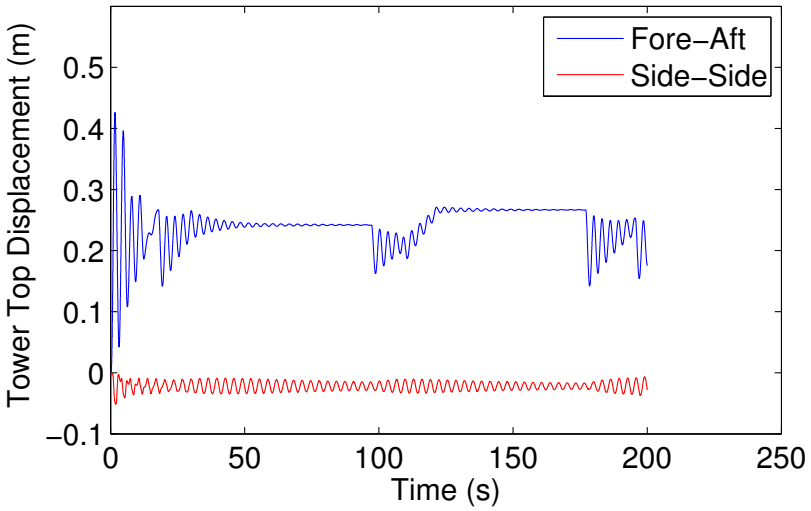

Figure 2.17: Time history of FAST simulated wind turbine tower top displacement for ice model 3.3 creep with random ice properties

2.5 Impact of isolated ice floe

All the previous models assume that ice constantly moves forward. The interaction between ice and the structure does not influence the velocity of the ice. The dynamic characteristics of the ice mass are not taken into consideration. In this model, the impact from an isolated ice floe is studied, which is a dynamic phenomenon. As the floe collides head-on with the structure, local ice failure takes place at the ice structure interface, and the floe decelerates from its initial velocity. As the structure penetrates the ice, the area of contact and the ice force increase while the floe velocity decreases until it stops in front of the structure, bounces back or splits into two or more large pieces and rotate around the structure (*Bhat*, 1988). If an external driving force exists, such as wind or wave force, the ice floe may continue to move against the structure with reduced velocity causing continuous crushing ice loads on the structure.

To study the change of ice force overtime during the impact of an ice floe, we first assume a rectangular isolated ice floe, with length L, width W and constant thickness h. It impacts our wind turbine tower with an initial velocity v_0. The tower waterline section has a radius of R, as shown in Fig. 2.18

When the ice floe collides with the structure, there will be local crushing at the ice-structure interface. As the structure penetration depth x increases, as shown in Fig. 2.19, the ice structure contact area width b increases as well.

According to design rule ISO 19906 (*BSI*, 2011) and many previous field measurements (*Johnston et al.*, 1998), the ice crushing strength is a function of contact area. The pressure-area relation has a general form:

$$P = CA^d \tag{2.18}$$

The ice-structure contact area A depends on the structure penetration depth $x(t)$,

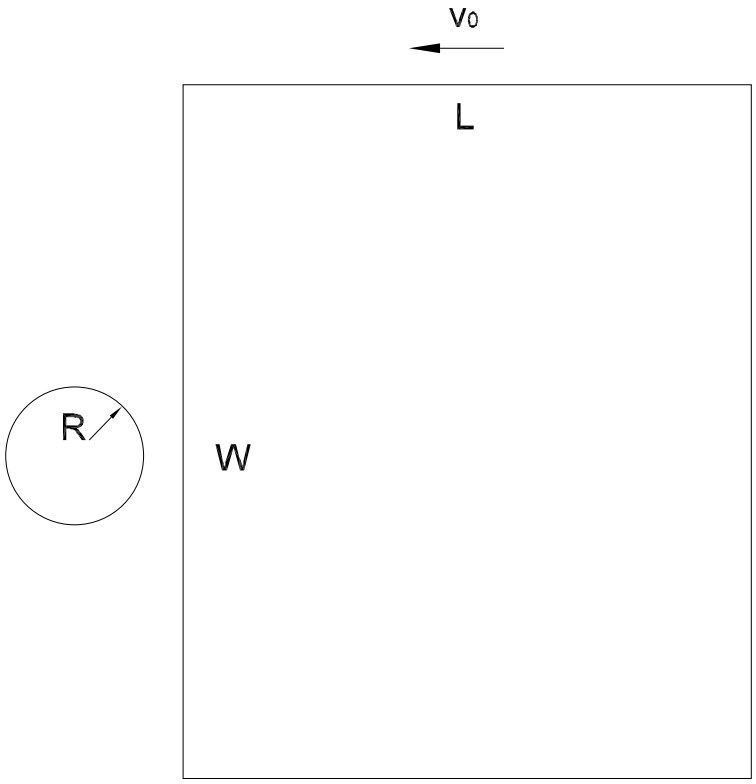

Figure 2.18: An isolated ice floe impacting a wind turbine tower

which is the relative displacement of ice and structure:

$$x(t) = x_{ice}(t) - x_{str}(t) \tag{2.19}$$

Then the contact area can be calculated as

$$A(t) = b(t)h \tag{2.20}$$

$$b(t) = 2\sqrt{R^2 - [R - x(t)]^2} \tag{2.21}$$

Also, it should be noted that when $x_{ice} - x_{str} \geq R$, $b(t)$ reaches its maximum value R.

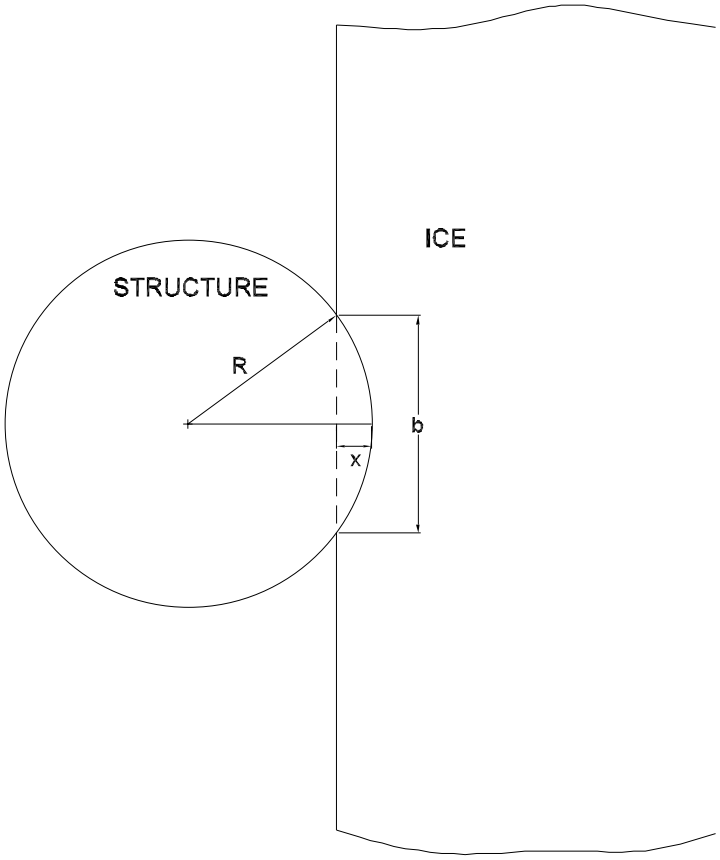

Figure 2.19: Ice structure interface area changes as the penetration increases

Therefore, the time-dependent ice force can be calculated as

$$F_{ice} = \begin{cases} CA(t)^{d+1} & x_{ice} > x_{str} \\ 0 & x_{ice} \leq x_{str} \end{cases} \tag{2.22}$$

$$F_{ice} = \begin{cases} 0 & x_{ice} - x_{str} \leq 0 \\ C\left\{2h\sqrt{R^2 - [R - (x_{ice} - x_{str})]^2}\right\}^{d+1} & 0 < x_{ice} - x_{str} \leq R \\ C\left(2hR\right)^{d+1} & x_{ice} - x_{str} > R \end{cases} \tag{2.23}$$

The ice displacement x_{ice} is decided from the ice floe motion, which is governed

by equations:

$$m_{ice}\ddot{x}_{ice} = \begin{cases} F_{dr} & x_{ice} - x_{str} \leq 0 \\ -C\left\{2h\sqrt{R^2 - \left[R - (x_{ice} - x_{str})\right]^2}\right\}^{d+1} + F_{dr} & 0 < x_{ice} - x_{str} \leq R \\ -C\left(2hR\right)^{d+1} + F_{dr} & x_{ice} - x_{str} > R \end{cases} \tag{2.24}$$

$$x_{ice}(t=0) = 0 \tag{2.25}$$

$$\dot{x}_{ice}(t=0) = v_0 \tag{2.26}$$

where F_{dr} is the external driving force with positive direction in the direction of ice initial velocity. And m_{ice} is the mass of the ice floe. It can be calculated as

$$m_{ice} = \rho_{ice} LWh \tag{2.27}$$

Meanwhile, the structure displacement x_{str} is calculated by the FAST main program and read by our ice module as an input.

As the structure penetrates the ice, the contact force between ice and structure increases as the contact area increases. If the force reaches a value large enough to cause the splitting failure, the ice force will drop to zero after the ice splits and rotate around the structure.

Many previous researches have studied the limit force when the splitting happens. According to the study of Wierzbicki and Karr (*Wierzbicki and Karr*, 1987), macro crack initiation can occur at extremely low loads. Therefore, it can be assumed that short radial cracks will occur in any real ice structure interaction in the brittle regime (*Bhat*, 1988). Then the splitting failure happens when the propagations of those initial cracks become unstable. Here we applied the general form of splitting force P

given in the research by Baht et al. (*Bhat*, 1988) (*Bhat et al.*, 1991):

$$P = \tilde{P} h K_{IC} \sqrt{L} \tag{2.28}$$

where h is the ice thickness. L is the length a square floe or can be the radius of a circular floe. K_{IC} is the fracture toughness of ice. $\tilde{P}$ is the non-dimensional splitting load. It can different values based on different material assumptions and the conditions of indentation. To make a conservative prediction of ice load, we set a default value $\tilde{P} = 3.3$, which is given by Bhat et al. (*Bhat*, 1988) generated from Finite Element Method and returns the largest value of splitting load. But the users have the freedom to input the value of $\tilde{P} = 3.3$.

Two example simulations are given for this model. The user input ice thickness is 0.8 m. ice mass density is 900 kg/m^3. ice crushing strength has a pressure-area relationship as $P = 5A^{-0.5}$. The structure has a radius of 3 m. Fracture toughness of ice has a value of 140 $kN/m^{3/2}$. Non dimensional splitting load is 3.3.

The first simulation assumes an ice square floe with length 1000 m. The ice floe has an initial velocity of 0.5 m/s and is under an external driving force of 11 MN. The simulated ice force and structure displacement are shown in Fig. 2.20 and 2.21.

The second simulation assumes an ice square floe with length 800 m. The ice floe has an initial velocity of 0.5 m/s and is under an external driving force of 9 MN. The simulated ice force and structure displacement are shown in Fig. 2.22 and 2.23.

In the first simulation, the ice sheet fully envelopes the structure and is pushed moving forward under the external driving force. The ice fails in crushing at the ice-structure contact face and the contact force becomes constant since the contact area reaches a constant value. And the structure tends to a constant displacement. In the second simulation, the ice fails in splitting and rotate around the structure. The ice-structure contact force suddenly drops to zero. It can be seen from these two

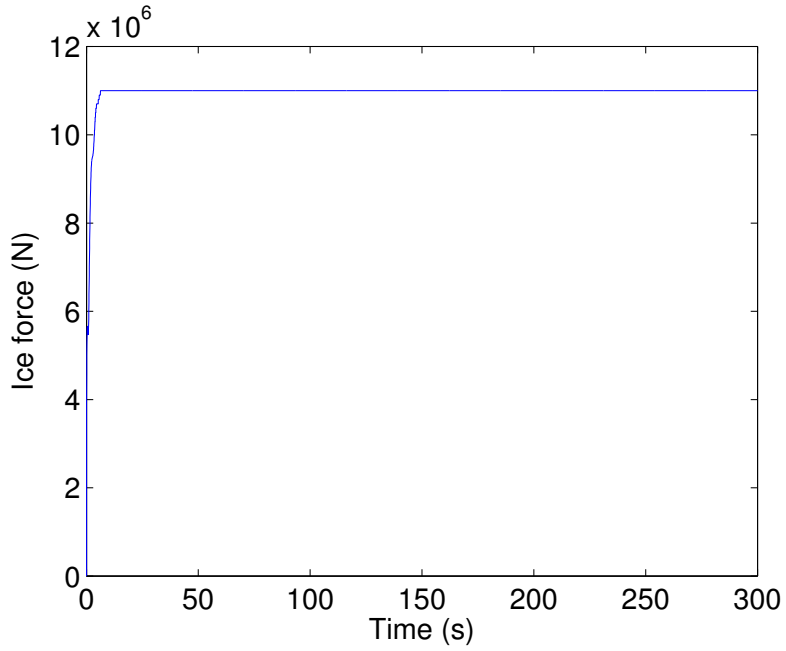

Figure 2.20: Time history of ice force for ice model 4 isolated ice floe impact, case 1

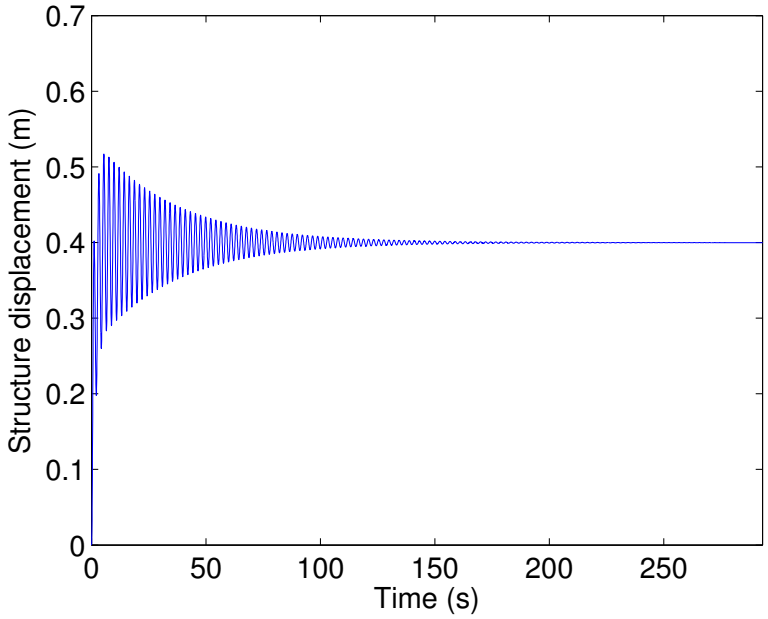

Figure 2.21: Time history of structure displacement for ice model 4 isolated ice floe impact, case 1

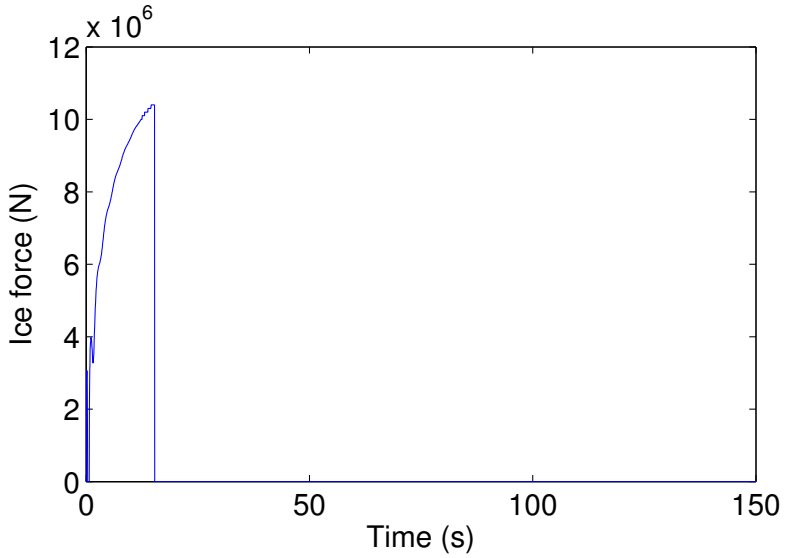

Figure 2.22: Time history of ice force for ice model 4 isolated ice floe impact, case 2

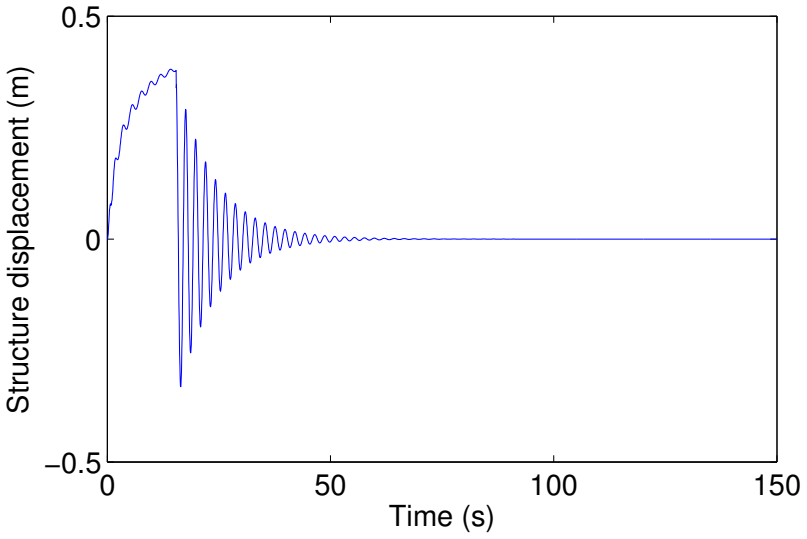

Figure 2.23: Time history of structure displacement for ice model 4 isolated ice floe impact, case 2

simulations that depending on different ice floe sizes and driving forces, ice may have different failure modes.

2.6 Conclusion: Model 1 through 4

Computer-Aided Engineering tools are needed that are capable of modeling the design-driving loads that will interact with an offshore wind turbine system during operation, to allow for innovation of long-term solutions for offshore wind turbines in a variety of environmental conditions. This chapter describes efforts to augment existing CAE tools used for offshore wind turbine analysis with a new module that can provide simulation capability for ice loading on the system. This is accomplished by creating an ice-loading module coupled to FAST, the CAE tool maintained by the National Renewable Energy Laboratory, for simulating onshore and offshore wind turbine dynamics.

The new module includes both static and dynamic ice loading that can be applied during a dynamic simulation of an offshore wind turbine. This new module adds to the existing capabilities that consider combined loading from wind, waves, current, and seismic base motions. Existing ice loading standards are used as guides to establish design considerations for static and dynamics ice loading. This chapter focuses on the development of an ice loading module based on loading scenarios applicable to Great Lakes ice features with due modifications of the existing standards. Of particular importance is the development of new ice/structure interaction models which include effects of ice sheet deformation and failure coupled with the dynamic response of the turbine structure.

The more complex interaction between ice and multi-pile structures creates the need for more complex ice-loading models that go beyond the simple static load cases. The loading module described here includes ice dynamics models based on ice mechanics models that incorporate ice floe forcing, deformation, and failure. Presented

are a quasi-static ice crushing model, a random vibration model with brittle ice deformation, a dynamic ice/structure interaction model and a dynamic ice floe impact model that considers splitting failure of ice.

Two additional models are also given in the following chapters including a multiple failure zone model and an ice bending model for sloping structures.

CHAPTER III

An Ice-Structure Interaction Model for Non-Simultaneous Ice Failure

3.1 Introduction

It has been widely observed that during full-scale ice crushing against structures at medium to high speed, global ice pressures are significantly lower than local ice pressures (*Dempsey et al.*, 2001; *Johnston et al.*, 1998). Many previous ice-loading data, with different scales ranging from laboratory tests to full-scale ice-structure interactions, indicate a trend of decreasing pressure with increasing area (*Johnston et al.*, 1998; *Sanderson*, 1988). One explanation is that the ice failure occurs non-simultaneously in discrete local zones. As shown in Fig. 3.1, due to irregular ice-structure contact, although crushing may appear to be occurring over the full width D, at any one time, it is likely to concentrate in a few zones of width d_i (*Sanderson*, 1988).

Many previous researches addressed this problem by discussing the formation and distribution of the high-pressure zones. Dempsey et al. (*Dempsey et al.*, 2001) found that for medium indentation speeds, direct ice-structure contact occurred through a line-like high-pressure zone distributed along the width of the indenter. Johnston et al. (*Johnston et al.*, 1998) provided quantified estimation of high-pressure zones

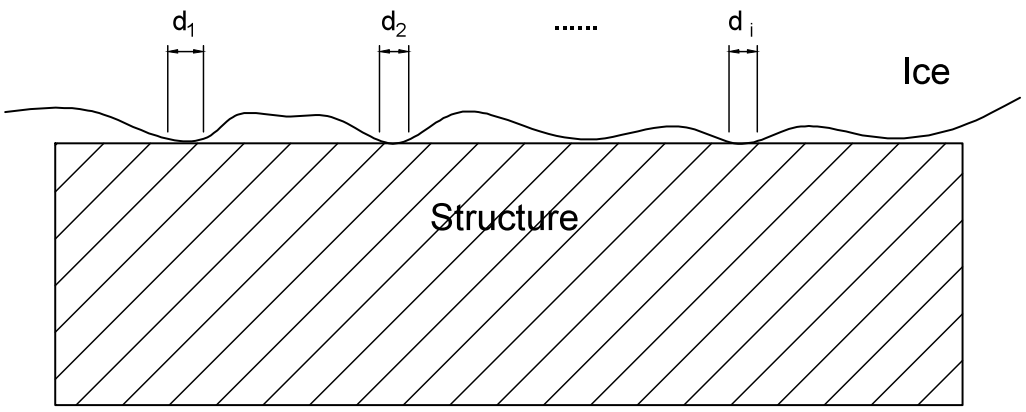

Figure 3.1: A schematic representation of non-simultaneous failure

parameters, such as zonal size, force, pressure, and spatial density and examined the estimation with data from medium-scale indentation tests, ship ramming trials of the Louis S. St. Laurent and CanMar Kigoriak, and icestructure interaction with the offshore structure Molikpaq. The measured data showed that the high-pressure zones distributed randomly and transferred from one location to another, but the distribution was affected by both the extrusion of crushed ice and spalling.

Some other research addressed the uneven contact surface. Baht (*Bhat*, 1990) proposed the idea of a fractal ice edge profile in which the finite failures would generate fractal surfaces. According to Palmer et al. (*Palmer and Sanderson*, 1991), fragments of crushed ice were found to have a fractal size distribution. Meanwhile, Kry (*Kry*, 1980) divided the interaction width into a number of statistically independent and equivalent zones. Ashby et al. (*Ashby et al.*, 1986) divided the whole contact area into N independent zones and estimate the total force across the contact area based on pressure in each failure zone. Daley et al. (*Daley et al.*, 1998) looked at discrete local ice failure as wedge-shaped ice blocks crushing against indentors. This provided

reference for studying the ice failure in a single failure zone. In one of Daleys later studies (*Daley*, 2007), two types of pressure-area data were discussed. One described the way that pressure was distributed within the area of the contact zone, termed spatial pressure-area. The other described how the average pressure within the nominal area changed as the indentation grew, termed process pressure-area. For spatial pressure distribution, the average pressure decreased as the measured area increased. For process pressure distribution, however, Daley argued that there was a trend of increasing pressure as the contact area increased. In this chapter, we mainly look at spatial pressure distribution.

Most previous research focused on estimating total ice force and average ice pressure for the purpose of designing coastal and offshore structures. However, for some offshore structures, the dynamic nature of ice loading is also of interest. One potential application of the non-simultaneous ice failure model is offshore wind turbine designs. Due to the consideration of wind resource, availability of transmission systems and adjacency to energy demand, many potential wind farm locations are in cold regions, such as Baltic Sea in the Europe and the Great Lakes in the US (*BOEM*, 2013). The potential impact of floating ice in the winter exerts great challenge to the development of offshore wind farms in these areas. Static ice loads can be very large and the ice-induced vibration of the whole system (foundation, tower and wind turbine) can also be severe. Such challenges raise the demand of modeling capacity of dynamic wind turbine response under the joint action of ice, wind, wave and current.

As a result, for design and analysis of some offshore structures, a time-dependent ice-loading model is needed. In this chapter, a new analytical model on ice non-simultaneous failure that combines the independent failure zone theory of brittle materials (*Ashby et al.*, 1986) and a dynamic ice-structure interaction model (*Matlock et al.*, 1971; *Karr et al.*, 1993) is developed. This model is a recent addition to a new ice module for FAST, which is a widely used open-source simulation software for

wind turbines. This ice module is developed to assess the dynamic response of turbine structures subjected to ice loads (*Yu and Karr*, 2013). The non-simultaneous ice failure model is then integrated into FAST and numerical simulation results of a sample wind turbine responding to the time-dependent ice load are presented. The model also generates a relation that shows the trend of decreasing pressure corresponding to increasing contact area. Besides pressure area relationships, the resulting pressure dependence on various parameters is also studies, such as independent zone size, shape and strength.

3.2 Non-simultaneous ice failure model

As stated in the independent failure zone theory by Ashby et al (*Ashby et al.*, 1986), the interaction between an ice block of thickness h and a structure of width D is studied. The irregular contact area with dimension $h \times D$ is divided into a set of small zones with dimensions $L_i \times L_i$, as shown in Fig. 3.2. The contact surface within each zone is assumed to be flat and have a random initial position relative to the structure, as shown in Fig. 3.3.

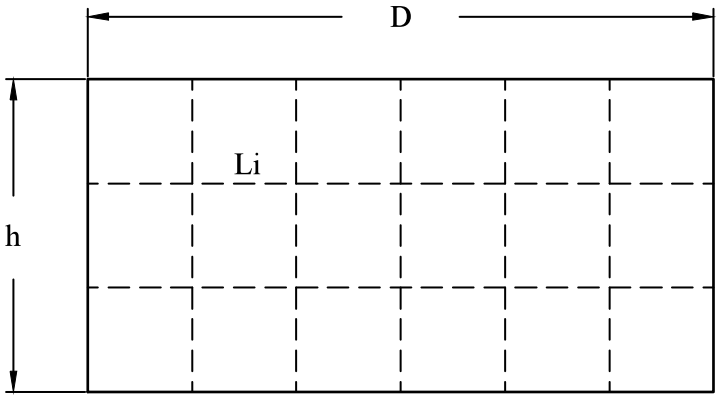

Figure 3.2: The partition of independent failure zones across the contact area between an ice block of thickness h and a structure of width D (front view)

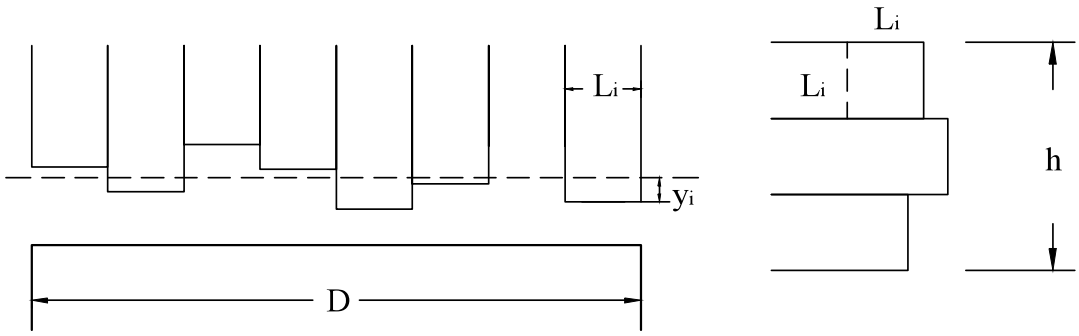

Figure 3.3: Distribution of independent failure zones along the width and height of the contact surface (left: top view; right: front view)

As shown in Fig. 3.4, each zone represents a small ice cell. In this theory, it is assumed that each small cell fails independently. For this reason, the small zones are given the name independent failure zones. As each cell comes into contact with the structure, the cubical cell is first under elastic deformation. When the deformation reaches a critical value Δ_L, the cell fails. An ice cube with a volume of L_i^3 is crushed and cleared out of the contact surface while other zones are not affected. The ice block has to travel forward a distance L_i before the next cell within the same zone contacts the structure. Under such assumptions, at any time, only a subset of all the independent zones is in contact with the structure. This results in a reduction of the average ice pressure from that of simultaneous failure.

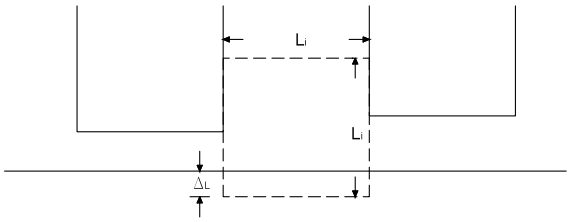

Figure 3.4: When a single zone deforms Δ_L, the ice cube of dimensions L_i^3 fails independently (*Sanderson*, 1988)

In Ashbys model, the position of each zone is independently and randomly distributed. For each zone, the possibility of its contacting the structure at one time incident is uniform:

$$p = \Delta_L / L_i \tag{3.1}$$

Therefore, the total number of zones n contacting the structure at any time is defined by a binomial distribution. The probability density function of n is:

$$f(n) = \binom{N}{n} p^n (1-p)^{N-n} \tag{3.2}$$

where N is the total number of independent failure zones:

$$N = Dh / L_i^2 \tag{3.3}$$

Ashby et al. selects three-standard-deviation levels to approximate the peak force. At one time instant, if p is small, the maximum number of zones simultaneously in active contact is approximately:

$$n_{max} = Np + 3(Np)^{1/2} \tag{3.4}$$

The pressure required to fail a single cell is denoted as σ_L. The peak load is:

$$F_{peak} = n_{max} \sigma_L L_i^2 \tag{3.5}$$

And the maximum indentation pressure P is calculated by averaging the peak force over the total contact area:

$$P = \frac{F_{peak}}{A} = \frac{\sigma_L \Delta_L}{L_i} \left[1 + 3 \left(\frac{L_i^3}{A \Delta_L} \right)^{1/2} \right] \tag{3.6}$$

where $A = Dh$ is the total contact area.

One of the shortcomings of this model is that the selection of three standard deviations level to approximate peak force is arbitrary. And since the position of each failure zone is random, there is no control of the roughness of the ice-structure contact face. Also, only the average pressure at the peak load is calculated. In the new ice module, we have developed a time-dependent ice-loading model based on Ashbys theory and a dynamic ice-structure interaction model (*Matlock et al.*, 1971; *Karr et al.*, 1993). We also control the irregular ice-structure contact shape by assigning a normal distribution to generate the failure zones positions.

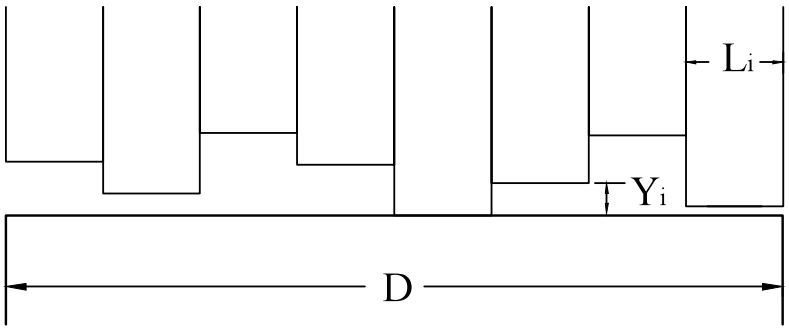

Figure 3.5: Initial positions of independent failure zones relative to the structure

As shown in Fig. 3.3, we assume the mean position of the contact face is zero, the individual position of each zone y_i is assumed to have a normal distribution. By adjusting the standard deviation, we control the roughness of the contact face. When the contact face profile is generated, the most upfront zone is just in contact with the structure at the beginning of the simulation. Therefore, as shown in Fig. 3.5, the initial position of each failure zone is

$$Y_i = y_i - y_{max} \tag{3.7}$$

As the indentation begins, when the deformation of one failure zone exceeds its

limit Δ_L, an ice cube of size L_i^3 fails. This failure zone will not be contacting the structure until it proceeds a distance of L_i. In this way, we are able to apply the mechanical model proposed by Matlock et al. and Karr et al (*Matlock et al.*, 1971; *Karr et al.*, 1993). As shown in Fig. 3.6, each failure zone is modeled as a series of ice teeth, with L_i as the distance between successive teeth. The failure of one ice cell is modeled as the breakage of one ice tooth. When the deformation of the ice tooth reaches the maximum value Δ_L, the ice tooth breaks.

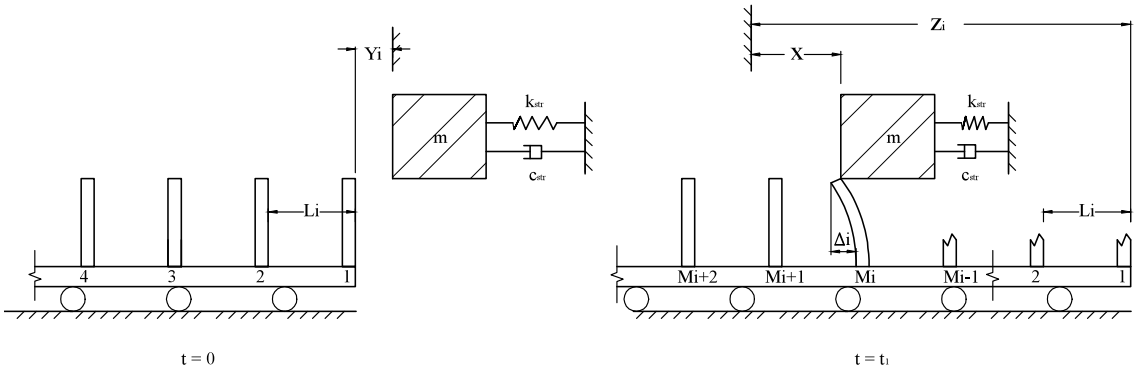

Figure 3.6: Application of the dynamic ice-structure interaction model by Matlock et al. and Karr et al. to model the ice failure within the i^{th} independent failure zone (*Matlock et al.*, 1971; *Karr et al.*, 1993). Left: the relative position of ice teeth and the structure at t=0. Right: the relative position of ice teeth and the structure at $t = t_1$

As shown in Fig. 3.6, at $t = 0$, the ice tooth within the i_{th} failure zone has an initial location Y_i. Then during the indentation process, at a certain time t_1, M_{i-1} ice teeth have been broken. The deformation of the M_i^{th} ice tooth can be calculated as

$$\Delta_i = z_i - x - L_i\,(M_i - 1) = Y_i + v_{ice}t - L_i\,(M_i - 1) - x \tag{3.8}$$

where z_i is the position of the first ice tooth at time t_1. The elastic stiffness of ice

teeth in the i^{th} failure zone can be calculated as

$$K_i = L_i^2 \sigma_L / \Delta_L \tag{3.9}$$

where σ_L is the pressure to fail a single ice cell. Then the ice force exerted on the i^{th} failure zone is

$$F_i = \begin{cases} K_i \left[y_i - y_{max} + v_{ice} t - L_i \left(M_i - 1 \right) - x \right] & 0 < \Delta \leq \Delta_L \\ 0 & \Delta \leq 0 \end{cases} \tag{3.10}$$

When Δ_i reaches its limit, the current ice tooth fails and $M_i = M_i + 1$. Then the total ice force at time t is the sum of all the local ice forces:

$$F = \sum_{i=1}^{N} F_i \tag{3.11}$$

3.3 Effect of changing various parameters on the resulting ice indentation pressure

In this new model, we introduce normal distribution to describe the shape of the ice-structure contact surface. Affected by this factor, the probability of each failure zone contacting the structure at any time incident is not uniform. Therefore, the total number of cells contacting the structure at any time does not have the simple form of Binomial distribution. For this reason, in order to study the peak ice force and indentation pressure, and the pressures dependence on various parameters, we apply the Monte Carlo method. For each simulation, an ice-structure contact surface is generated according to a normal distribution of y_i. Then a time-history of ice force is simulated, as shown in Fig. 3.7. From the ice force time history of each simulation, we collect the value of the peak ice force, average it over the total contact area and determine the maximum indentation pressure of a single simulation. We then average

the maximum indentation pressures of the simulations and study the relation between the resulted pressure and various parameters.

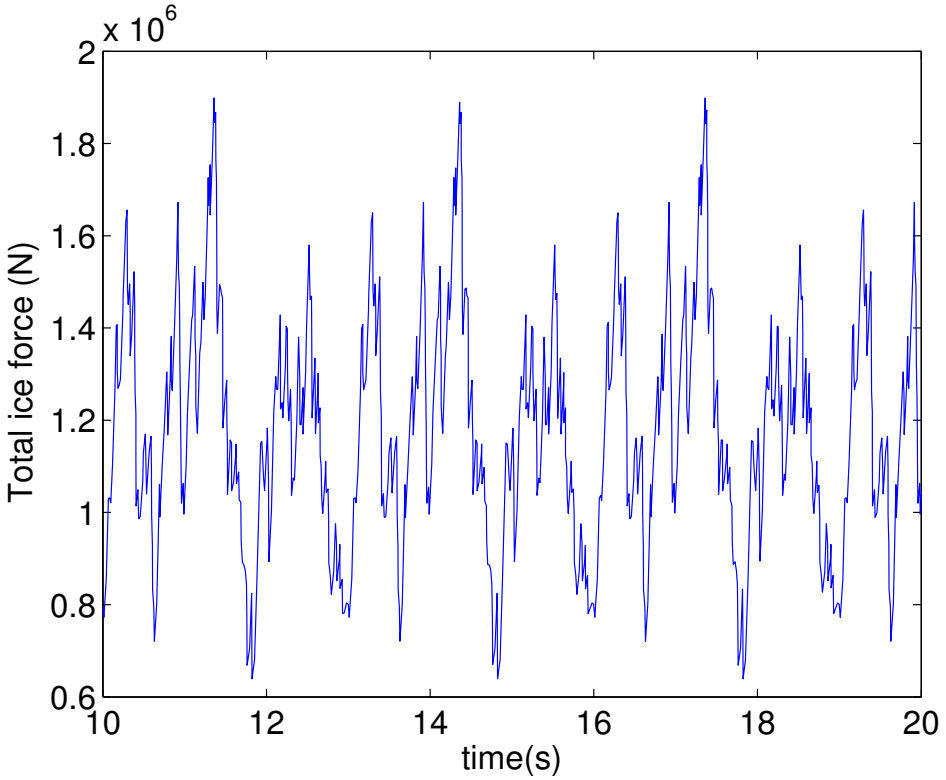

Figure 3.7: Example ice force time history simulated using the ice nonsimultaneous failure model

3.3.1 Pressure vs. area and zone size

When checking the indentation pressure dependence on contact area and zone size, we set the standard deviation of y_i equal to $0.09m$. The ice has a velocity of 0.05 m/s and the pressure to fail a single ice cell is set to be 15 MPa. And Δ_L is $0.02L_i$. For independent zone sizes L_i of 1 m and 0.5 m, peak force and indentation pressure are calculated for contact areas ranging from 0.25 to 500 m^2. The values at each zone size and area are calculated from 200 simulations. We plot the resulting indentation pressure as a function of contact area and compare the curves to the observed data provided by Sanderson (*Sanderson*, 1988) and the curve generated by

Ashbys theory (*Ashby et al.*, 1986), as shown in Fig. 3.8. The parameters used by Ashby are: independent zone size $L_i = 1\ m$, the pressure to fail a single ice cell was 15 MPa and Δ_L was 0.02 m.

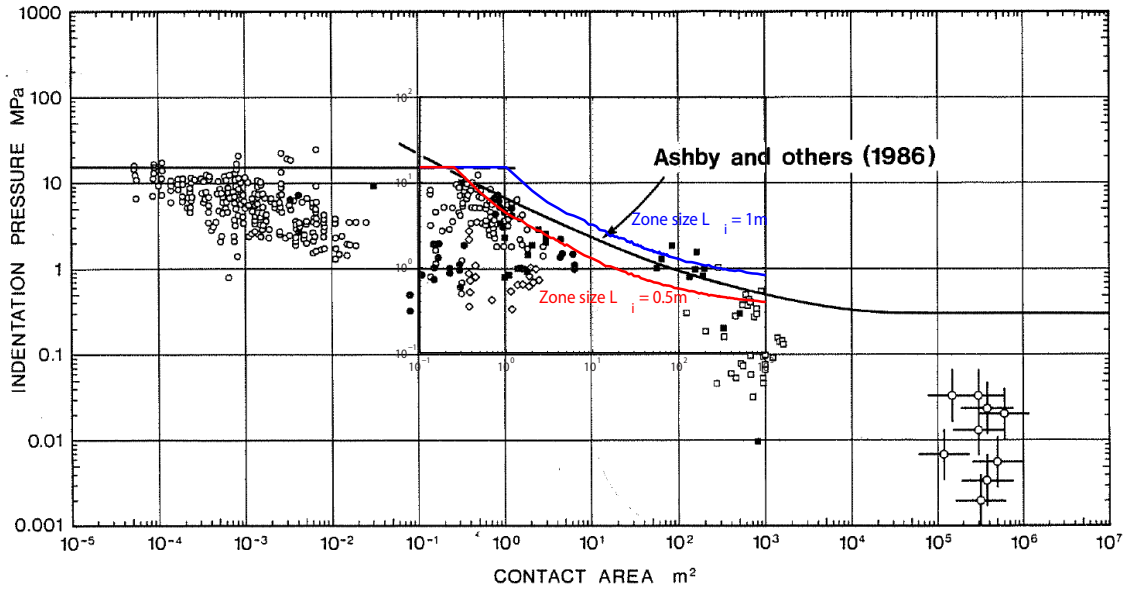

Figure 3.8: Comparison of simulated pressure-area curves for independent failure zone sizes of 1m and 0.5m to the curve generated by Ashbys theory (*Ashby et al.*, 1986) and field data provided by Sanderson (*Sanderson*, 1988).

It can be observed from the above figure that the pressure decreases as the area increases. One common representation of the pressure-area relation is in the form of power-law equation:

$$P = CA^d \tag{3.12}$$

When we apply the above equation to fit the pressure area curve, the resulting values of C and d are shown in Table 3.3.1.

It can be observed that the values of C and d also decrease as the area increases. This phenomenon may be qualitatively explained by the fact that the distribution of the number of cells contacting the structure is affected by both binomial distribution and normal distribution. When the ice-structure contact face profile is generated from

Table 3.1: Values of C and d when fitting whole and partial pressure-area curves

	Overall		Area=1-20 m^2		Area=20-60 m^2		Area=60-500 m^2	
	C	d	C	d	C	d	C	d
Zone Size =1	7.35	-0.395	12.3	-0.591	7.38	-0.398	3.83	-0.238
Zone Size =0.5	3.60	-0.385	4.58	-0.592	3.09	-0.391	1.39	-0.195

a normal distribution, the zones that will be contacting the structure simultaneously are those that have relative positions closer than Δ_L:

$$y_i - y_j \leq \Delta_L \tag{3.13}$$

When the total number of failure zones is large, the maximum possible number of simultaneously contacting zones happens when $\Delta_L/2 y_i \Delta_L/2$, as shown in Fig. 3.9. This number can be calculated from the cumulative probability density function $F(x)$ of a normal distribution:

$$n_{max} = N\left[F\left(\Delta_L/2\right) - F\left(-\Delta_L/2\right)\right] \tag{3.14}$$

And the indentation pressure at the peak force becomes:

$$P = \frac{F_{peak}}{A} = \frac{n_{max}\sigma_L L_i^2}{N L_i^2} = \sigma_L\left[F\left(\Delta_L/2\right) - F\left(-\Delta_L/2\right)\right] \tag{3.15}$$

This value does not change as the total contact area A changes. As the total number of independent failure zones N increases, this effect of normal distribution gets stronger and the pressure tends to stay constant as the area increases. In this way, the trend of decreasing order d with increasing area can be explained.

The results also show that the average maximum pressure differs greatly with different failure zone sizes. This can be explained by the binomial nature of the problem. If the zone sizes $(L_i)_1 = 2(L_i)_2$, in order to have the same number of failure

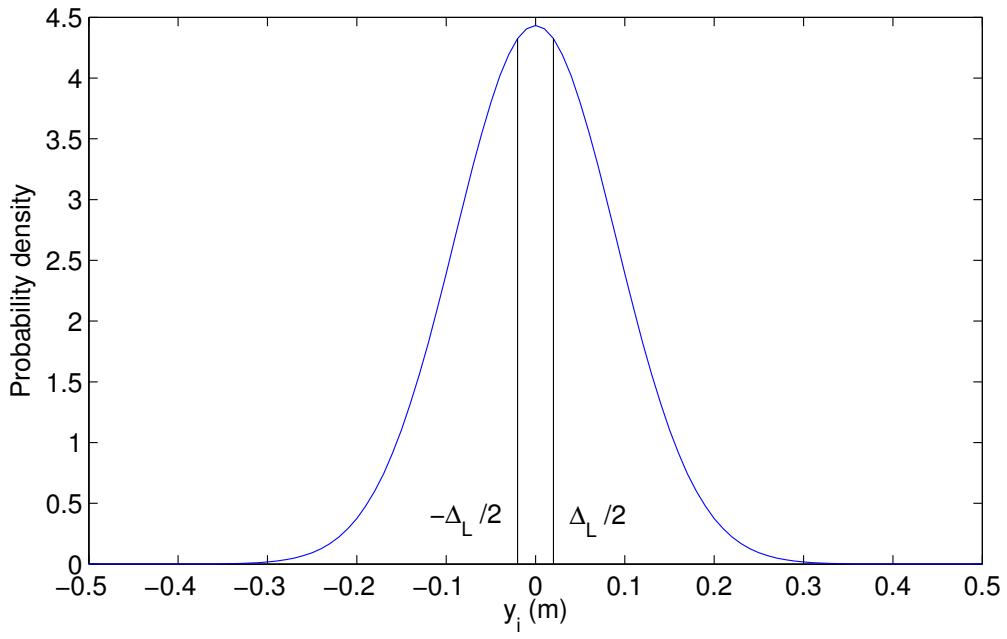

Figure 3.9: Maximum possible number of simultaneously contacting zones is the number of zones that have positions distributed between $\Delta_L/2 y_i \Delta_L/2$, when the total number of zones is large

zones, the contact areas should be $(A)_1 = 4(A)_2$. If we assume the total number of zones (n) simultaneously contacting the structure still has the binomial distribution, then the pressure for (A)1 = 4(A)2 of the case that zone sizes $(L_i)_1 = 2(L_i)_2$ should be the same:

$$P_1 = C_1 A_1^{d_1} = P_2 = C_2 A_2^{d2} \tag{3.16}$$

$$d_1 = d_2,\ C_1 = 4^{-d_1} C^2 \tag{3.17}$$

As shown in Table 3.3.1, the values of C and d approximately comply with this relation. In general application of this model, the size of fracture pieces of ice measured in a compressive indentation experiment can be used as an approximation for independent zone sizes (*Sanderson*, 1988; *Ashby et al.*, 1986).

3.3.2 Pressure vs. Δ_L

When checking the indentation pressure dependence on Δ_L, we set the ice velocity as 0.05 m/s, ice block thickness as 1 m and structure width as 3 m. The standard deviation of ice contact face position is 0.09 m and the failure stress of a single zone is 15 MPa. The failure zone size is set to be 0.5 m. The average of indentation pressure results of 200 simulations is recorded for each Δ_L. The result, as in Fig. 3.10 shows an approximately linear increasing trend of pressure over increasing Δ_L. This is as expected since larger Δ_L leads to possibly more failure zones contacting simultaneously.

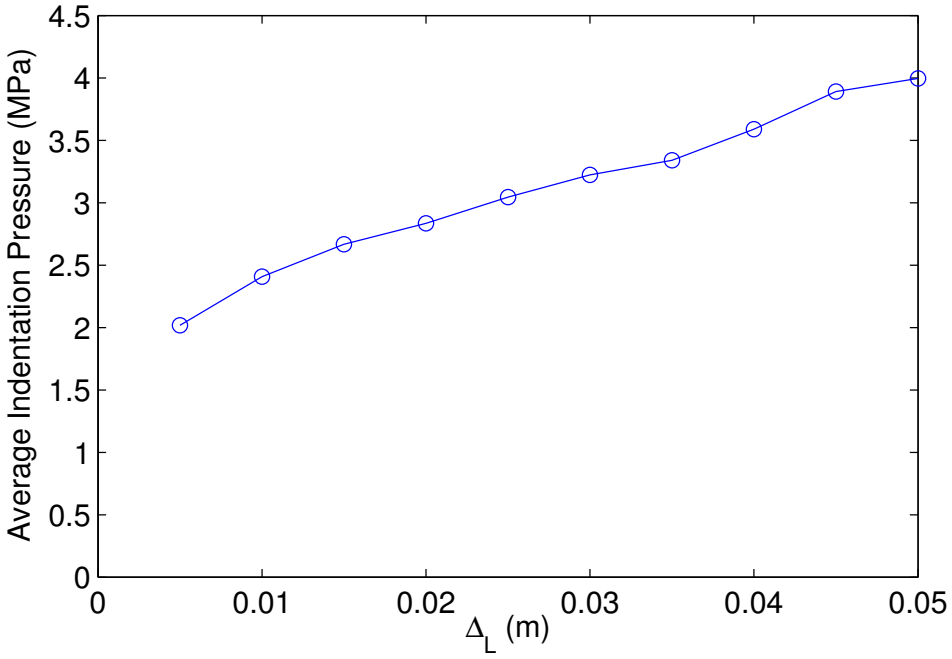

Figure 3.10: Simulation results show a trend of increasing maximum indentation pressure with increasing Δ_L

3.3.3 Pressure vs. ice contact face profile

The effect of the random ice contact face profile is also examined. We set the ice velocity at 0.05 m/s, ice thickness at 1 m and structure width at 3 m. The ice failure

stress is 15 MPa for a single zone and the failure zone size L_i is 0.5 m. The critical elastic deformation is $\Delta_L = 0.02L_i$. The average of indentation pressure results of 200 simulations is recorded for each standard deviation of ice contact face position. The result is shown in Fig. 3.11.

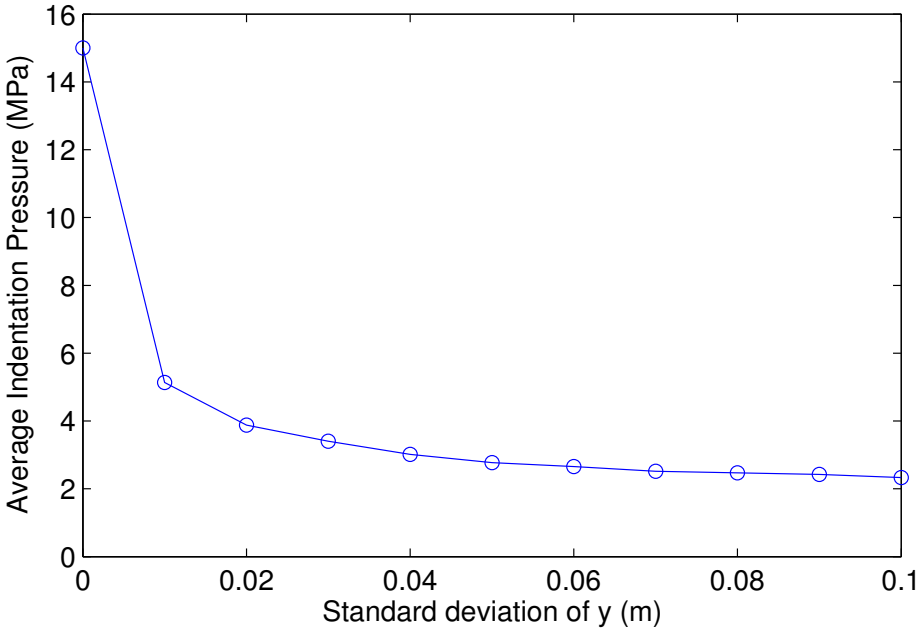

Figure 3.11: Simulation results show a trend of decreasing maximum indentation pressure with increasing irregularness of ice-structure contact face

From the above figure, it can be seen that when the standard deviation is 0, ice-loading pressure equals to 15 MPa. This is perfect contact and simultaneous failure. When the standard deviation increased, the relative positions between failure zones are less likely to be within Δ_L. Therefore, the peak ice force and indentation pressure decrease as well.

It should be noted that, in our model, the maximum ice force depends on the maximum possible number of simultaneously contacting zones, which only depends on the shape of the ice-structure contact face and the elastic properties of the equivalent ice teeth. The ice velocity does not affect the value of the peak ice force, as well as the pressure-area relation. However, the ice velocity does affect the dynamic feature

of the ice loading. This will be discussed in the following section.

3.4 Wind turbine simulation using FAST with ice module

FAST is the CAE tool maintained by the National Renewable Energy Laboratory (NREL) for simulating onshore and offshore wind turbine dynamics (*Jonkman and Buhl Jr.*, 2005). This model is implemented in the ice module in FAST for assessing dynamic wind turbine response to ice load (*Yu and Karr*, 2013).

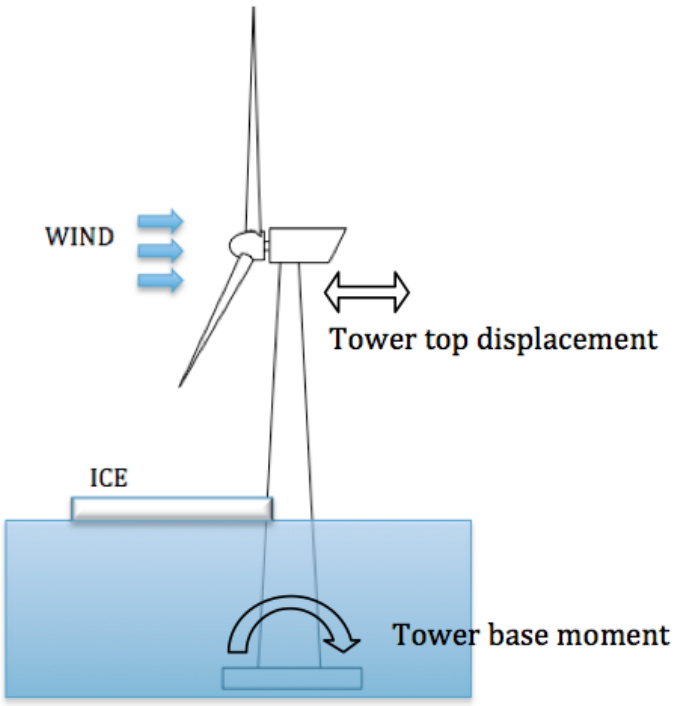

Figure 3.12: Example wind turbine in contact with wind and ice. Tower base moment and tower top displacement are selected to represent structural response

In this chapter, we present a simulation of an offshore system consisting of an NREL 5.0 MW Baseline Wind Turbine (*Jonkman et al.*, 2009) atop a fixed bottom monopile substructure. The turbine is operating under constant wind speed of 8 m/s and floating freshwater ice loading, as shown in Fig 3.12. The tower base moment and tower top displacement are selected to represent the tower response to wind and ice

force. The ice module reads the structure displacement at the ice-structure contact point from FAST main program as input and then calculates ice force at each time step as outputs to FAST.

We apply our ice model by using the following parameters: ice velocity is 0.2 m/s, ice thickness is 0.5 m, and structure width is 5 m. Therefore the ice structure contact face has one row of 10 independent failure zones. The standard deviation of ice contact face position is 0.09 m. The independent failure zone size is 0.5m. The ice failure stress of a single zone is 15 MPa. The critical elastic deformation $\Delta_L = 0.05m$. The ice contact face profile change over time in this simulation is shown in the Fig. 3.13.

The resulting time histories of total ice force, tower base moment and tower top displacement are shown in Fig. 3.14, 3.15 and 3.16 respectively.

The resulting time histories of the ice force, tower base moment and tower top displacement all have similar cycles. The periods, i.e. the time between sequential peak values of ice forces can be derived from the ice velocity and distance between sequential ice teeth if the structure response is not taken into consideration:

$$T = L_i/v \tag{3.18}$$

For this case, $T = 2.5s$. The periods read from the simulation results have approximately the same values. In this simulation, the structure response has the same frequency as the force. Therefore, this case is a typical forced-vibration problem. Simulations of other sample wind turbines with different mass, stiffness and damping properties are needed for further investigation of the dynamic effect of the ice model.

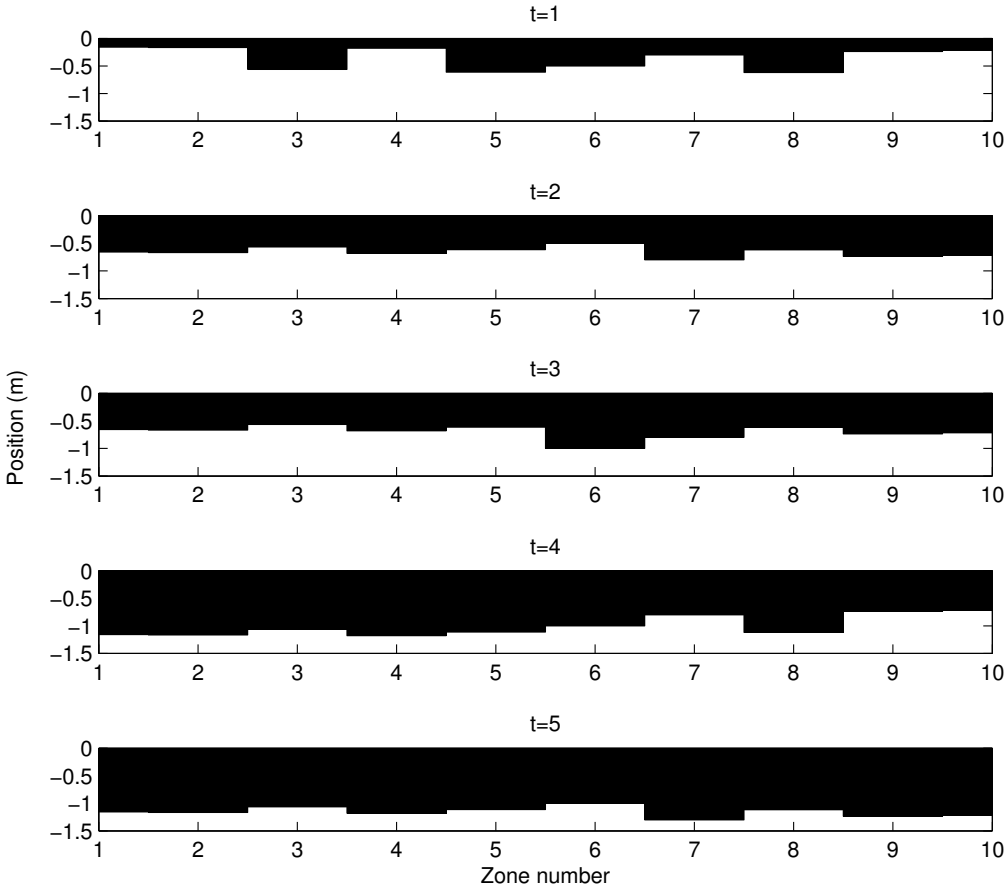

Figure 3.13: Ice-structure contact face profile change over time

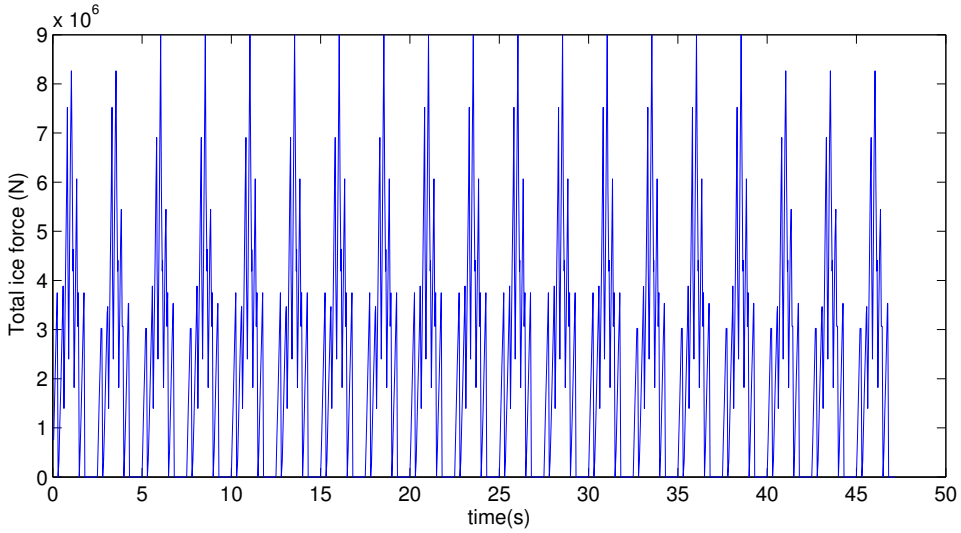

Figure 3.14: Time history of the cyclic ice force resulted from the non-simultaneous ice failure model

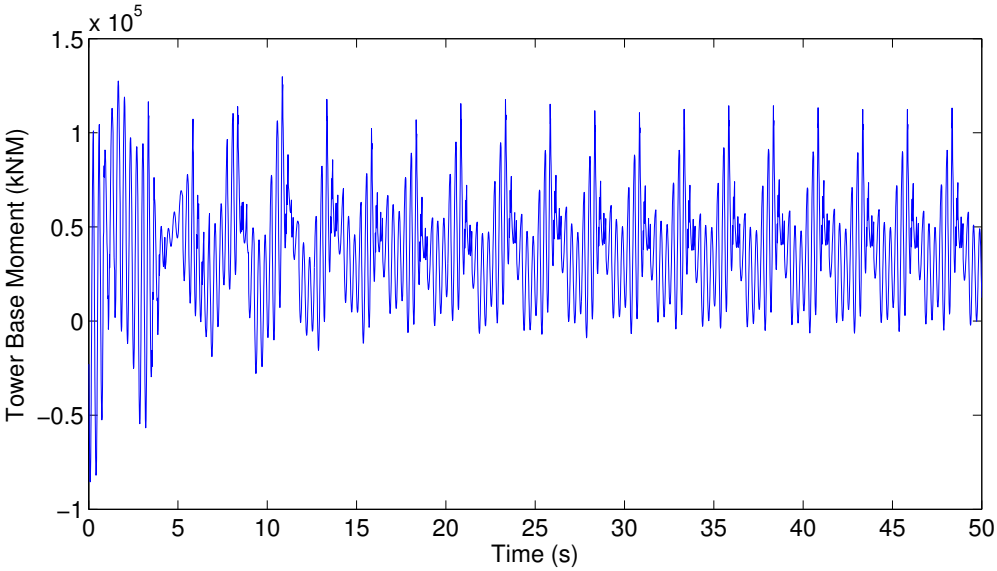

Figure 3.15: Time history of FAST simulated wind turbine tower base moment in the fore-aft direction, with similar cycle as the time history of ice force

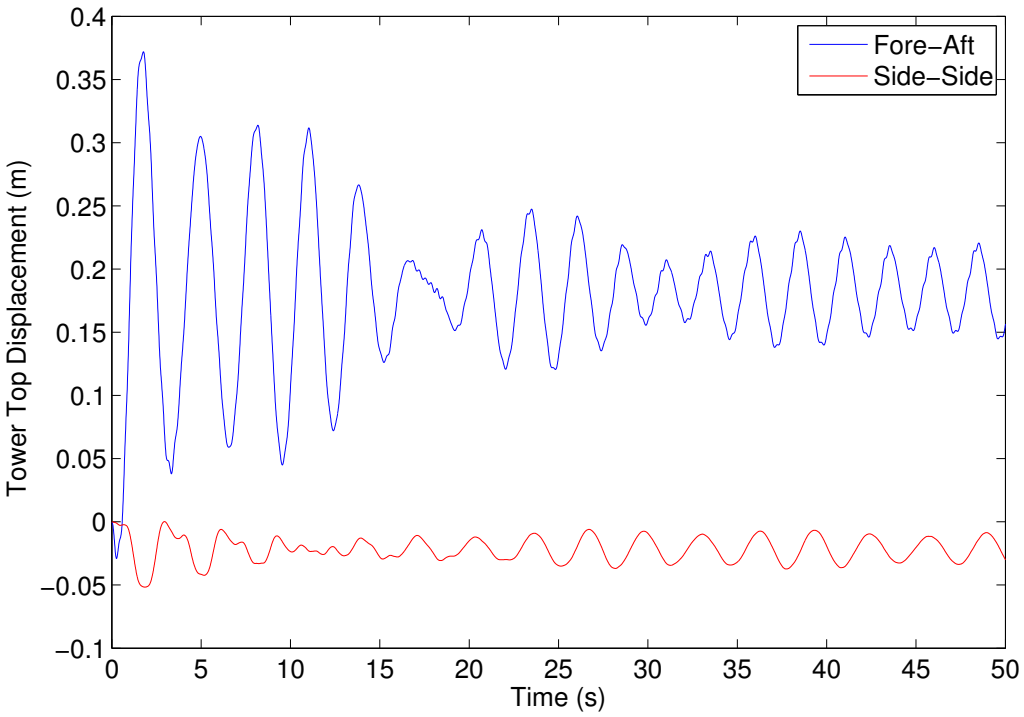

Figure 3.16: Time history of FAST simulated wind turbine tower top displacements, with similar cycle as the time history of ice force

3.5 Conclusion

In this chapter, a new analytical model to simulate time-dependent response of structures subjected to ice impact is proposed. This model further develops the independent failure zone theory by Ashby et al. and combines it with the dynamic ice- structure interaction model by Matlock and Karr. This model results in an ice force time history based on the shape of the ice-structure contact surface, the strength of each independent failure zone, ice drifting velocity and the structure displacement.

The new model introduces a normal distribution to describe and control the shape of the ice-structure contact surface. The result of this modification is that the peak ice force and maximum indentation pressure within one simulation are influenced by the nature of both binomial and normal distributions. This influence is reflected in the relations between maximum indentation pressure and parameters such as total contact area, failure zone size, deformation limit of a single zone and the shape of the contact surface. The model can also generate a pressure-area curve based on the input ice characteristics. The resulting shape of the pressure-area curve can be fitted by multiple power-law equations at different area ranges. According to the argument of Johnston et al., fitting the pressure-area data with multiple power-law equations instead of one may provide better description of the data (*Johnston et al.*, 1998).

This model generates time-dependent ice forces, which can be applied to dynamic ice-structure interaction analysis. In this chapter, a sample simulation is presented using FAST embedded with this ice failure model. The resulting ice force is cyclic and the frequency relates to the ice velocity and ice teeth spacing within a single zone. In the current model, the ice teeth spacing is set equal to the failure zone size L_i. Meanwhile a previous study shows that the ice teeth spacing is proportional to ice thickness and gives approximate ratio of these two values (*Sodhi and Morris*, 1986). This study provides useful suggestions on deciding the value of ice teeth spacing in general application of this ice failure model.

Some further refinements of the current model include consideration of random and spatially non-uniform strength of a single zone. Due to the factor of confinement, zones along the middle of the contact surface may have higher strength. Also, assigning random numbers to the ice strength may satisfy the observations that the pressure within a small zone can get as high as 40 MPa (*Johnston et al.*, 1998). Also, further investigations are needed for deciding parameters such as ice teeth spacing. Additional simulations of ice interacting with various structures are also needed to better understand the dynamic effect of the ice model.

CHAPTER IV

Ice Loading on Sloping Structures

4.1 Introduction

Many offshore structures in cold regions face great challenges due to the potential encounter with floating ice cover. For many cases, ice forces are very large compared to other environmental forces, thus usually govern the design of offshore structures. As a result, there is a need to design offshore structures to reduce ice forces to the largest extent. Considering the fact that ice tensile strength is much smaller comparing to its compressive strength, flexural failure is a preferred ice failure mode in an ice-structure interaction. To induce the flexural failure of ice and thus reduce ice forces, sloping structure especially conical structures attached to the offshore tower at water level are widely used, as shown in Fig. 4.1

Because of the reasons stated above, for offshore wind turbines to be deployed on the Great Lakes, there are plans proposed to attach ice cones to the wind turbine towers at the waterline level. Therefore, in our research of ice interaction with offshore wind turbines, it is necessary to include a model studying the ice bending failure mode. For the purpose of assessing ice loading on the ice cones as a input to simulate wind turbine responses, three parts should be considered. One is the magnitude of ice force when the bending failure happens. The second is the breaking length, which is defined as the distance between the zone of ice edge/structure contact and the first

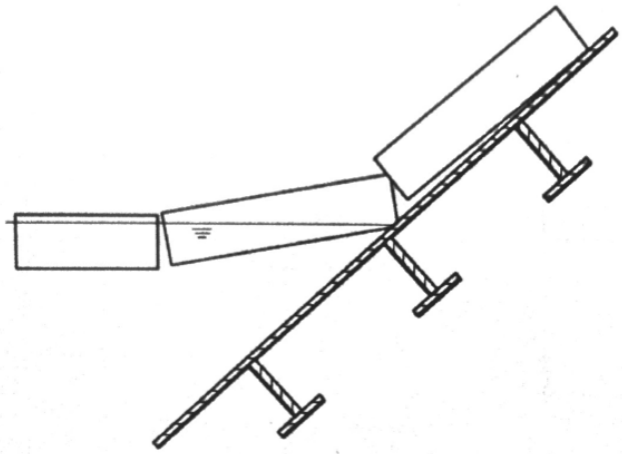

Figure 4.1: Ice bending on sloping structure (*Sanderson*, 1988)

circumferential crack (*Feng et al.*, 2003). The third is how the ice force changes over time after the bending failure.

Many previous research have developed ways to calculate ice forces on conical structures. One widely used theory is modeling ice as an elastic beam on an elastic foundation. Based on this theory, Croasdale incorporates adjustments for a three-dimensional model, taking into consideration of in-plane compression and the presence of ice rubble build-up (*Croasdale and Cammaert*, 1994). Aksnes et al. combined the elastic beam theory with friction theory and generated a dynamic model that considered the relative motions and velocities between ships and ice such that the vessel response influenced the interaction force between the hull and the ice (*Aksnes*, 2011). Dempsey et al. established a hydrodynamic ice-structure interaction problem and took into consideration the motion of the water (*Dempsey et al.*, 1999). Some research applied plastic limit theory in approximation of ice bending load. Ralston calculates ice loads by considering circumferential and side crack formations, elastic foundation reaction, ice deformation and ice bubble ride up on the conical structure (*Ralston*, 1980). Besides theoretical methods, numerical methods utilizing finite element methods were also applied to calculate ice breaking forces (*Kaldjian*, 1987; *Lu*

et al., 2012).

For the breaking length, many previous researches have established analytical or empirical estimations. A majority of researchers had adopted the ratio between the breaking length and the characteristic length of ice as a non-dimensional parameter to characterize the bending failure. The ratio ranging from around 0.6-0.8 by elastic beam theory (*Hetényi and Hetbenyi*, 1946), plate theory (*George*, 1986) or wedged beam theory (*Frederking*, 1980) to as low as 0.1-0.2 according to full-scale measurements (*Lau et al.*, 1999). Some other researchers also use the ratio of breaking length over ice thickness as a representative non-dimensional breaking length (*Feng et al.*, 2003; *Barker et al.*, 2005). From some previous model tests, the breaking length was found to increase with increasing thickness (*Finn et al.*, 1993) and is a strong function of ice morphology (*Poplin and Timco*, 2003). Some researchers speculated that the hydrodynamic effect of added mass may be responsible for bending failure distances lower than those predicted by elastic beam theory (*Sorensen*, 1978).

Most previous research on quasi-static ice forces did not generate explicit ice forces as a function of time. There are several model tests that provide general patterns of ice force time histories (*Barker et al.*, 2005; *Finn et al.*, 1993).

In this chapter, we established a simplified model to approximate the deformation field of the ice sheet when encountering a sloping structure, and thus calculate the ice force when bending failure happens. We also provide a quasi-static ice force time history that describe the change of ice force over time after the bending failure happens. The results of this model is compared to results from existing theories and model experiments. An example simulation using FAST with the new model is also presented.

4.2 A simplified method to approximate ice displacement field and ice breaking force

4.2.1 General theory

To propose a simplified method to calculate ice breaking loads and provide a simple approximation of the ice radial and circumferential cracks formation, we assume the floating ice cover as a rigid-plastic structure supported by an elastic foundation and apply the mode approximation method proposed by Augusti (*Augusti*, 1970).

Consider a rigid-perfectly plastic body Ω subjected to forces ξP_n which increase quasi-statically in proportion to a single parameter ξ, as shown in Fig. 4.2. The surface S of Ω is embedded on an elastic foundation, which provides distributed reactions of components $-c_i u_i$ per unit surface, where u_i are the components of the displacement and c_i are non-negative reaction coefficients.

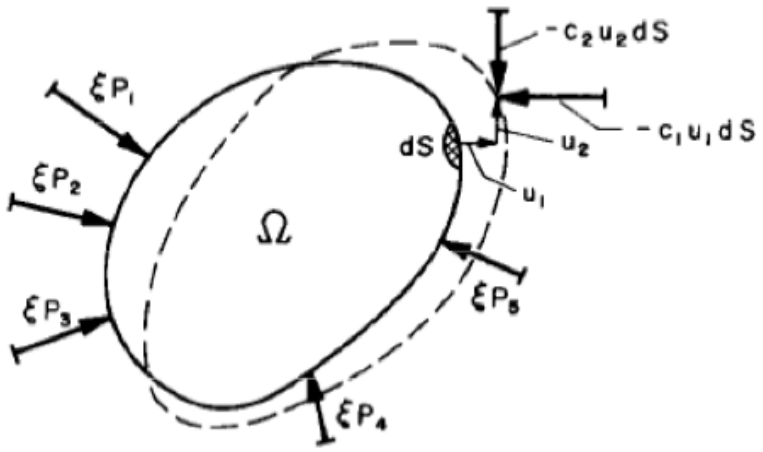

Figure 4.2: Diagram of a general body in elastic medium (*Augusti*, 1970)

According to Augusti's theory, consider a displacement field $u_i^*(\mathbf{x})$ such that the reactions $-c_i u_i^* dS$ are in equilibrium with loads ξP_n, but otherwise arbitrary. u_i^* is considered as an approximate solution for the displacements u_i. Let $\dot{q}_j^*$ be the strain

increments determined by u_i^* and Q_j' are the stresses associated with any non-zero $\dot{q}_j^*$ via plastic flow rule. Meanwhile, another set of stresses Q_j^* can be found in equilibrium with ξP_n and not violating the yield condition. Then the following inequality holds:

$$\int_S c_i(u_i - u_i^*)(\dot{u}_i - \dot{u}_i^*)dS \leq \int_\Omega (Q_j' - Q_j^*)\dot{q}_j^* d\Omega \tag{4.1}$$

Let

$$\Delta = \frac{1}{2}\int_S c_i(u_i - u_i^*)(u_i - u_i^*)dS \tag{4.2}$$

$$\Gamma = \int_\Omega (Q_j' - Q_j^*)\dot{q}_j^* d\Omega \tag{4.3}$$

Then the inequality Eqn. 4.1 becomes

$$\frac{\partial \Delta}{\partial \xi} \leq \Gamma \tag{4.4}$$

$$\Delta(\xi) \leq \Delta^+(\xi) = \int_0^\xi \Gamma d\xi \tag{4.5}$$

Let W^* be the elastic energy stored in the embedding medium

$$W^* = \frac{1}{2}\int_S c_i u_i^* u_i^* dS \tag{4.6}$$

Augusti assumed that the approximate displacement field u_i^* is more reliable the smaller is the ratio

$$\rho = \frac{\Delta^+}{W^*} \tag{4.7}$$

When applying the above theory to the ice sheet interaction with a sloping structure, we first make assumptions of the ice deformation field. According to the observation of many previous model experiments, when ice fails in bending, there are different modes depending on the relative dimension of structure diameter and ice

thickness. The ice sheet may fail in semi-infinite beam mode, plate failure mode and wedged beam failure mode. Each mode will result in different radial and circumferential crack formations (*Feng et al.*, 2003). As a result, we should also assume ice displacement field according to different relative dimensions of the structure and the ice sheet.

4.2.2 2D application - ice sheet interaction with flat sloping structures

When an ice sheet interacts with a flat sloping structure or with a conical structure with a diameter significantly exceeding ice thickness, the force between ice and structure can be considered an evenly distributed line load along the whole front boundary of the ice sheet. The the ice may fail in the mode of a semi-infinite beam.

As in the Augusti's method, we assume ice as an rigid plastic material. As the ice encounters the sloping structure, it is subject to a lifting force ξP_n. As argued by Augusti, for a semi-infinite beam, for any non-zero ξP_n, there exist a hinge line at a distance of L from the ice-structure contact edge. Therefore, we assume a displacement field as shown in Fig. 4.3.

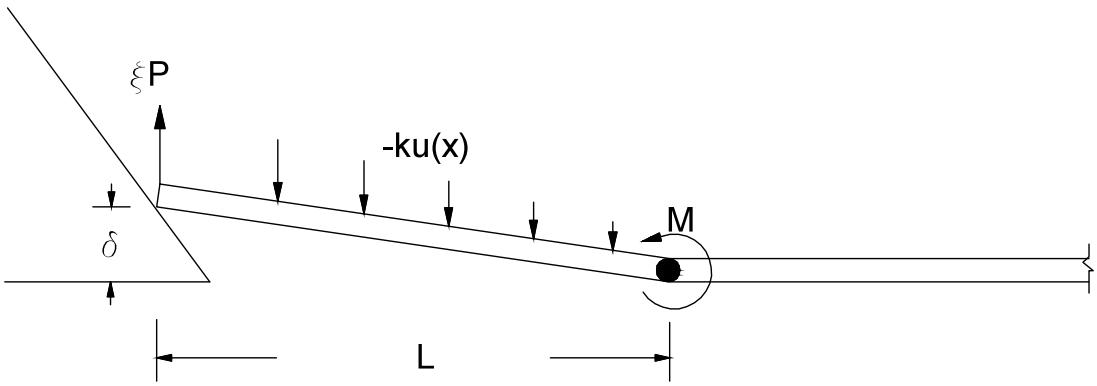

Figure 4.3: Approximate displacement field of sheet ice encountering a sloping strucutre

The front edge of the ice sheet is lifted by a distance of δ. The displacement $u^*(x)$ is in the form:

$$u^*(x) = \frac{x}{L}\delta \tag{4.8}$$

The hinge line happens where the bending moment reaches its maximum value, which means the shear force at the hinge line is zero. Here we assume δ is small so the ice sheet is not entirely lifted out of the water, i.e. $\delta \leq h\rho_i/\rho_w$, where ρ_i is the mass density of ice, ρ_w is the mass density of water and h is the ice thickness. Then the reaction force can be calculated from the ice plate weight and buoyancy: $-Ku = -\rho_w gBu$, where B is the ice sheet width. Also, the assumption that δ is small means that the horizontal ice-structure contact force does not contribute to the moment equilibrium. Then from the force and moment equilibrium of the ice sheet:

$$\xi P - \int_0^L K\frac{x}{L}\delta dx = 0 \tag{4.9}$$

$$M^* - \xi PL + \int_0^L K\frac{x}{L}\delta x dx = 0 \tag{4.10}$$

It can be determined that:

$$\xi P = \frac{1}{2}K\delta L \tag{4.11}$$

$$M^* = \frac{1}{6}K\delta L^2 \tag{4.12}$$

If we assume perfect plasticity, then from the flow rule,

$$M' = M_u \tag{4.13}$$

where $M_u = \sigma_f h^2 B/4$ is the total ultimate moment along the hinge line.

When $M^* = M'$, $\Gamma = 0$, hence the assumed displacement field is the accurate

solution. Then we have:

$$M_u = \frac{1}{6} K \delta L^2 \tag{4.14}$$

$$L = \sqrt{\frac{6M_u}{K\delta}} \tag{4.15}$$

$$\xi P = \frac{\sqrt{6}}{2} \sqrt{M_u k \delta} \tag{4.16}$$

It can be seen from the above equations that as δ increases, the applied force increases and L decreases, which means that the hinge line travels towards the contact edge between ice and structure as the ice is pushed along the slope.

Since ice has the characteristic that it is a ductile material at low strain rate and brittle material at high strain rate, it is unrealistic if the plastic deformation or δ increase to a significant level if the strain rate is large. A breaking mechanism should be assumed. In this chapter, we use both limit strain and limit strain rate as ice breaking criteria.

We assume that once the limit strain rate $\dot{\epsilon}_{lim}$ is reached, the behavior of ice is in the brittle region and ice fails in fracture if its strain exceeds the limit strain ϵ_{lim}. In order to approximate the strain and strain rate, as shown in Fig. 4.4, we assume the size of the hinge node is $h \times h$. Therefore the strain can be calculated as

$$\epsilon = \frac{2\Delta}{h} = \frac{\Delta}{h/2} = \frac{\theta}{2} = \frac{\delta}{2L} \tag{4.17}$$

Substitute L calculated from Eqn. 4.15, we have

$$\epsilon = \frac{\delta}{2\sqrt{\frac{6M_u}{K\delta}}} = \frac{\sqrt{6}}{12} \sqrt{\frac{K}{M_u}} \delta^{\frac{3}{2}} \tag{4.18}$$

$$\dot{\epsilon} = \frac{\sqrt{6}}{8} \sqrt{\frac{K\delta}{M_u}} \dot{\delta} = \frac{3}{4} \frac{\dot{\delta}}{L} \tag{4.19}$$

From geometry of the ice-structure contact, $\dot{\delta}$ can be related to the ice sheet

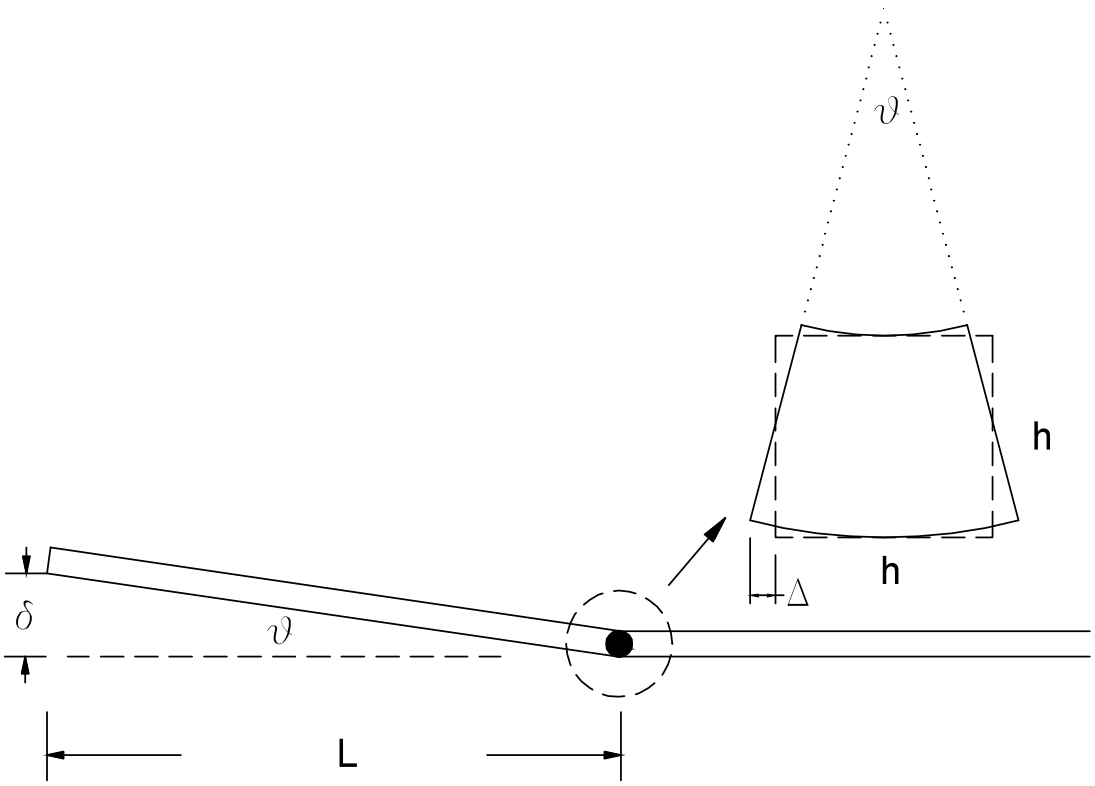

Figure 4.4: Geometry and strain definition at the hinge node

velocity v:

$$\dot{\delta} = v \tan \alpha \tag{4.20}$$

As a result,

$$\dot{\epsilon} = \frac{3}{4} \frac{v \tan \alpha}{L} \tag{4.21}$$

When the ice moves at a constant speed against the structure, as δ increases, the strain at the hinge line increases. The hinge line travels toward the contact edge so L decreases. Therefore the strain rate increases as well. When the $\dot{\epsilon}_{lim}$ is reached, the ice transitions to the brittle regime. If the limit strain ϵ_{lim} is also reached, the ice fails in fracture along the hinge line. From the limit strain rate, the ice breaking length, vertical displacement at the ice front edge and ice breaking force can be calculated

as:

$$L_{lim,1} = \frac{3v\tan\alpha}{4\dot{\epsilon}_{lim}} \tag{4.22}$$

$$\delta_{lim,1} = \frac{6M_u}{KL_{lim}^2} = \frac{32M_u\dot{\epsilon}_{lim}^2}{3Kv^2\tan^2\alpha} \tag{4.23}$$

$$\xi P_{lim,1} = \frac{3M_u}{L_{lim}} = \frac{4M_u\dot{\epsilon}_{lim}}{v\tan\alpha} \tag{4.24}$$

From the limit strain, the ice breaking length, vertical displacement at the ice front edge and ice breaking force can be calculated as:

$$L_{lim,2} = \sqrt[3]{\frac{3M_u}{K\epsilon_{lim}}} \tag{4.25}$$

$$\delta_{lim,2} = \sqrt[3]{\frac{24M_u\epsilon_{lim}^2}{K}} \tag{4.26}$$

$$\xi P_{lim,2} = \frac{3M_u}{L_{lim,2}} = \sqrt[3]{9M_u^2K\epsilon_{lim}} \tag{4.27}$$

When $L_{lim,1} < L_{lim,2}$, which means when limit strain rate is reached, the strain is already larger than the limit strain. Then the first set of criteria should be applied. Otherwise, we apply the second set of criteria.

4.2.3 3D application - ice sheet interaction with conical structures

When the cone angle gets steeper, the loading boundary is a narrow line of the order of the ice thickness. The ice sheet deforms in bending in both lateral directions (*Feng et al.*, 2003). To approximate this failure mode, we assume the contact between ice and the structure is at a single point. As shown in Fig. 4.5, the displacement field of ice sheet is approximated with three hinge lines.

As the geometry defined in Fig. 4.6, the displacement field $u^*(x, y)$ can be calculated as

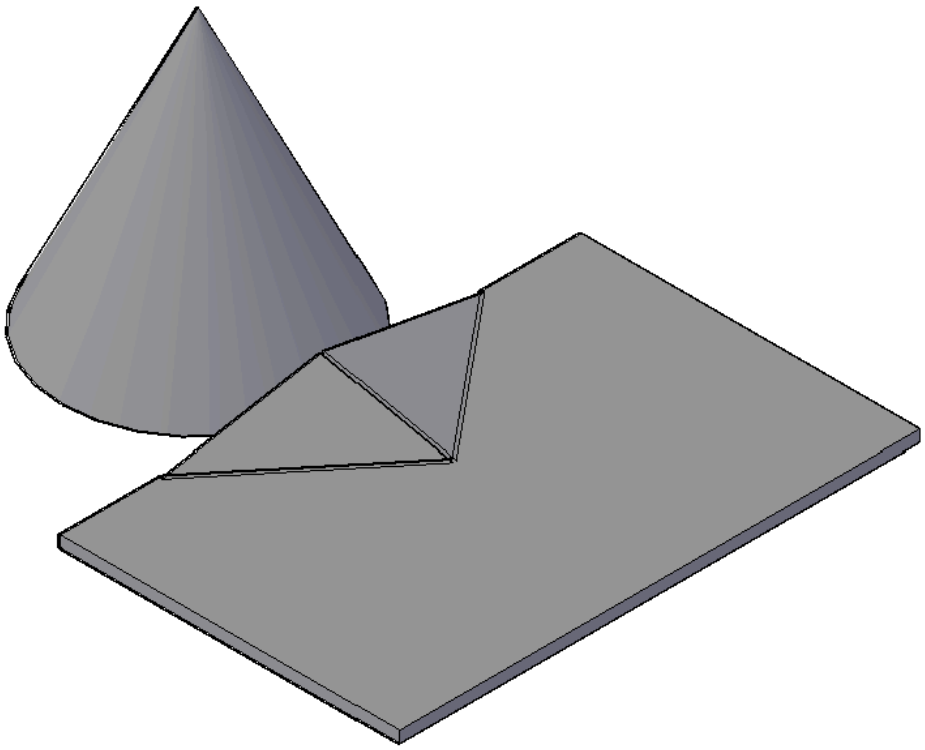

Figure 4.5: Approximation of ice deformation when contacting steeper cone

$$u^*(x,y) = \delta\left(1 - \frac{1}{L_y}y - \frac{1}{L_x}x\right) \tag{4.28}$$

Similar to the analysis in the previous section, we assume there is no shear force along the hinge lines. On plates ABD and BCD, the only vertical forces are the concentrated force at point B and the reaction forces from the foundation. From the equilibrium of vertical force on the plates ABD and BCD, the concentrated force at point B can be calculated

$$\xi P - \int_A K u^*(x,y) dA = 0 \tag{4.29}$$

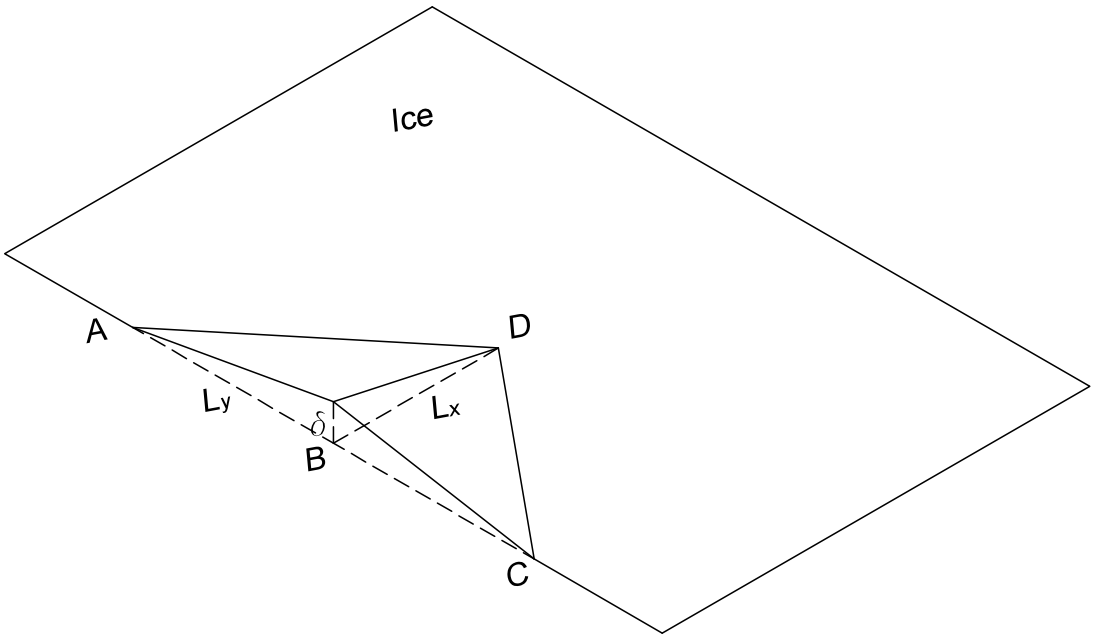

Figure 4.6: Geometry of the approximate ice displacement field

$$\xi P = 2 \int_0^{L_x} \int_0^{L_y(1-x/L_x)} K\delta \left(1 - \frac{1}{L_y}y - \frac{1}{L_x}x\right) dxdy \tag{4.30}$$

$$\xi P = \frac{1}{3} K\delta L_x L_y \tag{4.31}$$

where K is the reaction force from the change of buoyancy per displacement per unit area. In this case, $K = \rho_w g$.

Then as shown in Fig. 4.7, the equilibrium of moments of plate ABD can be calculated by summing up moments about point B.

$$\sum M_y = 0 \qquad \int_A Ku^* x dA - M^*_{AD} \frac{L_y}{\sqrt{L_x^2 + L_y^2}} = 0 \tag{4.32}$$

$$\sum M_x = 0 \qquad \int_A Ku^* y dA - M^*_{BD} - M^*_{AD} \frac{L_x}{\sqrt{L_x^2 + L_y^2}} = 0 \tag{4.33}$$

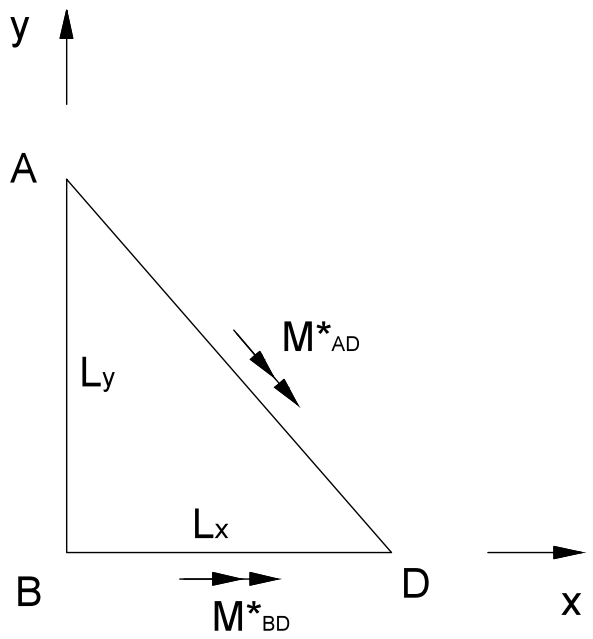

Figure 4.7: Equilibrium of moment

Moments along the hinge lines $\overline{AD}$ and $\overline{BD}$ generated from the equilibrium are as follows.

$$M^*_{AD} = \frac{1}{24} K\delta L_x^2 \sqrt{L_x^2 + L_y^2} \tag{4.34}$$

$$M^*_{BD} = \frac{1}{24} K\delta L_x \left(L_y^2 - L_x^2\right) \tag{4.35}$$

Meanwhile, moments along the hinge lines $\overline{AD}$ and $\overline{BD}$ generated from the plastic flow rule are

$$M'_{AD} = M_u \sqrt{L_x^2 + L_y^2} \tag{4.36}$$

$$M'_{BD} = M_u L_x \tag{4.37}$$

Similar to the analysis in the previous section, when $M^*_{AD} = M'_{AD}$, $M^*_{BD} = M'_{BD}$, $\Gamma = 0$ and the assumed $u^*(x, y)$ is the accurate solution. It can be solved by equating

Eqn. 4.34 to Eqn. 4.36, and Eqn. 4.35 to Eqn. 4.37 that

$$L_x = \sqrt{\frac{24M_u}{K\delta}} \tag{4.38}$$

$$L_y = \sqrt{\frac{48M_u}{K\delta}} \tag{4.39}$$

And the contact force ξP becomes

$$\xi P = \frac{1}{3}K\delta L_x L_y = 8\sqrt{2}M_u \tag{4.40}$$

It can be seen from the above equations that as δ increases, L_x and L_y decreases, the hinge lines $\overline{AD}$ and $\overline{BD}$ travel towards the contact point of ice and structure. However, the contact force remains constant.

Similar to the analysis of limit strain and strain rate in the previous section, in the 3D application, the strains along the hinge lines $\overline{AD}$ and $\overline{BD}$ are

$$\epsilon_{AD} = \frac{1}{2}\frac{\delta}{L_x L_y/\sqrt{L_x^2 + L_y^2}} \tag{4.41}$$

$$\epsilon_{BD} = \frac{\delta}{L_y} \tag{4.42}$$

Substitute the result of Eqn. 4.38 and Eqn. 4.39, then

$$\epsilon_{AD} = \frac{1}{8}\sqrt{\frac{K}{M_u}}\delta^{\frac{3}{2}} \tag{4.43}$$

$$\epsilon_{BD} = \frac{\sqrt{3}}{12}\sqrt{\frac{K}{M_u}}\delta^{\frac{3}{2}} \tag{4.44}$$

Thus the strain rates becomes

$$\dot{\epsilon}_{AD} = \frac{3}{16}\sqrt{\frac{K\delta}{M_u}}\dot{\delta} \tag{4.45}$$

$$\dot{\epsilon}_{BD} = \frac{3\sqrt{3}}{24}\sqrt{\frac{K\delta}{M_u}}\dot{\delta} \tag{4.46}$$

It can be seen from the above equations that ϵ_{AD} and $\dot{\epsilon}_{AD}$ are smaller than ϵ_{BD} and $\dot{\epsilon}_{BD}$. Therefore hinge line along BD breaks first, which means the radial cracks form first. This approximation matches the observation of experiment results of this failure mode (*Feng et al.*, 2003). The time difference between the breakage of the radial and circumferential hinge should be small, here we use the force when the circumferential crack breaks as the limiting breaking force.

If we also relate $\dot{\delta}$ with the horizontal velocity of ice sheet v

$$\dot{\delta} = v\tan\alpha \tag{4.47}$$

Then when $\dot{\epsilon}_{AD}$ reaches $\dot{\epsilon}_{lim}$,

$$L_{x,lim,1} = \frac{3\sqrt{6}}{8}\frac{\dot{\delta}}{\dot{\epsilon}_{lim}} \tag{4.48}$$

$$L_{y,lim,1} = \frac{3\sqrt{3}}{4}\frac{\dot{\delta}}{\dot{\epsilon}_{lim}} \tag{4.49}$$

$$\delta_{lim,1} = \left(\frac{16\dot{\epsilon}_{lim}}{3v\tan\alpha}\right)^2\frac{M_u}{K} \tag{4.50}$$

$$\xi P_{lim,1} = 8\sqrt{2}M_u \tag{4.51}$$

When ϵ_{AD} reaches ϵ_{lim},

$$L_{x,lim,2} = \sqrt{6}\sqrt[3]{\frac{M_u}{K\epsilon_{lim}}} \tag{4.52}$$

$$L_{y,lim,2} = 2\sqrt{3}\sqrt[3]{\frac{M_u}{K\epsilon_{lim}}} \tag{4.53}$$

$$\delta_{lim,2} = 4\sqrt[3]{\frac{\epsilon_{lim}^2 M_u}{K}} \tag{4.54}$$

$$\xi P_{lim,2} = 8\sqrt{2}M_u \tag{4.55}$$

The criterion that returns the smaller L_x should be applied.

4.3 Ice force time history

In order to provide ice load input for FAST, besides the limiting breaking force, we also need to generate ice force time history after the ice breaks. When an ice sheet drifts against a conical structure, we assume it fails in bending within a very short period of time after it contacts the structure. After it breaks, the broken ice piece is pushed by the rest of the ice sheet and rides up the cone. The previous analysis does not consider the weight of the ride-up ice on the cone. Here we ignore the shape of the cone and assume it as a flat sloping structure. There is a ride-up piece of ice that comes from previous bending failure, with the length of L_r. Then we assume the ice can ride up to a height of Z_r. The ice above that height is cleared due to the floe mechanism. As shown in the Fig. 4.8, the initial length of the ride-up ice L_r can be calculated as

$$L_r = (Z_r - \delta)/\sin\alpha \tag{4.56}$$

From the force equilibrium of the ride-up piece, the contact forces P_{N1} between the ride-up piece and the structure, F_1 between the ride-up piece and and the floating piece can be calculated.

$$P_{N1} = W_r \cos\alpha \tag{4.57}$$

$$F_1 = \mu P_{N1} + W_r \sin\alpha \tag{4.58}$$

where W_r is the weight of the ride-up piece, $W_r = \rho_i D h_r L_r$. D is the structure wideth, h_r is the ride-up piece thickness, μ is the friction coefficient between ice and the structure and α is the uprising angle of the structure.

Then the sum of forces acting at the contacting point between floating piece and

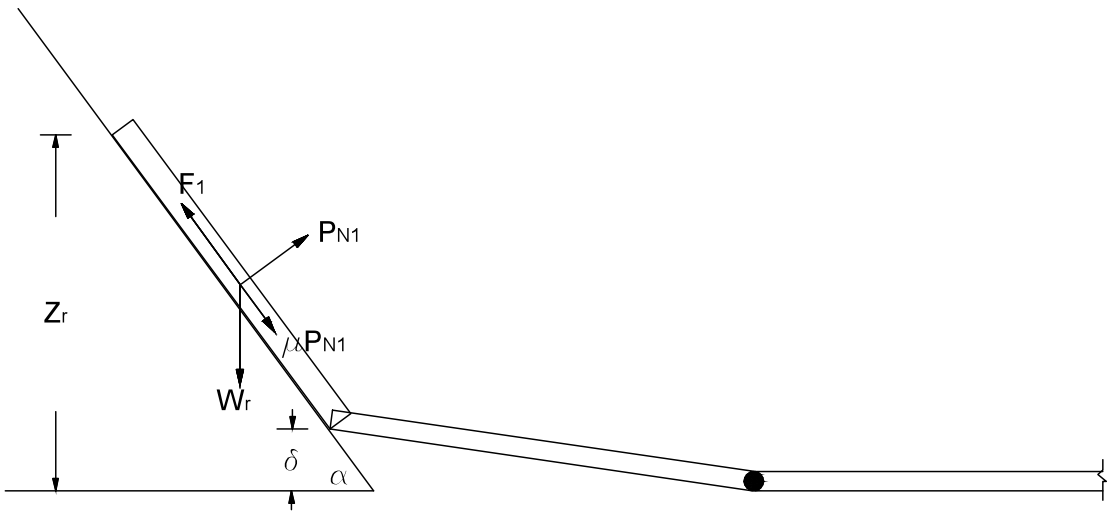

Figure 4.8: Force equilibrium of the ride-up piece

the structure provides the breaking force, as shown in the Fig. 4.9

$$P_{br} = P_{N2}\left(\cos\alpha - \mu\sin\alpha\right) + F_1\sin\alpha \tag{4.59}$$

$$P_{N2} = \frac{P_{br} + F_1\sin\alpha}{\cos\alpha - \mu\sin\alpha} \tag{4.60}$$

where from previous analysis

$$P_{br} = \frac{\sqrt{6}}{2}\sqrt{M_u k\delta} \qquad or \qquad P_{br} = 8\sqrt{2}M_u \tag{4.61}$$

Then the total ice force on the structure at breakage can be calculated

$$R_H = \left(P_{N1} + P_{N2}\right)\left(\sin\alpha + \mu\cos\alpha\right) \tag{4.62}$$

$$R_V = \left(P_{N1} + P_{N2}\right)\left(\cos\alpha - \mu\sin\alpha\right) \tag{4.63}$$

After the ice breaks, as shown in Fig 4.10, the broken piece is lifted up, out of the

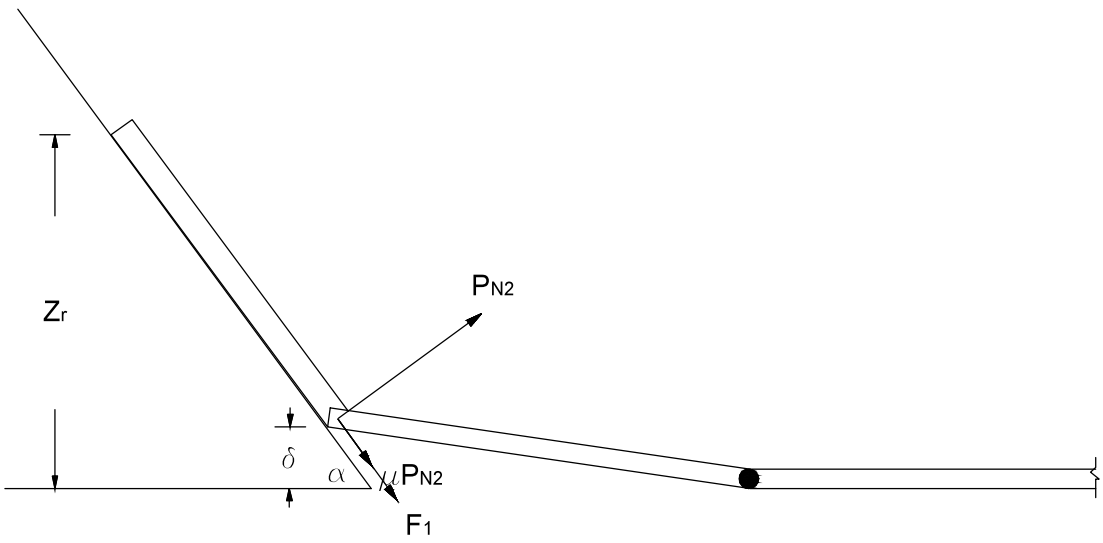

Figure 4.9: Forces acting at the contact point between floating ice piece and the structure

water and rides up the structure.

According to the geometry, the angle $\beta(t)$ can be solved from the following equation:

$$L\sin\beta\cot\alpha + L - vt = L\cos\beta \tag{4.64}$$

where v is the ice drifting speed and t is time. The weight of the ride-up piece changing over time is:

$$W_r = \rho_i g D h L_r = \rho_i g D h \left[Z_r - L\sin\beta(t)\right] / \sin\alpha \tag{4.65}$$

Similarly as before, from the the equilibrium of the ride-up piece,

$$P_{N1} = W_r \cos\alpha \tag{4.66}$$

$$F_1 = \mu P_{N1} + W_r \sin\alpha = W_r(\sin\alpha + \mu\cos\alpha) \tag{4.67}$$

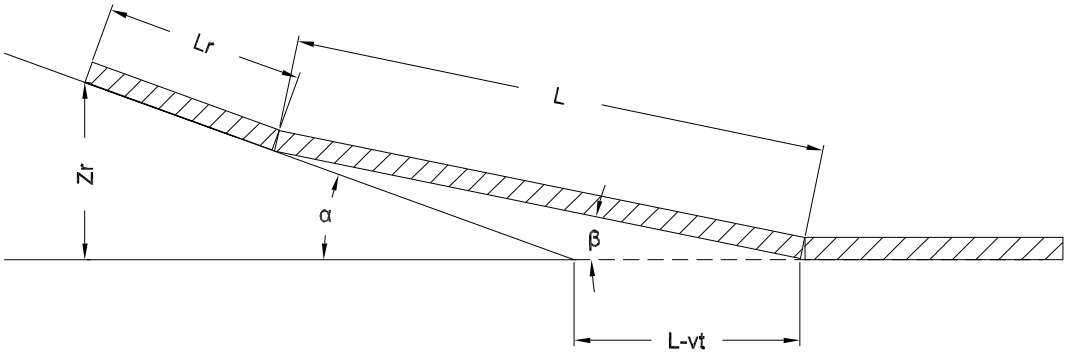

Figure 4.10: 2D model of ice sheet riding up the cone

From the equilibrium of the floating ice piece,

$$P_{N2} = \frac{\frac{1}{2}W_L L\cos\beta + W_r L g(\alpha,\beta) - F_B X_B}{L f(\alpha,\beta)} \tag{4.68}$$

where W_L is the weight of the floating ice piece, F_B is the buoyancy force, X_B is center of buoyancy and

$$f(\alpha,\beta) = \sin\beta(\sin\alpha + \mu\cos\alpha) + \cos\beta(\cos\alpha - \mu\sin\alpha) \tag{4.69}$$

$$g(\beta) = (\sin\alpha + \mu\cos\alpha)\sin(\alpha-\beta) \tag{4.70}$$

$$F_B = \begin{cases} \rho_w g D\left[L\left(\frac{\rho_i}{\rho_w}h - L\tan\beta\right) + \frac{1}{2}L^2\tan\beta\right] & \text{if } \beta < \frac{\rho_i h}{\rho_w L}, \\ \rho_w g D\left[\frac{1}{2\tan\beta}\left(\frac{\rho_i}{\rho_w}h\right)^2\right] & \text{if } \beta \geq \frac{\rho_i h}{\rho_w L}. \end{cases} \tag{4.71}$$

$$X_B = \begin{cases} \frac{L}{3}\left(\frac{3h\rho_i/\rho_w - L\tan\beta}{2h\rho_i/\rho_w - L\tan\beta}\right) & \text{if } \beta < \frac{\rho_i h}{\rho_w L}, \\ \frac{1}{3}\frac{h\rho_i/\rho_w}{\sin\beta} & \text{if } \beta \geq \frac{\rho_i h}{\rho_w L}. \end{cases} \tag{4.72}$$

The total ice forces on the structure are also

$$R_H = (P_{N1} + P_{N2})(\sin\alpha + \mu\cos\alpha) \tag{4.73}$$

$$R_V = (P_{N1} + P_{N2})(\cos\alpha - \mu\sin\alpha) \tag{4.74}$$

As an example, we consider an ice sheet with thickness of 0.65m, moving at a velocity of 0.2 m/s, interacting with a conical structure with waterline diameter of 8m and uprising angle of 55°. We set the maximum ride-up height of the ice at 5m. The friction coefficient of ice on the structure is assumed to be 0.1. The limit strain rate is set at $10^{-2}s^{-1}$ and the limit strain is 1.5%. The ultimate moment per unit length is

$$M_u = \frac{\sigma_f h^2}{4} \tag{4.75}$$

where σ_f is the tensile strength of ice. The resulted time histories of horizontal and vertical ice forces are shown in Fig. 4.11 and Fig. 4.12 respectively.

The resulted time histories show similar patterns to the ice force time histories observed from model tests (shown in Fig. 4.13).

4.4 Comparison with results from other theories

4.4.1 Comparison with the upper bound theorem of plasticity

A direct comparison can be made between the current model and the plasticity upper bound theorem. According to the upper bound theorem, if a compatible mechanism of plastic deformation is assumed which satisfied the conditions on the displacement boundaries, then the load determined by equating the rate of work of the external forces to the rate of internal energy dissipation will be either higher or equal to the collapse load.

Consider the 2D beam model with the front edge lifted by δ and has a plastic

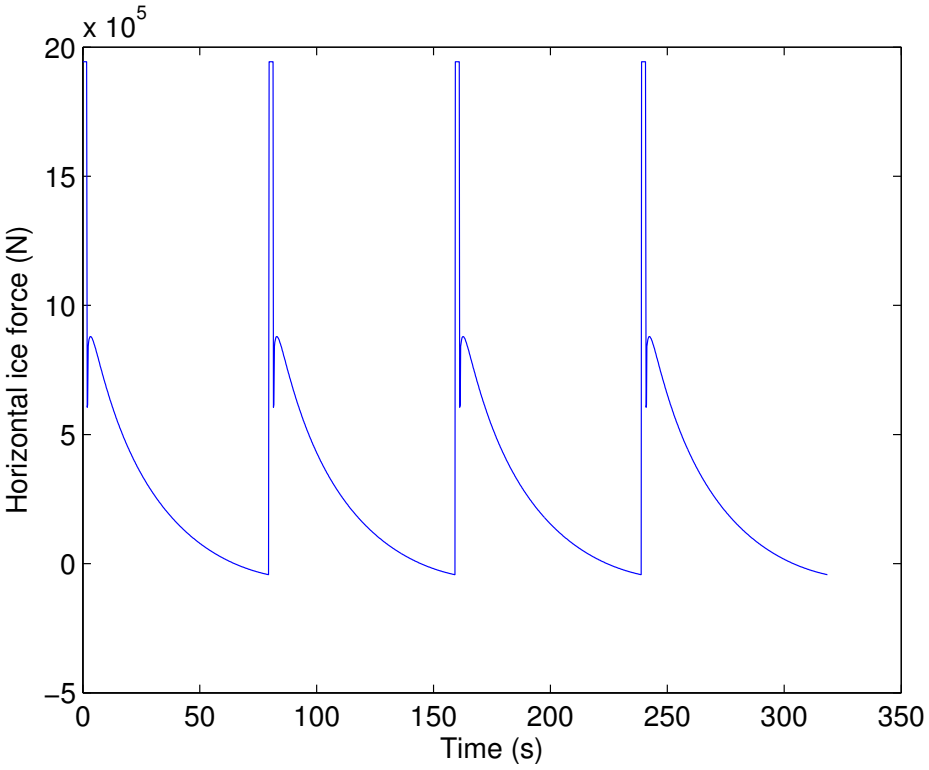

Figure 4.11: Horizontal ice force time history

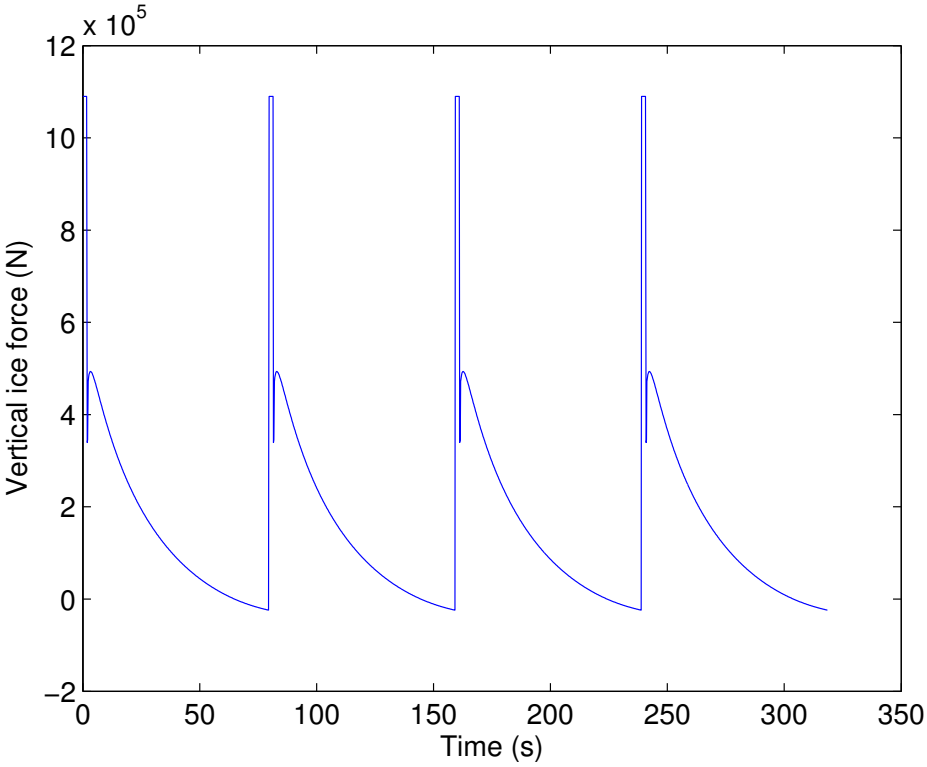

Figure 4.12: Vertical force time history

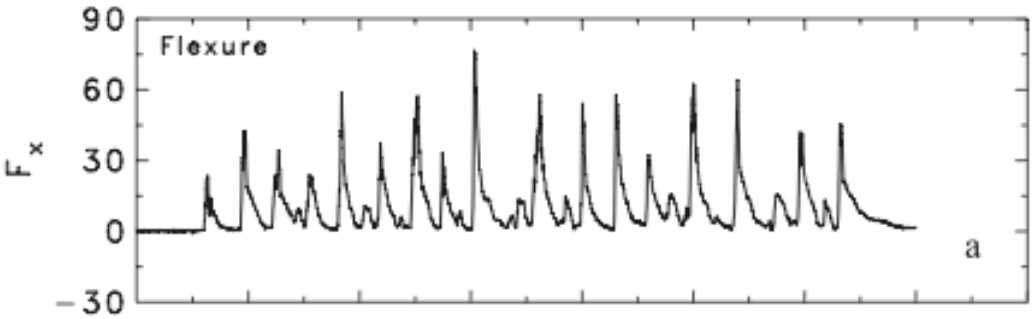

Figure 4.13: Ice force time history from model test (*Barker et al.*, 2005)

hinge at a distance of L away from the front edge. Using the upper bound theorem, the rate of external work is equated to the rate of internal energy dissipation:

$$\Delta \dot{W}_e = \Delta \dot{W}_i \tag{4.76}$$

From the assumed deformation field, the work of external forces can be calculated.

$$\Delta W_e = P\delta + \int_0^L -\frac{1}{2} K u(x)^2 dx \tag{4.77}$$

$$u(x) = \frac{\delta}{L} x \tag{4.78}$$

$$\Delta W_e = P\delta - \frac{1}{6} K \delta^2 L \tag{4.79}$$

$$\Delta \dot{W}_e = P\dot{\delta} - \frac{1}{3} K \delta L \dot{\delta} \tag{4.80}$$

The rotation angle at the hinge line can be generated from the geometry. Then the work of internal forces can be calculated.

$$\theta = \frac{\delta}{L} \tag{4.81}$$

$$\Delta W_i = M_u \theta = M_u \frac{\delta}{L} \tag{4.82}$$

$$\Delta \dot{W}_i = M_u \dot{\theta} = M_u \frac{\dot{\delta}}{L} \tag{4.83}$$

Then the Eqn. 4.76 becomes

$$P\dot{\delta} - \frac{1}{3} K \delta L \dot{\delta} = M_u \frac{\dot{\delta}}{L} \tag{4.84}$$

$$P = \frac{1}{3} K \delta L + \frac{M_u}{L} \tag{4.85}$$

Then we obtain the minimum load by determining the corresponding plastic hinge

location:

$$\frac{\partial P}{\partial L} = 0 \tag{4.86}$$

$$\frac{1}{3}K\delta - \frac{M_u}{L^2} = 0 \tag{4.87}$$

$$L = \sqrt{\frac{3M_u}{K\delta}} \tag{4.88}$$

$$P = \frac{2\sqrt{3}}{3}\sqrt{M_u k\delta} \tag{4.89}$$

As we compare the results of our 2D model and the results from upper bound theorem:

$$\frac{L_{2D}}{L_{upper}} = \frac{\sqrt{2}}{1} \tag{4.90}$$

$$\frac{P_{2D}}{P_{upper}} = \frac{2\sqrt{2}}{3} \tag{4.91}$$

It can observed that our model returns a larger breaking length and a slightly larger breaking force.

4.4.2 Comparison with plastic limit theory results

Ralston (*Ralston*, 1980) applied upper bound theory of plastic limit analysis to provide an estimate of the forces imposed on the cone. He proposed an assumed velocity field that described the motion of ice that occurred in the failure process. Then the rate of work done the external forces was equated to the rate of energy dissipation in the ice as a result of the assumed motion. Factors include the formation of plastic hinges to represent the circumferential and side cracks, the work done against the foundation reaction, the continuous deformation of ice within the deforming region and frictional dissipation at the cone/ice interface.

The resulting horizontal ice force can be calculated as

$$R_H = \left[A_1\sigma_f h^2 + A_2\rho_i g h D^2 + A_3\rho_i g h_R\left(D^2 - D_T^2\right)\right] A_4 \tag{4.92}$$

where

$$A_1 = \frac{1}{3}\left[\frac{\lambda}{\lambda-1} + \frac{1-\lambda+\lambda ln\lambda}{\lambda-1} + 2.422\frac{\lambda ln\lambda}{\lambda-1}\right] \tag{4.93}$$

$$A_2 = \left(\lambda^2+\lambda-2\right)/12 \tag{4.94}$$

$$A_3 = \frac{1}{4}\left[\frac{1}{\cos\alpha} + \frac{\mu E\left(\sin\alpha\right)}{\sin\alpha} - \mu\frac{f(\alpha,\mu)g(\alpha,\mu)}{\tan\alpha}\right] \tag{4.95}$$

$$A_4 = \frac{\tan\alpha}{1-\mu g(\alpha,\mu)} \tag{4.96}$$

$$g(\alpha,\mu) = \left(\frac{1}{2} + \frac{\alpha}{\sin\alpha}\right) / \left(\frac{\pi}{4}\sin\alpha + \frac{\mu\alpha\cos\alpha}{\sin\alpha}\right) \tag{4.97}$$

$$f(\alpha,\mu) = \sin\alpha + \mu\cos\alpha F(\sin\alpha) \tag{4.98}$$

$$F(\sin\alpha) = \int_0^{\frac{\pi}{2}} \frac{1}{\sqrt{1-\sin^2\alpha\sin^2\theta}}d\theta \approx \frac{\pi}{2} + \frac{\pi}{8}\frac{\sin^2\alpha}{1-\sin^2\alpha} - \frac{\pi}{16}\frac{\sin^4\alpha}{1-\sin^4\alpha} \tag{4.99}$$

$$E(\sin\alpha) = \int_0^{\frac{\pi}{2}} \sqrt{1-\sin^2\alpha\sin^2\theta}d\theta = \frac{\pi}{2}\sum_{n=0}^{\infty}\left[\frac{(2n)!}{2^{2n}(n!)^2}\right]^2\frac{\sin\alpha^{2n}}{1-2n} \tag{4.100}$$

Here D is the structure width/diameter at waterline, D_T is the top diameter of the cone, h is the ice thickness, h_R is the thickness of the ride-up ice, ρ_i is the mass density of ice, σ_f is the flexural strength of ice, μ is the friction coefficient between ice and cone, α is the uprising angle of the cone, $\lambda = A/R$, A is the circumferential crack diameter and $R = D/2$ is the cone waterline radius.

The vertical ice force becomes:

$$R_V = B_1 R_H + B_2\rho_i g h_R\left(D^2 - D_T^2\right) \tag{4.101}$$

where

$$B_1 = \frac{h(\alpha,\mu)}{\frac{1}{4}\sin\alpha + \frac{\mu\alpha}{\tan\alpha}} \tag{4.102}$$

$$B_1 = \frac{1}{4}\left[\frac{\pi}{2}\cos\alpha - \mu\alpha - \frac{f(\alpha,\mu)h(\alpha,\mu)}{\frac{\pi}{4}\sin\alpha + \frac{\mu\alpha}{\tan\alpha}}\right] \tag{4.103}$$

$$h(\alpha,\mu)=\cos\alpha-\frac{\mu}{\sin\alpha}\left[E(\sin\alpha)-\cos^2\alpha F(\sin\alpha)\right] \tag{4.104}$$

According to the definition of breaking length, the radius of the circumferential crack $A/2$ can be used as the breaking length l_b. Ralston uses $\lambda = 2l_b/R$ as a non-dimensional representative breaking length (*Ralston*, 1980). The parameter λ can be calculated using upper bound plastic limit analysis to minimize the horizontal ice force. It is the solution of the following equation:

$$\lambda - ln\lambda + 0.0922\frac{\rho_i g h D^2}{\sigma_f h^2}(2\lambda+1)(\lambda-1)^2 = 1.369 \tag{4.105}$$

A comparison between results of Ralston's method and the method presented in this chapter is conducted. When we have an ice sheet with thickness of 0.65m, moving at a velocity of 0.2 m/s, interacting with a conical structure with waterline diameter of 8m and top diameter of 5m. We set the maximum ride-up height of the ice is to the top of the cone. The friction coefficient of ice on structure is assumed to be 0.1. Ice tensile strength is 0.7 MPa.

The first set of comparisons is conducted with respect to different cone angles. The results of ice breaking force and breaking length are shown in Fig. 4.14 and Fig. 4.15.

It can be observed from the Fig. 4.14 that the vertical forces of both methods match very well. Meanwhile, the horizontal force resulting from the current method is larger than the Ralston's estimation but shows similar increasing trend as the cone angle increases. For the breaking length, from Fig. 4.15, it can be seen that the current result returns a much larger breaking length than Ralston's. According to Eqn. 4.48 and Eqn. 4.52, the breaking length limited by strain rate increases as cone angle increases while the breaking length limited by strain is independent of cone angle. As a result, the applied criterion of breaking failure changes from limit strain rate to limit strain as the cone angle increases.

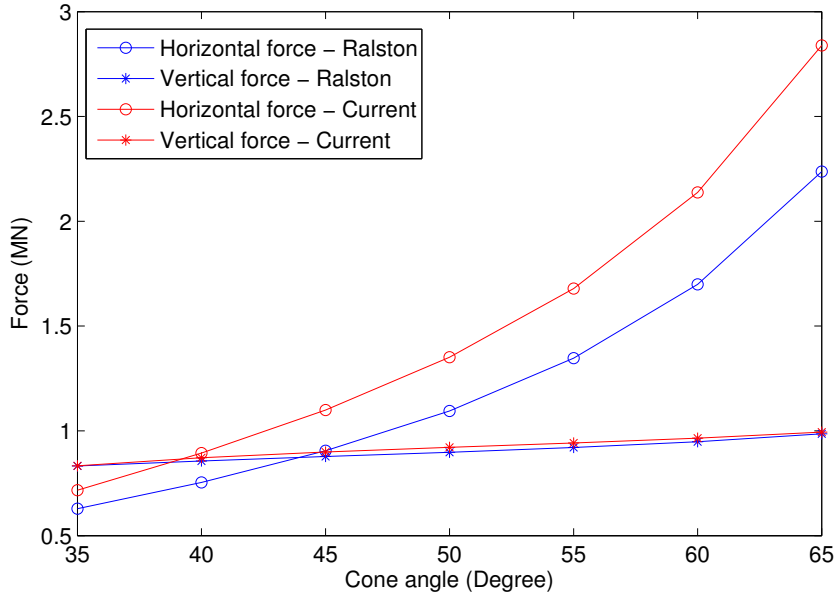

Figure 4.14: Comparison of ice breaking forces resulting from the current model and Ralston's method, with respect to different cone angles

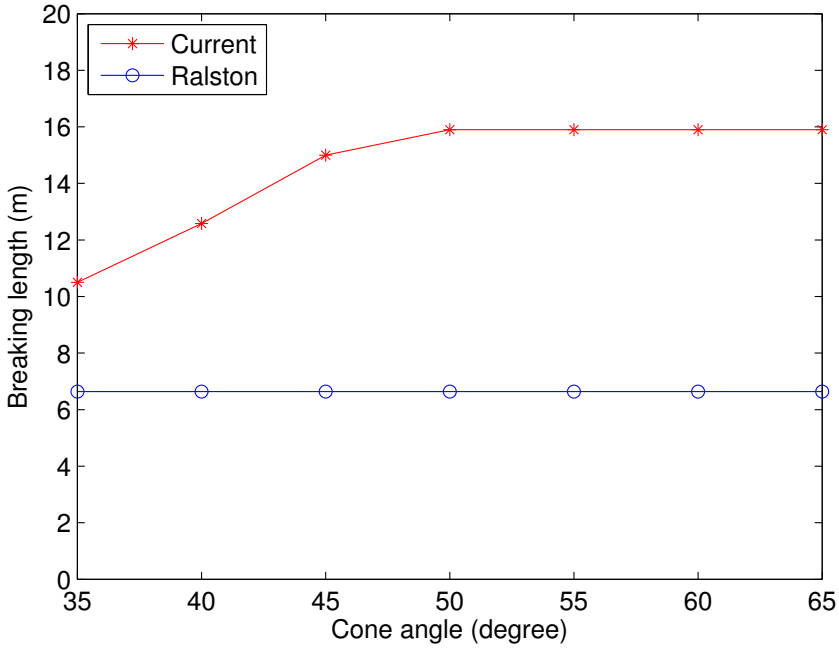

Figure 4.15: Comparison of breaking lengths resulting from the current model and Ralston's method, with respect to different cone angles

The second set of comparisons is conducted with respect to different ice thickness. The results of ice breaking force and breaking length are shown in Fig. 4.16 and Fig. 4.17. The non-dimensional ice breaking length L/h are also compared in Fig. 4.18

Also in this case, the vertical forces of both methods match very well. The current model returns a larger horizontal force than Ralston's, but the horizontal force shows similar increasing trend as the ice thickness increases. As shown in Fig. 4.17, the breaking length calculated by Ralston does not change significantly as ice thickness changes. For results of the current model, the breaking length limited by strain increases as ice thickness increases, while the breaking length limited by strain rate is constant. As a result, the applied criterion of breaking failure changes from limit strain to limit strain rate as the cone angle increases. The non-dimensional ice breaking length, as shown in Fig. 4.18, results of both methods show a decreasing trend.

4.5 Simulation of wind turbine response using FAST

In this section, one example simulation is presented here which involves the following: user input ice sheet thickness of 0.65m,ice velocity of 0.2 m/s, structure waterline diameter of 8m and uprising angle of 55. The maximum ride-up height of the ice is 3m. The friction coefficient of ice on structure is 0.1. The tensile strength of ice is 0.7 MPa. The simulated tower base moment and tower top displacement are shown in Fig. 4.19 and 4.20.

It can be seen from Fig. 4.19 and 4.20 that the tower base moment mainly follows the pattern of ice force time history and there is limited disturbance to the wind turbine motion.The maximum tower base moment is of the order of 10^4 kNm. And the maximum ice force is about 2 MN. This is corresponding to a equivalent pressure around 0.5 MPa, which is much smaller than the crushing strength of ice. The conical structure does significantly reduce ice loading on offshore wind turbines in this example.

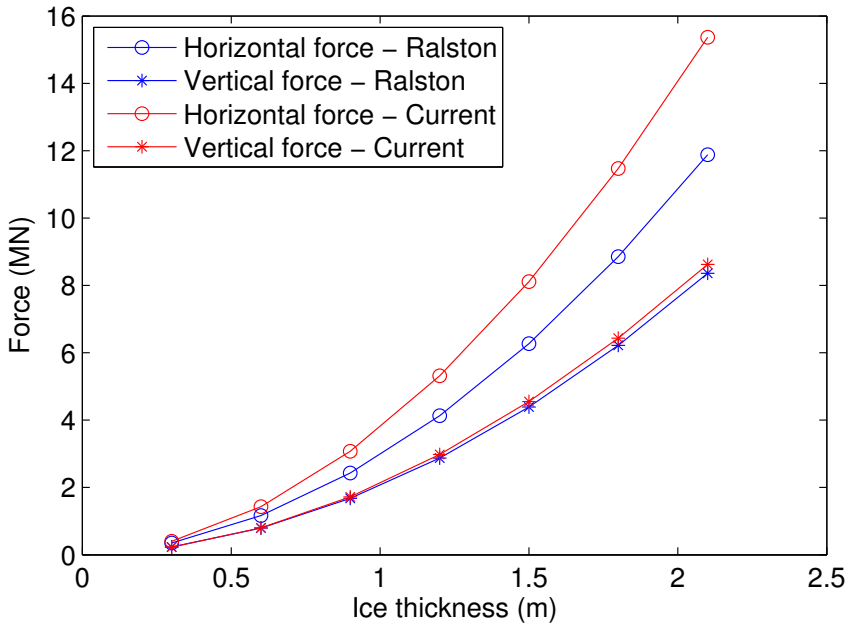

Figure 4.16: Comparison of ice breaking forces resulting from the current model and Ralston's method, with respect to different ice thickness

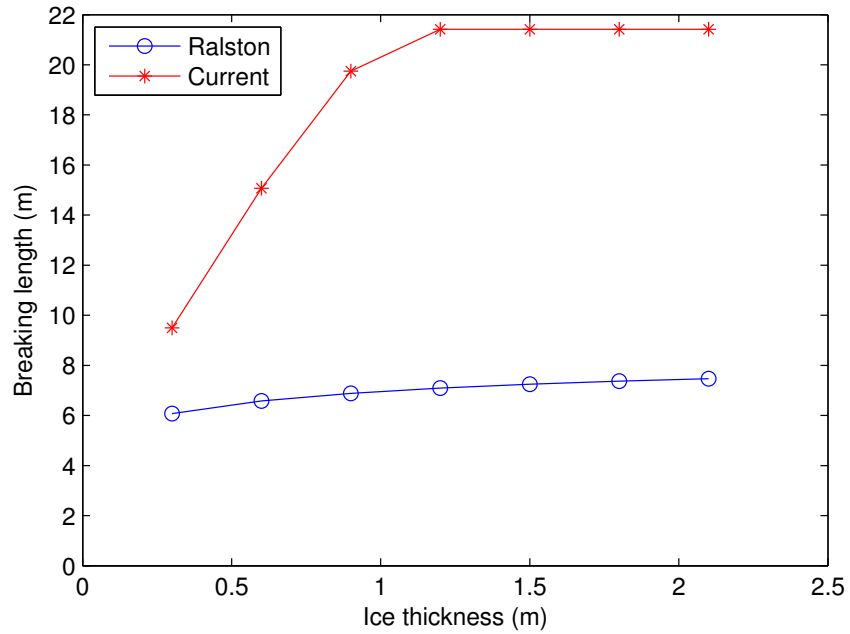

Figure 4.17: Comparison of breaking lengths resulting from the current model and Ralston's method, with respect to different ice thickness

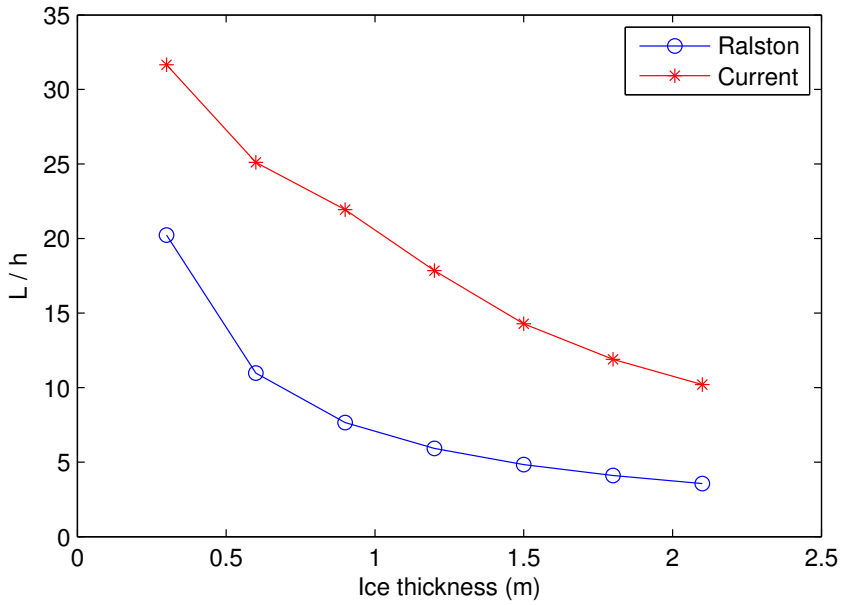

Figure 4.18: Comparison of breaking lengths resulting from the current model and Ralston's method, with respect to different ice thickness

4.6 Conclusion and discussion

In this Chapter, a method is proposed to approximate the ice deformation field when an ice sheet interacts with a sloping structure. In this method, the ice is idealized as a rigid-plastic material. A relation is established between the force exerted on the ice by the structure and the displacement field of the ice. The result shows a plastic hinge traveling towards the contact edge between ice and structure. Criteria that include a limit strain rate and a limit strain are established to determine when ice fails in fracture at the plastic hinge. By setting the criteria, the force and location of the hinge when ice breaks can be calculated. The resulting ice breaking force and breaking length are compared to results of other theories.

This chapter also provides a quasi-static ice force time history that describe the change of ice force over time after the bending failure happens. The weight of the ice pieces riding up the cone is taken into consideration. The ice force reaches a peak

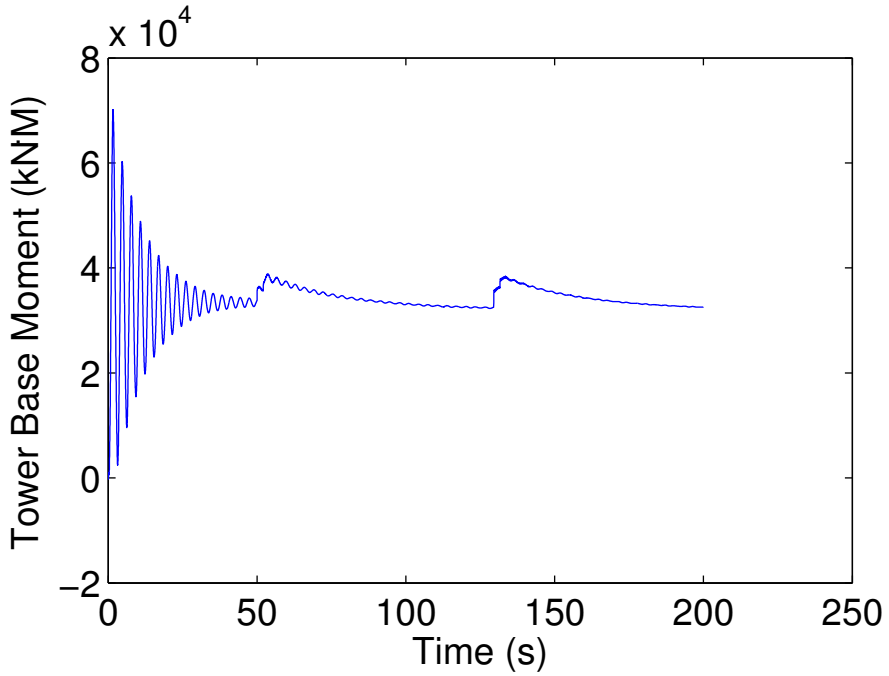

Figure 4.19: Time history of FAST simulated wind turbine tower base moment under ice loading with flexural failure mode

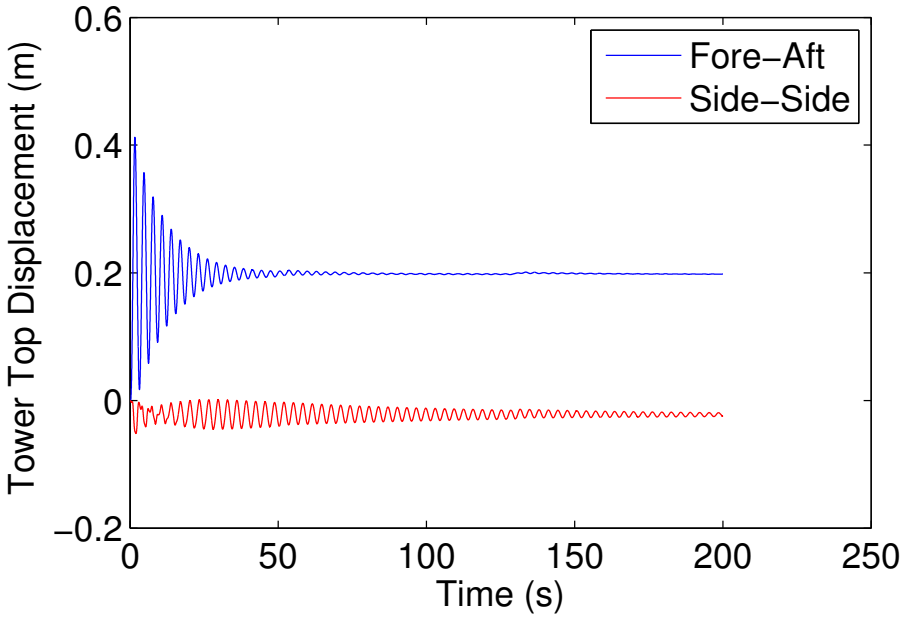

Figure 4.20: Time history of FAST simulated wind turbine tower top displacement under ice loading with flexural failure mode

value when the ice breaks and then suddenly drops to a lower level. As the broken ice piece is pushed and rides up the structure, the force first increases and then gradually decreases to zero until the intact piece contacts the structure and break. The resulting ice force is cyclic.

One future improvement of the current model can be the coupling the motion of the ice and the structure. According to Mroz et al. (*Mróz et al.*, 2008), semi-active conical structures with compliant connection to the towers are applied to reduce towers' response to ice loading. For this kind of structures, the structure motion may have influences on the ice loading. Therefore, a dynamic model of ice bending failure is needed. Another development may be combining the current model with models of other ice failure modes. According to previous model test observations, a transition in failure mode is often observed to occur at a certain velocity, thickness or cone angle from predominantly bending to predominantly crushing (*Dempsey et al.*, 1999; *Finn et al.*, 1993). Therefore, a model of mixed ice failure modes may be needed for some cases of ice interaction with sloping structure.

CHAPTER V

Ice Growth Prediction Model

5.1 Introduction

In all the ice models in previous chapters, ice thickness is an essential input parameter in the prediction of ice loading on offshore structures. In the Great Lakes, ice usually forms during November and fully melts around April. The ice thickness change over time is a function of many environmental factors. In order to simulate the change of ice loading on offshore wind turbines during winters, it is necessary to establish ice thickness as a function of time and environmental factors.

Many previous research addressed this problem. Assel (*Assel*, 1976) developed a statistical technique for ice thickness prediction on the Great Lakes. The technique is based on regression analysis of ice thicknesses and freezing degree-day (FDD) accumulations for individual ice measurement sites. Semtner et al. (*Semtner Jr*, 1976) develops a one-dimensional time-dependent vertical diffusion model within the thickness of ice, which took internal heating into consideration. The resulting non-linear differential equation is solved by numerical schemes for an ice temperature distribution across the ice thickness. Gu and Stefan (*Gu and Stefan*, 1990) studied the way to simulate year-round change of water temperature and ice and snow thickness of cold climate lakes. They established a five-layer heat transfer equilibrium that model the heat transfer between air, snow, ice, water and sediment.

Another important problem to consider when simulating ice growth is the start of ice formation. It is a very dynamic process and is not only governed by the thermodynamic interaction between air and water. The initial thin ice cover formed due to cold may be broken up by rising winds, under daytime heating. It also depends on the size and depth of the lake. On very large lakes a considerable thickness of ice is required to resist the wind shear without breaking (*Fang et al.*, 1996).

Many previous researches gave empirical criteria of ice formation. Harleman et al. (*Harleman*, 1986) argued that the establishment of an intact ice cover required an average daily air temperature below $-5°C$, a daily average wind speed less than 5 m/s and a volume averaged water temperature less than $2°C$. Meanwhile, Gu and Stefan (*Gu and Stefan*, 1990) found that appropriate conditions to determine the freeze-over date for Lake Calhoun, Minnesota, is $-2°C$ average air temperature, 5 m/s average wind speed and $2°C$ average water temperature. Fang et al. (*Fang et al.*, 1996) established an analytical way to determine ice formation date on a lake.

In many previous ice growth prediction models, values of solar radiation, air temperature, profile of water temperature, sediment temperature and wind speed are needed as inputs. At places where limited environmental data is available, a simplified method is needed. In this chapter, a method of predicting ice growth based mainly on air temperature is proposed. This method is based on Stefan's law and considered the heat transfer from water to ice. Based on this model, three modifications are proposed in order to better predict ice thickness at early and late winter. The resulting ice growth simulation is compared to maximum ice thickness data measured at Lake Huron provided by U.S. National Ice Center (*U.S. National Ice Center (USNIC)*, 2014).

5.2 Ice thickness prediction model and field measurement data comparison

In this research, the thermodynamic model of ice is based on the one-dimensional heat conduction equation along the thickness of ice (*Lepparanta*, 1993)

$$\frac{\partial}{\partial t}\left(\rho_i c_i T\right) = \frac{\partial}{\partial z}\left(\kappa_i \frac{\partial T}{\partial z}\right) + q \tag{5.1}$$

where ρ_i is the mass density of ice, c_i is the specific heat of ice, T is the ice temperature, κ_i is the heat conductivity of ice, and q is the internal heat resource term.

The boundary conditions are: first, the heat exchange equilibrium on the top surface

$$\kappa_i \frac{\partial T}{\partial z} = Q_T \tag{5.2}$$

where Q_T is the heat flux on the top ice surface.

Second, the ice temperature at the bottom surface equals the freezing point of ice

$$T_b = T_f \tag{5.3}$$

Also, the bottom surface level is changing

$$\rho_i L \frac{dH}{dt} = \kappa_i \frac{\partial T}{\partial z}\bigg|_{bottom} - Q_w \tag{5.4}$$

where L is the latent heat of freezing and Q_w is the heat flux from water to ice and H is the ice thickness.

In order to solve these problems, we make assumptions based on Stefans law: there is no thermal inertia (the diurnal ice temperature variation is small), no internal heat resource, with a known or prescribed temperature at the top. One additional assumption is that there is a constant Q_w at the bottom surface of ice. The resulted

ice temperature is linear through the thickness:

$$T(z,t) = T_0(t) + \frac{T_f - T_0(t)}{H} z \tag{5.5}$$

The lower boundary level function becomes

$$\rho_i L \frac{dH}{dt} = \kappa_i \frac{T_f - T_0}{H} - Q_w \tag{5.6}$$

Let

$$A = \frac{\kappa_i}{\rho_i L} \left(T_f - T_0\right), B = -\frac{Q_w}{\rho_i L} \tag{5.7}$$

The lower boundary level function then becomes

$$\frac{dH}{dt} = \frac{A}{H} + B \tag{5.8}$$

The above is a non-linear differential equation. It can be integrated over a small period of time base on the assumption that during that time, the temperature T_0 does not change. Let H_0 and H be the ice thickness at the beginning and end of the time period then

$$\frac{h}{A + Bh} dh = dt$$

$$\Delta t = \int_{H_0}^{H} \frac{h}{A + Bh} dh$$

$$\Delta t = \frac{1}{B}(H - H_0) - \frac{A}{B^2} ln \left(\frac{A + BH}{A + BH_0} \right) \tag{5.9}$$

Ice thickness H at the end of one day can be solved from Eqn. 5.9 using Newton-Raphson method, if H_0 is known. Meanwhile, the ice thickness change over time according to Stefan's law (Q_w=0) has a close-form solution for any time interval

$[t_0, t]$:

$$H = \sqrt{H_0^2 + 2\int_{t_0}^{t} \frac{\kappa_i \left(T_f - T_0(\tau)\right)}{\rho_i L_i} d\tau} \tag{5.10}$$

In order to test this model, we use environmental data of air temperature and maximum ice thickness measured at Lake Huron provided by USNIC (*U.S. National Ice Center (USNIC)*, 2014) and collected by University of Michigan student Nicholas Garant (*Garant*, 2011). The average air temperature during year 2002-2003 is used as input T_0, as in Fig 5.1, using time interval of one day. We then calculate ice thickness over time using the above model and compare it to the maximum ice thickness data measured at Huron Lake. The constants values used in this calculation are as suggested by Hinkel (*Hinkel*, 1983): $L = 3.35 \times 10^5 J \cdot kg^{-1}$, $\rho_i = 920 kg \cdot m^{-3}$, $c_i = 1.93 \times 10^6 J \cdot m^{-3}$, $\kappa_i = 2.18 W \cdot m^{-1 \circ} C^{-1}$, $Q_w = 5 W \cdot m^{-2}$, $T_f = 0^\circ C$, $\Delta t = 1 Day = 86,400 s$.

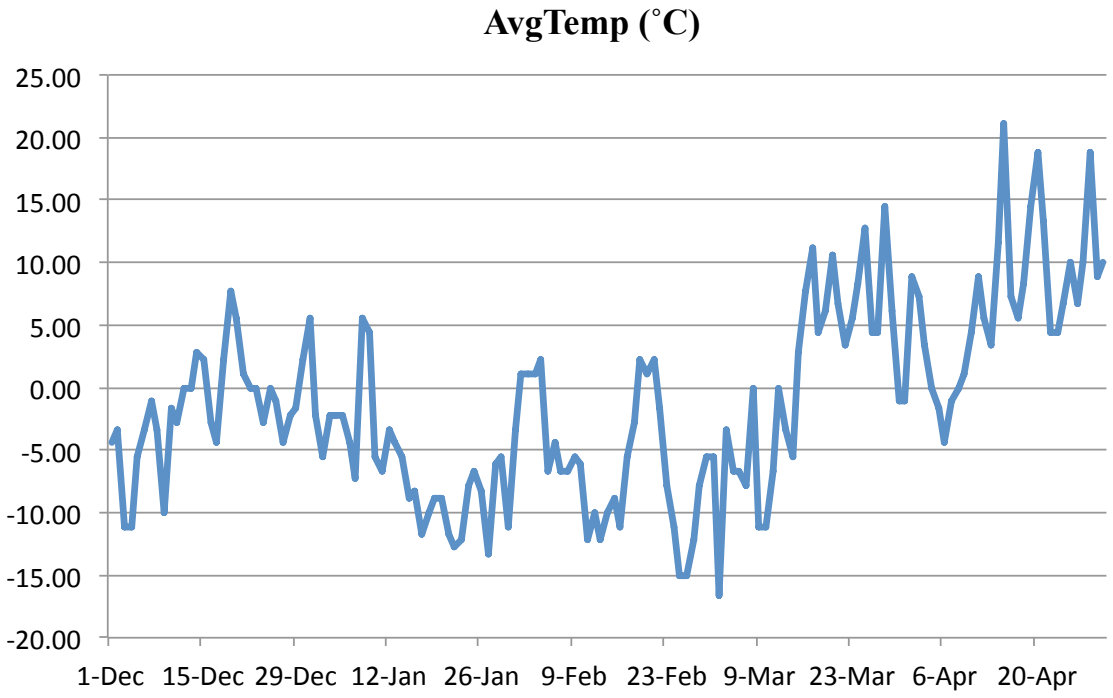

Figure 5.1: Daily averaged air temperature measured at Lake Huron 2002-2003 (*Garant*, 2011)

Another set of prediction results are calculated assuming $Q_w = 0$, as suggested by Stefan's Law. The comparison of these two sets of predictions with the maximum ice thickness measured at Port Huron Light House is shown in Fig 5.2.

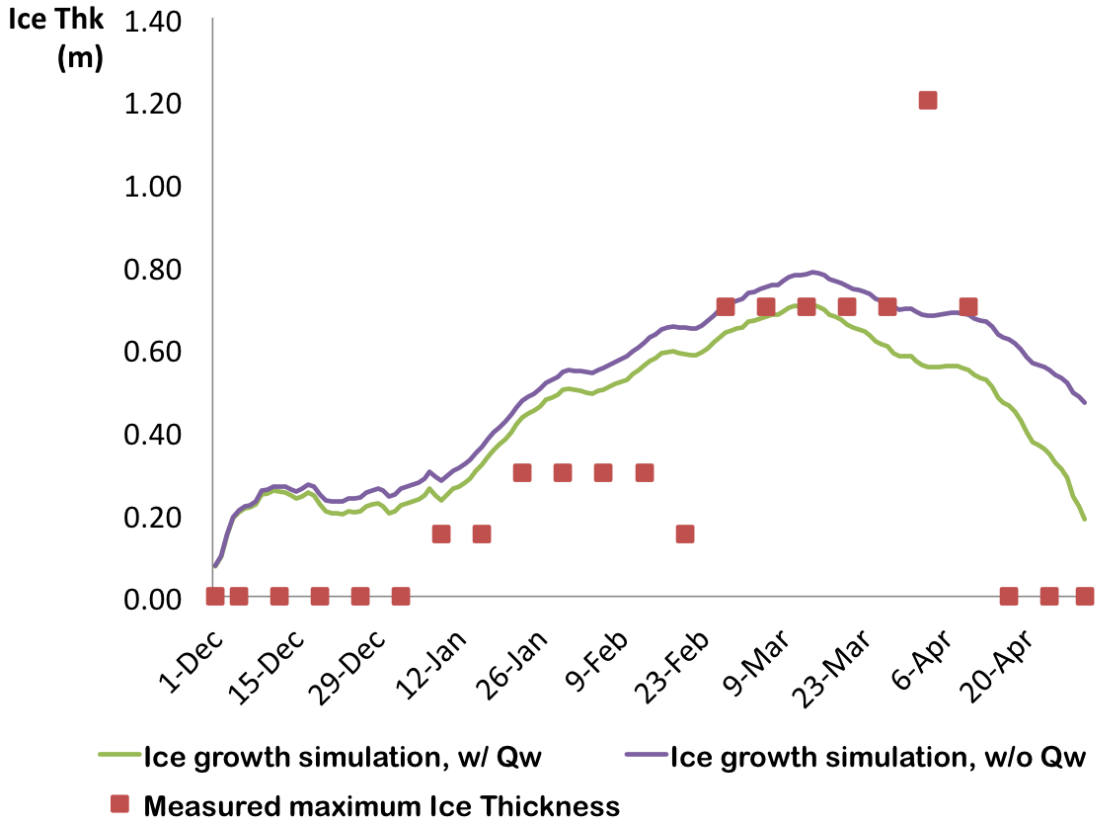

Figure 5.2: Comparison of ice growth prediction results with measured ice thickness data (*Garant*, 2011)

From Fig 5.2, it can be seen that the model assuming $Q_w = 0$ predicts larger ice thickness than that assuming $Q_w > 0$. This is expected since the heat flux from water to ice will help melting the ice, thus decreasing the ice thickness. It can also be observed that the difference between the two models increases over time. This is due to the accumulation of the heat transferred from water over time. In March, both sets of the predicted thickness agree well with the measured data. But the predictions fail to capture the extreme thick ice condition in the late March. Since the measured data is the maximum ice thickness measured at the Port Huron, there are many other

factors that influence its value, such as current and wind induced drifting. Therefore, it is reasonable that the analytical model does not predict extreme ice situations.

At the beginning and end of winter, both models over-predict ice thickness. One reason is that the model assumes the ice top surface temperature equals to the average air temperature. There are some days when the air temperatures are above the freezing point of ice. When this happens, with the linear ice temperature field, the whole ice sheet would have temperature above ice freezing point, which is unrealistic. In this case, the heat exchange on top of the ice surface is considered in equilibrium and no surface melting is considered. This explains why prediction result does not have as sharp decreases in warm days such as Feb 23 and late April. Also, at the beginning of winter, the analytical model assumes ice already exist, with thickness close to zero and top surface temperature equals to air temperature. In reality, it takes sometime to overcome the heat of fusion of the surface water body before it freezes. The above reasons may explain why at the beginning of December, the predicted thickness increases much faster than measured. In the following section, three modifications are tested in order to better simulate ice growth in early winter.

5.3 Modifications of ice growth model

5.3.1 Ice formation simulation

As discussed in the previous section, at the beginning of a winter before ice forms, the air and water directly interact. The heat transferred from water to air should overcome the heat of fusion of the surface water body in order for ice to form. Therefore, we need to first establish the heat equation of the water body and then simulate ice formation by considering the heat of fusion. The one-dimensional heat equation

along vertical depth of water can be written as

$$\frac{\partial u}{\partial t} = \alpha \frac{\partial^2 u}{\partial z^2} \tag{5.11}$$

where u is the water temperature and α is thermal diffusivity of water.

The boundary conditions are: at the bottom of the water, water temperature equals to sediment temperature.

$$u(z = D, t) = T_s \tag{5.12}$$

At the top surface of the water, water temperature equals the water freezing point:

$$u(z = 0, t) = 0 \tag{5.13}$$

According to the common form of solution to the heat equation Eqn. 5.11, we can assume the steady state condition is linear distribution of the water temperature along depth.

$$u(z, t = \infty) = \frac{T_s}{D} z \tag{5.14}$$

And the initial condition:

$$f(z) = \frac{T_s}{D} z + sin \frac{\pi z}{D} \tag{5.15}$$

The resulted temperature field of water body from the above equations is:

$$u(z, t) = \frac{T_s}{D} z + sin \frac{\pi z}{D} e^{-\pi \alpha^2 t} \tag{5.16}$$

At the water/air interface, the difference between upward heat flux to the air and heat flux from the water is the heat of fusion of ice formation (*Semtner Jr*, 1976):

$$\rho_i L_i \frac{dH}{dt} = Q_A - Q_W \tag{5.17}$$

where ρ_i is the mass density of ice, L_i is the latent heat of freezing of ice, H is the ice thickness, Q_A is the heat flux to the air, Q_W is the heat flux from the water. The heat flux has a positive value if it's upward. The heat flux from water can be derived from the temperature field of the water body:

$$Q_W = \kappa_w \left.\frac{du}{dz}\right|_{z=0} \tag{5.18}$$

$$= \kappa_w \left(\frac{T_s}{D} + \frac{\pi}{D} e^{-(\pi\alpha)^2 t}\right) \tag{5.19}$$

where κ_w is the heat conductivity of water.

The heat flux to the air can be written as (*Lepparanta*, 1993):

$$Q_A = \kappa_a(T_0 - T_a) = \kappa_a(0 - T_a) \tag{5.20}$$

where κ_a is the heat exchange coefficient of air and T_a is the air temperature. According to Lapparanta (*Lepparanta*, 1993):

$$\kappa_a/\kappa_i = 10(cm) \tag{5.21}$$

where κ_i is the heat conductivity of ice. Then equation 5.17 becomes:

$$\rho_i L_i \frac{dH}{dt} = \kappa_a(0 - T_a) - \kappa_w \left(\frac{T_s}{D} + \frac{\pi}{D} e^{-(\pi\alpha)^2 t}\right) \tag{5.22}$$

$$dH = \frac{\kappa_a}{\rho_i L_i}(-T_a)dt - \frac{\kappa_w}{\rho_i L_i}\left(\frac{T_s}{D} + \frac{\pi}{D} e^{-(\pi\alpha)^2 t}\right) dt \tag{5.23}$$

From the above equation, we will be able to calculate the thickness of ice formed at the end of one day $H = H_0 + dH = 0 + dH$, $dt = 86,400s$ based the air temperature of that day. And once the ice forms, we will go back to Eqn. 5.9 to predict the ice thickness for the rest of the winter. In this case, when ice thickness is over 0.1 m,

which is after two days, we go back to Eqn. 5.9. The constants used in this calculation are: (*Hinkel*, 1983): $L = 3.35 \times 10^5 J \cdot kg^{-1}$, $\rho_i = 920 kg \cdot m^{-3}$, $c_i = 1.93 \times 10^6 J \cdot m^{-3}$, $\kappa_i = 2.18 W \cdot m^{-1 \circ} C^{-1}$, $\kappa_w = 0.90 W \cdot m^{-1 \circ} C^{-1}$, $T_f = 0^\circ C$, $T_s = 10^\circ C$, $D = 10m$, $\alpha = 0.143 \times 10^{-6} m^2/s$.

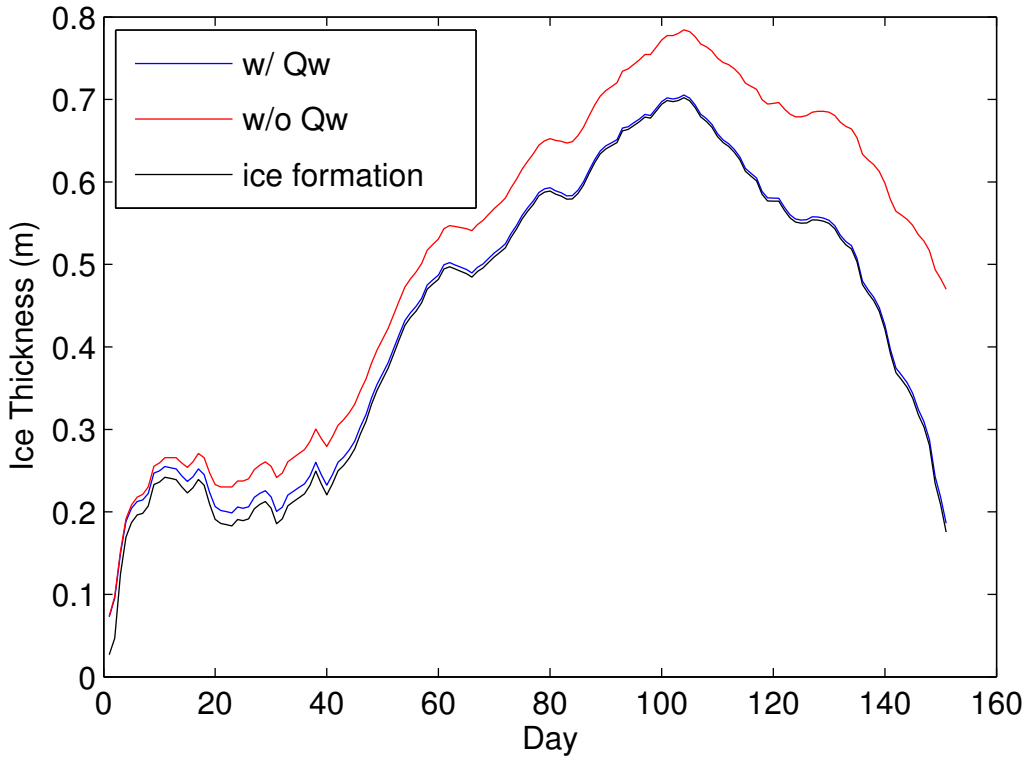

Figure 5.3: Comparison of ice growth simulation results of models: Stefan's law (w/o Q_w), Stefan's law with Q_w and Stefan's law with Q_w and with two days of ice formation

By comparing the results of these three different ice thickness prediction models shown in Fig 5.3, we can see that in the first month, the ice thickness predicted by the third model is a few centimeters less than the model with Q_w. And for the rest of the winter, these two models give very close results. The third model still largely over-predicts ice thickness during early winter. Therefore, more methods should be considered.

5.3.2 Ice-air heat exchange

One inaccuracy of the current proposed model is the assumption that ice top surface temperature equals to the recorded air temperature. Since air temperature is usually measured at some altitude, it does not necessarily equal the ice surface temperature. In order to calculate ice surface temperature T_0, a continuity condition for the heat flux at the ice-air interface should be established (*Lepparanta*, 1993). Assuming there is no snow, the heat exchange between ice and air can be approximated as:

$$Q_a = \kappa_a \left(T_0 - T_a\right) \tag{5.24}$$

where κ_a is the ice/air heat exchange coefficient and T_a is the average air temperature. Then the continuity condition should be:

$$\kappa_i \frac{(T_f - T_0)}{H} = \kappa_a \left(T_0 - T_a\right) \tag{5.25}$$

where κ_i is the heat conductivity of ice, T_f is the freezing point of ice.

From the above equation, the ice top surface temperature can be solved:

$$T_0 = \frac{\kappa_i T_f + H\kappa_a T_a}{\kappa_i + H\kappa_a} \tag{5.26}$$

Then the equation that governs the ice thickness change over time Eqn. 5.6 becomes:

$$\rho_i L \frac{dH}{dt} = \kappa_i \frac{T_f - T_a}{H + \kappa_i/\kappa_a} - Q_w \tag{5.27}$$

where ρ_i is the mass density of ice, L is the latent heat of freezing and Q_w is the heat flux from water.

The solution to the above equation without the Q_w term is given by Lepparanta (*Lepparanta*, 1993). Here we solve the above nonlinear equation by integrating over

a short period of time. Similar to the analysis of the previous sections, Eqn. 5.27 can be written in the form:

$$\frac{dH}{dt} = \frac{A}{H+C} + B \tag{5.28}$$

where

$$A = \frac{\kappa_i \left(T_f - T_a\right)}{\rho_i L} \tag{5.29}$$

$$B = -\frac{Q_w}{\rho_i L} \tag{5.30}$$

$$C = \frac{\kappa_i}{\kappa_a} \tag{5.31}$$

Therefore,

$$dt = \frac{H+C}{A+BC+BH} dH \tag{5.32}$$

Let H_0 and H be the ice thickness at the beginning and end of the time period then

$$\Delta t = \int_{H_0}^{H} \frac{h+C}{Bh+A+Bc} dh \tag{5.33}$$

$$\Delta t = \frac{1}{B}(H - H_0) - \frac{A}{B^2} \ln\left(\frac{A+BH+BC}{A+BH_0+BC}\right) \tag{5.34}$$

Ice thickness H at the end of one day can be solved from Eqn. 5.34 using Newton-Raphson method based on a known value of H_0, which is the ice thickness at the end of the pervious day. Here we also use the constants suggested by Hinkel (*Hinkel*, 1983): $L = 3.35 \times 10^5 J \cdot kg^{-1}$, $\rho_i = 920 kg \cdot m^{-3}$, $c_i = 1.93 \times 10^6 J \cdot m^{-3}$, $\kappa_i = 2.18 W \cdot m^{-1 \circ} C^{-1}$, $Q_w = 5 W \cdot m^{-2}$, $T_f = 0^\circ C$, $\Delta t = 1 Day = 86,400 s$ and $\kappa_i / \kappa_a = 20 cm$. The result is shown in Fig. 5.4

It can be seen in Fig. 5.4 that the model with ice-air heat exchange provides much better prediction of ice thickness in early season, especially during January to middle February. It can also be observed that this model predict a slower ice growth rate than the model with only Q_w, at the first 7-10 days of the season. After that, these

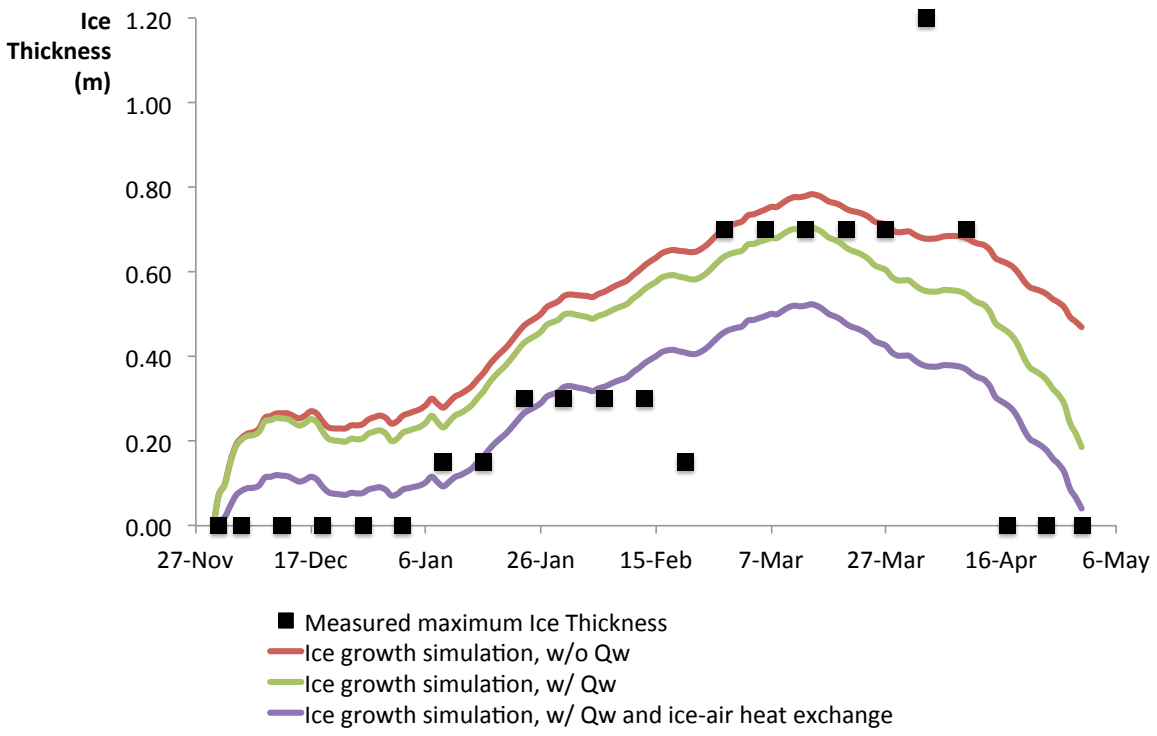

Figure 5.4: Comparison of ice growth simulation results of models: Stefan's law (w/o Q_w), Stefan's law with Q_w and Stefan's law with Q_w and with ice-air heat exchange to measured data (*Garant*, 2011)

two models have almost parallel ice growth curves. This is as expected, since if we assume the ice freezing point $T_f = 0$, then Eqn. 5.26 can be written in the form:

$$T_0 = \frac{T_a}{1 + \frac{1}{H}\frac{\kappa_i}{\kappa_a}} \tag{5.35}$$

When H is small, $1/H$ is large and T_0 has a much smaller absolute value than T_a, which means T_0 is approximately $0°C$. When $T_a < 0$, $T_f - T_a > T_f - T_0$. Then according to Eqn. 5.27, the ice growth rate of the current model is much smaller than the model with only Q_w when H is small.

5.3.3 Surface melting

Another possible modification is considering melting on the ice top surface. In all the previous models, when the air temperature is above the melting point of ice, the ice temperature becomes higher than the melting point as well, which is unrealistic. A simple method is proposed to modify this situation.

When the air temperature is above the melting point T_f, we assume that the temperature at the top surface of ice equals to the melting point: $T_0 = T_f$. Under this assumption, the ice temperature distribution along its thickness becomes uniform:

$$T(z) = T_f \tag{5.36}$$

$$\frac{\partial T}{\partial z} = 0 \tag{5.37}$$

The heat transfer equilibrium at the ice top surface is thus broken. There is ice melting at the top surface. Therefore, the total ice thickness change over time can be modeled as:

$$\rho_i L \frac{dH}{dt} = Q_a - Q_w \tag{5.38}$$

where Q_a is calculated by Eqn. 5.24 and Q_w is a constant value.

The the ice thickness change over time can be calculated as:

$$H = H_0 - \left[\frac{\kappa_a (T_a - T_f)}{\rho_i L} + \frac{Q_w}{\rho_i L} \right] \Delta t \tag{5.39}$$

Combing the surface melting analysis with previous models, we simulate the ice thickness time history using two models: one is the Stefan's law with Q_w and ice surface melting; the other is the Stefan's law with Q_w, ice-air coupling and surface melting. The results are compared with those from previous models as shown in Fig. 5.5. The constants' values are as follows: $L = 3.35 \times 10^5 J \cdot kg^{-1}$, $\rho_i = 920 kg \cdot m^{-3}$, $c_i = 1.93 \times 10^6 J \cdot m^{-3}$, $\kappa_i = 2.18 W \cdot m^{-1 \circ} C^{-1}$, $Q_w = 5 W \cdot m^{-2}$, $T_f = 0^\circ C$, $\Delta t =$

$1Day = 86,400s$ and $\kappa_i/\kappa_a = 20cm$.

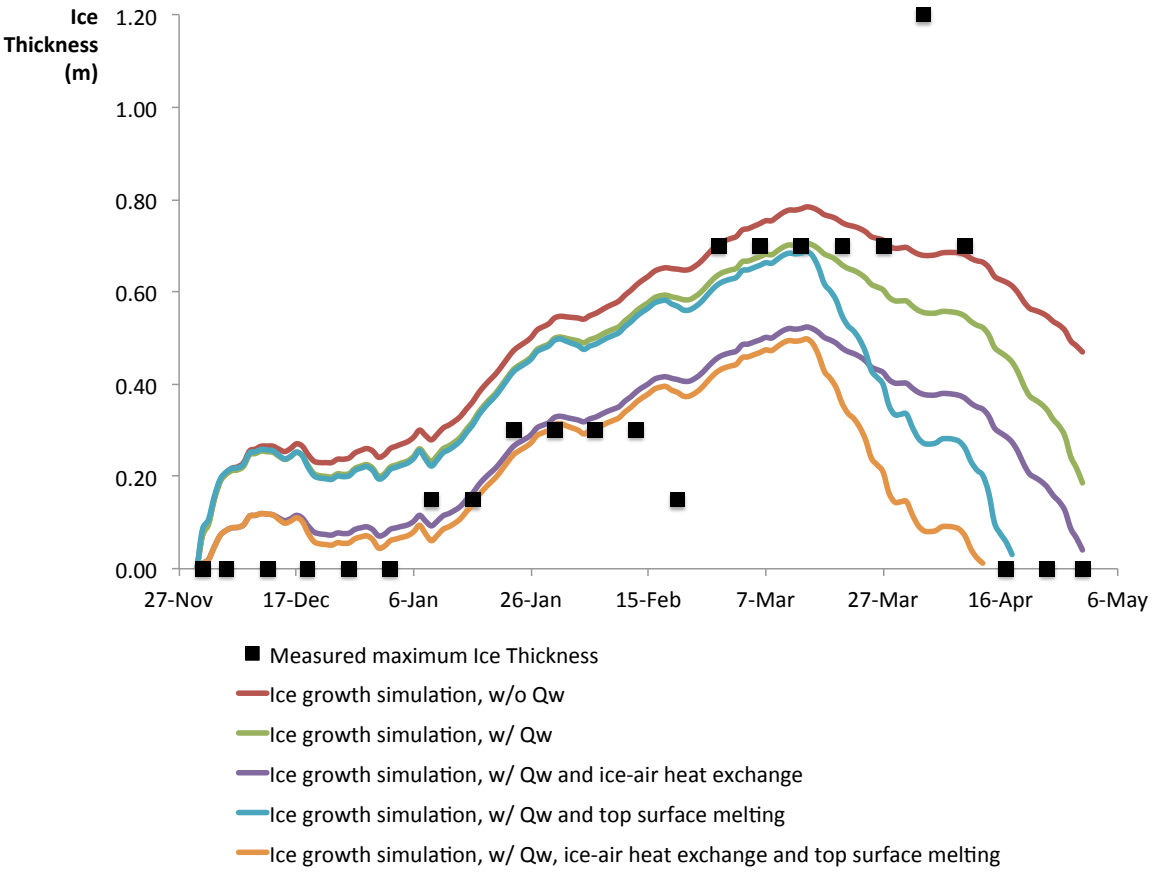

Figure 5.5: Comparison of ice growth simulation results of models: Stefan's law (w/o Q_w), Stefan's law with Q_w, Stefan's law with Q_w and with ice-air heat exchange, Stefan's law with Q_w and surface melting and Stefan's law with Q_w, ice-air heat exchange and surface melting to measured data (*Garant*, 2011)

In Fig. 5.5, it can be observed that these two new models give similar ice growth predictions at early to mid winter to models that don't consider surface melting. At late winter, when the air temperature become mainly above $0°C$, the simulated values of ice thickness decrease much faster using new models. The two new models predict that ice totally melt at mid April, which agrees well the field observed data.

5.4 Discussion and Conclusion

In this chapter, a method of predicting ice thickness change over time based on limited environmental data is provided. Based on this method, three modifications are proposed in order to better predict ice growth and decay in the early and late winter. Simulations of total six models are presented and compared to maximum ice thickness data measured at Lake Huron during the year of 2002-2003.

The first model is the classic Stefan's law. The second model adds a terms Q_w that represents a constant heat transfer from water. These two models are compared to field measured data in Fig. 5.2. The new model predicts smaller ice thickness than the Stefan's law. But both models over-predict ice thickness in early season. Three modification models are proposed. The third model considers water-air interaction prior to ice formation. The result of this model is compared to the previous two models in Fig. 5.3. This model does not provide a much different prediction than the second model. The fourth model gives a better approximation of ice top surface temperature by considering ice-air heat exchange. This model is compared to the first two models in Fig. 5.4. This model provides a better approximation for ice thickness in early winter, but underestimate the ice thickness in mid winter by a large extent. The fifth and sixth model combine the consideration of ice top surface melting to the second and third model respectively. The results are shown in Fig. 5.5. Both models predict a date when all ice melts closely to field observed date.

It should be noted that, even model 4 and 6 over estimate ice thickness at early winter. In reality, there are factors other than thermodynamic ones that affect ice formation. According to Fang et. al. (*Fang et al.*, 1996), convective mixing due to density instability on the top surface of water and wind mixing critically affect the process of ice cover formation. Considering the empirical criteria suggested by previous researches, air temperature before Dec 29^{th} is above the critical value of $-5°C$. Accordingly, the observed ice thickness before Dec 29^{th} is around zero. There-

fore, the current models combined with some empirical criterial might return a better prediction. To better predict ice growth at early winter, we may need to consider wind and convective mixing near upper surface of water body. However, such study may need more detailed environmental data, such as daily wind speed and sediment temperature.

As a summary, the first two models provide better predictions of ice thickness in mid winter but overestimate ice thickness in early and late season. Meanwhile, the fourth and sixth model provide better predictions at early winter but underestimate ice thickness values during the middle winter. The fifth model is able to capture the value of ice thickness in mid winter and ice melting date. Each model provides better estimation at different time period. They can be utilized according to different analytical needs. For example, the second model is are able to predict maximum ice thickness during the winter 2002-2003, except for an extreme value happens at early April. The existence of this extreme thick ice might due to factors other than thermodynamic factors, such as the collision of ice floes driven by wind and currents, which may form ice ridges with significantly large thickness. Therefore, in spite of this shortcoming, this model can be used to predict ice formation and assist in estimating design ice loads for offshore wind turbines.

CHAPTER VI

Conclusion

Computer-Aided Engineering tools are needed that are capable of modeling the design-driving loads that will interact with an offshore wind turbine system during operation, to allow for innovation of long-term solutions for offshore wind turbines in a variety of environmental conditions. This thesis describes efforts to augment existing CAE tools used for offshore wind turbine analysis with a new module that can provide simulation capability for ice loading on the system. This is accomplished by creating an ice-loading module coupled to FAST, the CAE tool maintained by the National Renewable Energy Laboratory, for simulating onshore and offshore wind turbine dynamics.

The new module includes both static and dynamic ice loading that can be applied during a dynamic simulation of an offshore wind turbine. The ice force can be prescribed, or influenced by the structure's compliant response only or by the dynamics of both the structure and the ice floe. The new module covers ice failure modes of creep, buckling, crushing, splitting and bending. The supporting structure of wind turbines can be modeled as vertical or sloping form at the waterline.

Besides application of existing ice mechanics theories to simulate ice loading in different scenarios, two new analytical ice models are proposed in this thesis. One simulates time-dependent ice impact with ice failing non-simultaneously across the

ice-structure contact area. This model results in an ice force time history based on the shape of the ice-structure contact surface, the strength of each independent failure zone, ice drifting velocity and the structure displacement. Another new analytical model is the method to approximate the ice deformation field when an ice sheet interacts with a sloping structure. A relation is established between the force exerted on the ice by the structure and the displacement field of the ice. A quasi-static ice force time history that describe the change of ice force over time after the bending failure happens is also provided. The results of both new models are compared to results of existing theories show good agreements.

Further refinements of the ice module can be considered from two directions. One is improving the analytical models. For the non-simultaneous ice failure model, random and spatially non-uniform strength of a single zone may provide more accurate simulation results according to some field observations. Also, further investigations are needed for deciding parameters such as ice teeth spacing. For the ice bending model, one future improvement can be coupling the motion of the ice and the structure, if the ice module is applied to semi-active conical structures with compliant connection to wind turbine towers.

Another direction of consideration of refining the current ice module is combining different models with different ice failure modes. According to observations of many model tests, a transition of ice failure mode is usually seen at a certain ice velocity, thickness or structure property. Therefore, a model is needed that can generate ice force time history of multiple ice failure modes that may happen sequentially or simultaneously.

Besides the ice loading models, several simplified models of predicting ice thickness change over time based on limited environmental data are also presented. These models are able to predict maximum ice thickness during the middle of winter 2002-2003, except for extreme values; ice thickness in the early winter and ice melting

date. These model can be useful to assist in the prediction of design ice load for normal working conditions for offshore wind turbines during different time periods of a winter.

BIBLIOGRAPHY

BIBLIOGRAPHY

Aksnes, V. (2011), A panel method for modelling level ice actions on moored ships. part 1: Local ice force formulation, *Cold Regions Science and Technology*, *65*(2), 128–136.

Ashby, M., et al. (1986), Nonsimultaneous failure and ice loads on arctic structures, in *Offshore Technology Conference*.

Assel, R. (1976), Great lakes ice thickness prediction, *Journal of Great Lakes Research*, *2*(2), 248–255.

Augusti, G. (1970), Mode approximations for rigid-plastic structures supported by an elastic medium, *International Journal of Solids and Structures*, *6*(6), 809–827.

Barker, A., G. Timco, H. Gravesen, and P. Vølund (2005), Ice loading on danish wind turbines: Part 1: Dynamic model tests, *Cold Regions Science and Technology*, *41*(1), 1–23.

Bhat, S. (1988), Analysis for splitting of ice floes during summer impact, *Cold Regions Science and Technology*, *15*(1), 53–63.

Bhat, S. (1990), Modeling of size effect in ice mechanics using fractal concepts, *Journal of Offshore Mechanics and Arctic Engineering*, *112*(4), 370–376.

Bhat, S., S. Choi, T. Wierzbicki, and D. Karr (1991), Failure analysis of impacting ice floes, *Journal of Offshore Mechanics and Arctic Engineering*, *113*, 171.

BOEM (2013), Offshore Wind Energy.

BSI (2011), *Petroleum and natural gas industries arctic offshore structures (BS EN ISO 19906:2010)*, British Standards Institution (BSI).

Christensen, F. T., and J. Skourup (1991), Extreme ice properties, *Journal of Cold Regions Engineering,*, *5*, 51–68.

Croasdale, K., and A. Cammaert (1994), An improved method for the calculation of ice loads on sloping structures in first-year ice, *Hydrotechnical Construction*, *28*(3), 174–179.

Daley, C. (2007), Reanalysis of ice pressure-area relationships, *Marine Technology*, *44*(4), 234–244.

Daley, C., J. Tuhkuri, and K. Riska (1998), The role of discrete failures in local ice loads, *Cold regions science and technology*, *27*(3), 197–211.

Damiani, R., and H. Song (2013), Assessing the Importance of Nonlinear Structural Characteristics in the Development of a Jacket Model for the Wind Turbine CAE Tool FAST, *32nd International Conference on Ocean, Offshore and Arctic Engineering (OMAE2013)*.

Dempsey, J., A. Palmer, and D. Sodhi (2001), High pressure zone formation during compressive ice failure, *Engineering fracture mechanics*, *68*(17), 1961–1974.

Dempsey, J. P., C. Fox, and A. C. Palmer (1999), Ice-slope interaction: Transitions in failure mode, in *ASME Offshore Mechanics and Arctic Engineering Conference, St Johns, Canada*, Citeseer.

Fang, X., C. R. Ellis, and H. G. Stefan (1996), Simulation and observation of ice formation (freeze-over) in a lake, *Cold Regions Science and Technology*, *24*(2), 129–145.

Feng, L., Y. Qianjin, K. N. Shkhinek, and T. Karna (2003), A qualitative analysis of breaking length of sheet ice against conical structures, in *Proceedings of the POAC Symposium on Ice. Trondheim Norway: POAC International Committee*.

Finn, D. W., S. J. Jones, and I. J. Jordaan (1993), Vertical and inclined edge-indentation of freshwater ice sheets, *Cold regions science and technology*, *22*(1), 1–18.

Frederking, R. (1980), Dynamic ice forces on an inclined structure, in *Physics and Mechanics of Ice*, pp. 104–116, Springer.

Garant, N. (2011), NA590 independent study report.

George, D. (1986), River and lake ice engineering.

Gu, R., and H. G. Stefan (1990), Year-round temperature simulation of cold climate lakes, *Cold Regions Science and Technology*, *18*(2), 147–160.

Harleman, D. (1986), Hydrothermal modeling of reservoirs in cold regions: status and research needs, in *Proceedings of the Symposium: Cold Regions Hydrology. University of Alaska-Fairbanks, Fairbanks, Alaska. American Water Resources Association, Bethesda Maryland. 1986. p 39-50, 3 fig, 47 ref.*

Hetényi, M., and M. I. Hetbenyi (1946), *Beams on elastic foundation: theory with applications in the fields of civil and mechanical engineering*, vol. 16, University of Michigan Press.

Hinkel, K. M. (1983), Ice-cover growth rates at nearshore locations in the Great Lakes, *NOAA Technical Memorandum ERL GLERL-44*.

Johnston, M., K. R. Croasdale, and I. J. Jordaan (1998), Localized pressures during ice-structure interaction: relevance to design criteria, *Cold regions science and technology*, *27*(2), 105–117.

Jonkman, J. (), *FAST Theory Manual*, NREL/TP-500-32449, Golden, CO: National Renewable Energy Laboratory, latest ed.

Jonkman, J. (2007), Dynamics Modeling and Loads Analysis of an Offshore Floating Wind Turbine, PhD Thesis, Department of Aerospace Engineering Sciences, University of Colorado, Boulder, CO, nREL/TP-500-41958. Golden, CO: National Renewable Energy Laboratory.

Jonkman, J. (2009), Dynamics of Offshore Floating Wind TurbinesModel Development and Verification, *Wind Energy*, *12*, 459–492.

Jonkman, J. (2013), The New Modularization Framework for the FAST Wind Turbine CAE Tool, *51st AIAA Aerospace Sciences Meeting Including the New Horizons Forum and Aerospace Exposition*.

Jonkman, J., and M. L. Buhl Jr. (2005), *FAST User's Guide*, NREL/EL-500-38230, Golden, CO: National Renewable Energy Laboratory, latest ed.

Jonkman, J., S. Butterfield, W. Musial, and G. Scott (2009), Definition of a 5-MW Reference Wind Turbine for Offshore System Development, *Prepared under task no. wer5.3301, nrel/tp-500-38060*, National Renewable Energy Laboratory, Golden, CO.

Jordaan, I., M. A. Maes, P. W. Brown, and I. P. Hermans (1993), Probabilistic Analysis of Local Ice Pressures, *Journal of Offshore Mechanics and Arctic Engineering*, *115*, 83–89.

Kaldjian, M. J. (1987), Ice-sheet failure against inclined and conical surfaces, *Computers & Structures*, *26*(1), 145–152.

Kamio, Z., H. Matsushita, and B. Strnadel (2003), Statistical analysis of ice fracture characteristics, *Engineering Fracture Mechanics*, *70*, 2075–2088.

Karr, D. G., A. W. Troesch, and W. C. Wingate (1993), Nonlinear dynamic response of a simple ice-structure interaction model, *Journal of Offshore Mechanics and Arctic Engineering*, *115*, 246–252.

Korzhavin, K. (1971), *Action of ice on engineering structures.*, U.S. Army Cold Regions Research and Engineering Laboratory Translation TL260, New Hampshire.

Kry, P. (1980), Third canadian geotechnical colloquium: Ice forces on wide structures, *Canadian Geotechnical Journal*, *17*(1), 97–113.

Laino, D. J., and A. C. Hansen (2002), User's guide to the wind turbine dynamics aerodynamics computer software AeroDyn, *Prepared for the national renewable energy laboratory under subcontract no. tcx-9-29209-01*, Windward Engineering LLC, Salt Lake City, UT.

Lau, M., J. Molgaard, F. Williams, and S. ASJ (1999), An analysis of ice breaking pattern and ice piece size around sloping structures, in *18th international conference on offshore mechanics and arctic engineering*.

Leira, B., L. Borsheim, O. Espeland, and J. Amdahl (2009), Ice-load estimation for a ship hull based on continuous response monitoring, *Journal of Engineering for Maritime Environment*, *223*, 529–540.

Lepparanta, M. (1993), A review of analytical model of sea-ice growth, *Atmosphere Ocean*, *31*, 123–138.

Liu, X., L. Gang, and Y. Q. Oberlies, Robert (2009), Research on short-term dynamic ice cases for dynamic analysis of ice-resistant jacket platform in the Bohai Gulf, *Marine Structure*, *22*, 457–479.

Lu, W., S. Løset, and R. Lubbad (2012), Simulating ice-sloping structure interactions with the cohesive element method, in *Proceedings of the 31st International Conference on Ocean, Offshore and Arctic Engineering, Rio de Janeiro, Brazil.(submitted)*.

Matlock, H., W. Dawkins, and J. Panak (1971), Analytical model for ice-structure interaction, *ASCE Journal of Engineering Mechanics*, *97*, 1083–1092.

Michel, B., and N. Toussaint (1977), Mechanisms and theory of indentation of ice plates, *Journal of Glaciology*, *19*, 285–300.

Moriarty, P. J., and A. C. Hansen (2005), *AeroDyn Theory Manual*, NREL/EL-500-36881, Golden, CO: National Renewable Energy Laboratory, latest ed.

Mróz, A., J. Holnicki-Szulc, and T. Kärnä (2008), Mitigation of ice loading on offshore wind turbines: Feasibility study of a semi-active solution, *Computers & structures*, *86*(3), 217–226.

Palmer, A., and T. Sanderson (1991), Fractal crushing of ice and brittle solids, *Proceedings of the Royal Society of London. Series A: Mathematical and Physical Sciences*, *433*(1889), 469–477.

Popko, W., J. Heinonen, S. Hetmanczyk, and F. Vorpahl (2012), State-of-the-art comparison of standards in terms of dominant sea ice loads for offshore wind turbine support structures in the baltic sea, in *Proceedings of the Twenty-second (2012) International Offshore and Polar Engineering Conference*, Rhodes, Greece.

Poplin, J., and G. Timco (2003), Ice damage zone around conical structures: implications for evacuation, in *Proceedings of the 17 International Conference onthPort and Ocean Engineering under Arctic Conditions POAC'03*, vol. 2, pp. 797–806.

Ralston, T. (1979), Sea ice loads, *Technical seminar on Alaskan Beaufort Sea gravel island design*.

Ralston, T. (1980), Plastic limit analysis of sheet ice loads on conical structures, in *Physics and Mechanics of Ice*, pp. 289–308, Springer.

Sanderson, T. (1988), *Ice mechanics, risk to offshore structures*, Graham & Trotman, London, UK.

Semtner Jr, A. J. (1976), A model for the thermodynamic growth of sea ice in numerical investigations of climate, *Journal of Physical Oceanography*, *6*(3), 379–389.

Sodhi, D. (1998), Nonsimultaneous crushing during edge indentation of freshwater ice sheets, *Cold Regions Science and Technology*, *27*, 179–195.

Sodhi, D. S., and C. E. Morris (1986), Characteristic frequency of force variations in continuous crushing of sheet ice against rigid cylindrical structures, *Cold Regions Science and Technology*, *12*(1), 1–12.

Song, H., R. Damiani, A. Robertson, and J. Jonkman (2013), A New Structural-Dynamics Module for Offshore Multimember Substructures within the Wind Turbine CAE tool FAST, *23rd International Ocean and Polar Engineering Conference*.

Sorensen, C. (1978), Interaction between floating ice sheets and sloping structures, *1978., 175*.

Suyuthi, A., B. J. Leira, and K. Riska (2012), Short term extreme statistics of local ice loads on ship hulls, *Cold Regions Science and Technology*, *130*, 130–143.

Tarp-Johansen, N. J. (2005), Partial safety factors and characteristic values for combined extreme wind and wave load effects., *ASME Journal of Solar Energy Engineering*, *127*, 242–252.

U.S. National Ice Center (USNIC) (2014), Great Lakes Ice Analysis Products.

Wierzbicki, T., and D. Karr (1987), Structural imperfections and interactive failure of edge loaded ice sheets, *Proc. 9th POAC, Fairbanks, Alaska*.

Yu, B., and D. Karr (2013), A surface ice module for wind turbine dynamic response simulation using fast., *Proc. 32nd OMAE, Nantes, France*.

Yue, Q., G. Fengwei, and T. Karna (2009), Dynamic ice forces of slender vertical structures due to ice crushing, *Cold Regions Science and Technology*, *56*, 77–83.